Valley Valves at Domain Walls in Symmetry-Broken Rhombohedral Graphene

Võ Tiến Phong[1,2,*] Francisco Lobo[3], Elsa Prada[3], Pablo San-Jose[3], Francisco Guinea[4,5,†] and Eugene Mele[6‡]
[1]*Department of Physics, Florida State University, Tallahassee, FL, 32306, U.S.A.*
[2]*National High Magnetic Field Laboratory, Tallahassee, FL, 32310, U.S.A.*
[3]*Instituto de Ciencia de Materiales de Madrid (ICMM), CSIC, 28049 Madrid, Spain*
[4]*IMDEA Nanoscience, C/ Faraday 9, 28049 Madrid, Spain*
[5]*Donostia International Physics Center, Paseo Manuel de Lardizábal 4, 20018 San Sebastián, Spain and*
[6]*Department of Physics and Astronomy, University of Pennsylvania, Philadelphia, PA 19104, U.S.A.*
(Dated: June 23, 2026)

Supplementary Information

CONTENTS

I. KEKULE RECONSTRUCTION

To describe intervalley-hybridized states in real space, we consider a $\sqrt{3} \times \sqrt{3}$ reconstruction of the honeycomb unit cell to form a Kekule lattice. In reciprocal space, this reconstruction maps both the K and K' valleys in the original Brillouin zone to $\overline{\Gamma}$ in the folded Brillouin zone. In this setting, momentum-preserving intervalley perturbations (which would necessarily be momentum-non-preserving in the honeycomb lattice) can mix the overlapping states from different valleys and generate intervalley-mixed Bloch wavefunctions. As such, this Kekule reconstruction is a natural and elegant approach to describe intervalley coupling at domain walls.

* vophong@magnet.fsu.edu
† paco.guinea@imdea.edu
‡ mele@physics.upenn.edu

A. Monolayer Toy Models

1. *Valley-Orbital Basis States and Their Symmetry Representations*

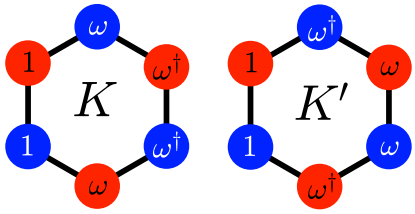

Figure S1. **Phase winding of valley basis states.** $\omega = \exp(2\pi i/3)$.

It is instructive to use simplified single-layer models to define the notion of intervalley interaction. We begin with the tight-binding model of graphene with two sublattices per unit cell. In the usual convention, basis states are written as

$$\begin{aligned} |\psi_A(\mathbf{k})\rangle &= \frac{1}{\sqrt{N}} \sum_{\mathbf{r}} e^{i\mathbf{k}\cdot\mathbf{r}} |\phi_A(\mathbf{r})\rangle \,, \\ |\psi_B(\mathbf{k})\rangle &= \frac{1}{\sqrt{N}} \sum_{\mathbf{r}} e^{i\mathbf{k}\cdot(\mathbf{r}+\boldsymbol{\delta}_{\boldsymbol{r}})} |\phi_B(\mathbf{r})\rangle \,, \end{aligned} \tag{S1}$$

where $\mathbf{r} = n_1\mathbf{a}_1 + n_2\mathbf{a}_2$, where $\mathbf{a}_1 = a(1,0)$, $\mathbf{a}_2 = a(-1/2, \sqrt{3}/2)$, and $\mathbf{a}_3 = a(-1/2, -\sqrt{3}/2)$ are primitive lattice vectors, $a = 2.46$ Å is the lattice constant, n_1 and n_2 are integers, and $\boldsymbol{\delta}_{\boldsymbol{r}} = a/\sqrt{3}(0,1)$ is the basis vector. $|\phi_A(\mathbf{r})\rangle$ is an orbital located at $\mathbf{r}$ while $|\phi_B(\mathbf{r})\rangle$ is an orbital located at $\mathbf{r} + \boldsymbol{\delta}_{\boldsymbol{r}}$. Exactly at the valleys $\mathbf{K} = 4\pi/3a(1,0)$ and $\mathbf{K}' = -4\pi/3a(1,0)$ the wavefunctions take the following form

$$\begin{aligned} |\psi_\sigma(\mathbf{K})\rangle &= \frac{1}{\sqrt{N}} \sum_{n_1,n_2} e^{+\frac{2\pi i}{3}(2n_1-n_2)} |\phi_\sigma(n_1\mathbf{a}_1 + n_2\mathbf{a}_2)\rangle \,, \\ |\psi_\sigma(\mathbf{K}')\rangle &= \frac{1}{\sqrt{N}} \sum_{n_1,n_2} e^{-\frac{2\pi i}{3}(2n_1-n_2)} |\phi_\sigma(n_1\mathbf{a}_1 + n_2\mathbf{a}_2)\rangle \,, \end{aligned} \tag{S2}$$

where $\sigma = \{A, B\}$ labels sublattice. The phases at K in Eq. (S2) are zero if $\mathrm{mod}(2n_1 - n_2, 3) = 0$ and are $\pm 2\pi/3$ if $\mathrm{mod}(2n_1 - n_2, 3) = \pm 1$. The phases at K' are complex conjugates of those at K. Around a hexagon, the phases on the A (B) sublattice wind clockwise (counterclockwise) in the K valley. For the K' valley, the phases on the A (B) sublattice wind counterclockwise (clockwise), as shown in Fig. S1. In the space of these valley-orbital basis states, the Hamiltonian $\delta\hat{\mathcal{H}}$ (to be added to the pristine Hamiltonian $\hat{\mathcal{H}}_0$) can be constructed from valley Pauli matrices $\boldsymbol{\tau}$ and orbital Pauli matrices $\boldsymbol{\sigma}$, giving 16 possible terms to the Hamiltonian (including the trivial $\tau_0 \otimes \sigma_0$ term): $\delta\hat{\mathcal{H}} = \sum_{i,j\neq 0} \delta\mathcal{H}_{i,j}\tau_i \otimes \sigma_j$. Even though the original Hamiltonian of graphene has C_6 symmetry, we allow this to be broken by additional hopping terms (since rhombohedral multilayers do not have this symmetry to begin with). Instead, we study C_3 rotation symmetry around various high-symmetry centers. To start, we examine $C_3(\hexagon)$ symmetry, which is a threefold rotation about a hexagon center. In the valley-orbital basis, with ordering $\begin{pmatrix} KA & KB & K'A & K'B \end{pmatrix}$, the $C_3(\hexagon)$ operator takes the form

$$\hat{C}_3(\hexagon) = \exp\left(\frac{2\pi i}{3}\tau_3 \otimes \sigma_3\right) = \begin{pmatrix} \omega & 0 & 0 & 0 \\ 0 & \omega^\dagger & 0 & 0 \\ 0 & 0 & \omega^\dagger & 0 \\ 0 & 0 & 0 & \omega \end{pmatrix}, \tag{S3}$$

where $\omega = \exp(2\pi i/3)$ [1]. Applying this operator on all possible combinations of $\tau_i \otimes \sigma_j$, we find

$$\begin{aligned}
&\hat{C}_3(\hexagon)^\dagger \tau_0 \otimes \sigma_0 \hat{C}_3(\hexagon) = \tau_0 \otimes \sigma_0, \quad \hat{C}_3(\hexagon)^\dagger \tau_0 \otimes \sigma_3 \hat{C}_3(\hexagon) = \tau_0 \otimes \sigma_3, \quad \hat{C}_3(\hexagon)^\dagger \tau_1 \otimes \sigma_1 \hat{C}_3(\hexagon) = \tau_1 \otimes \sigma_1, \\
&\hat{C}_3(\hexagon)^\dagger \tau_1 \otimes \sigma_2 \hat{C}_3(\hexagon) = \tau_1 \otimes \sigma_2, \quad \hat{C}_3(\hexagon)^\dagger \tau_2 \otimes \sigma_1 \hat{C}_3(\hexagon) = \tau_2 \otimes \sigma_1, \quad \hat{C}_3(\hexagon)^\dagger \tau_2 \otimes \sigma_2 \hat{C}_3(\hexagon) = \tau_2 \otimes \sigma_2, \\
&\hat{C}_3(\hexagon)^\dagger \tau_3 \otimes \sigma_0 \hat{C}_3(\hexagon) = \tau_3 \otimes \sigma_0, \quad \hat{C}_3(\hexagon)^\dagger \tau_3 \otimes \sigma_3 \hat{C}_3(\hexagon) = \tau_3 \otimes \sigma_3, \\
&\hat{C}_3(\hexagon)^\dagger \tau_0 \otimes \sigma_1 \hat{C}_3(\hexagon) = -\frac{1}{2}\tau_0 \otimes \sigma_1 - \frac{\sqrt{3}}{2}\tau_3 \otimes \sigma_2, \quad \hat{C}_3(\hexagon)^\dagger \tau_3 \otimes \sigma_2 \hat{C}_3(\hexagon) = +\frac{\sqrt{3}}{2}\tau_0 \otimes \sigma_1 - \frac{1}{2}\tau_3 \otimes \sigma_2, \\
&\hat{C}_3(\hexagon)^\dagger \tau_0 \otimes \sigma_2 \hat{C}_3(\hexagon) = -\frac{1}{2}\tau_0 \otimes \sigma_2 + \frac{\sqrt{3}}{2}\tau_3 \otimes \sigma_1, \quad \hat{C}_3(\hexagon)^\dagger \tau_3 \otimes \sigma_1 \hat{C}_3(\hexagon) = -\frac{\sqrt{3}}{2}\tau_0 \otimes \sigma_2 - \frac{1}{2}\tau_3 \otimes \sigma_1, \\
&\hat{C}_3(\hexagon)^\dagger \tau_1 \otimes \sigma_0 \hat{C}_3(\hexagon) = -\frac{1}{2}\tau_1 \otimes \sigma_0 - \frac{\sqrt{3}}{2}\tau_2 \otimes \sigma_3, \quad \hat{C}_3(\hexagon)^\dagger \tau_2 \otimes \sigma_3 \hat{C}_3(\hexagon) = +\frac{\sqrt{3}}{2}\tau_1 \otimes \sigma_0 - \frac{1}{2}\tau_2 \otimes \sigma_3, \\
&\hat{C}_3(\hexagon)^\dagger \tau_1 \otimes \sigma_3 \hat{C}_3(\hexagon) = -\frac{1}{2}\tau_1 \otimes \sigma_3 - \frac{\sqrt{3}}{2}\tau_2 \otimes \sigma_0, \quad \hat{C}_3(\hexagon)^\dagger \tau_2 \otimes \sigma_0 \hat{C}_3(\hexagon) = +\frac{\sqrt{3}}{2}\tau_1 \otimes \sigma_3 - \frac{1}{2}\tau_2 \otimes \sigma_0.
\end{aligned} \tag{S4}$$

It might be possible to form invariant linear combinations of matrices that are rotated into each other in the above equation. However, it turns out that they are all trivial combinations. For example, consider this

$$\begin{aligned}
\hat{C}_3(\hexagon)^\dagger \left[a\tau_0 \otimes \sigma_1 + b\tau_3 \otimes \sigma_2\right] \hat{C}_3(\hexagon) &= a\left(-\frac{1}{2}\tau_0 \otimes \sigma_1 - \frac{\sqrt{3}}{2}\tau_3 \otimes \sigma_2\right) + b\left(+\frac{\sqrt{3}}{2}\tau_0 \otimes \sigma_1 - \frac{1}{2}\tau_3 \otimes \sigma_2\right) \\
&= \left(-\frac{a}{2} + \frac{\sqrt{3}b}{2}\right)\tau_0 \otimes \sigma_1 + \left(-\frac{\sqrt{3}a}{2} - \frac{b}{2}\right)\tau_3 \otimes \sigma_2.
\end{aligned} \tag{S5}$$

This leads to the following conditions on the complex numbers a (not the lattice constant) and b

$$a = -\frac{a}{2} + \frac{\sqrt{3}b}{2} \quad \text{and} \quad b = -\frac{\sqrt{3}a}{2} - \frac{b}{2}, \tag{S6}$$

which only has the trivial solution $(a, b) = (0, 0)$. Therefore, the only nontrivial $C_3(\hexagon)$-invariant terms to the Hamiltonian are

$$\begin{aligned}
&\text{Intravalley: } \sigma_3, \tau_3, \tau_3 \otimes \sigma_3, \\
&\text{Intervalley: } \tau_1 \otimes \sigma_1, \tau_1 \otimes \sigma_2, \tau_2 \otimes \sigma_1, \tau_2 \otimes \sigma_2.
\end{aligned} \tag{S7}$$

We note that all the intravalley terms are known to have simple real-space representations: σ_3 is a Semenoff mass, τ_3 is a valley Zeeman interaction (this is, actually, the term that we need to achieve a chiral phase by shifting the energy of the K valley relative to the K' valley), and $\tau_3 \otimes \sigma_3$ is the Haldane mass. It is also interesting to note that there are no intervalley terms that are diagonal in sublattice and also preserve $C_3(\hexagon)$ symmetry, i.e., we do not have $C_3(\hexagon)$-respecting τ_1 and τ_2. We can also classify the operators according to *spinless* time-reversal $\mathcal{T}$ symmetry (by assuming spin polarization, we are *always* breaking *physical, spinful* time-reversal symmetry), which is represented by

$$\hat{\mathcal{T}} = \tau_1 \mathcal{K}, \tag{S8}$$

where $\mathcal{K}$ is the complex conjugation operator. Spinless time-reversal symmetry is important because in order to have a nonzero Hall conductivity, this symmetry needs to be broken in addition to spinful time-reversal symmetry. The classification result is shown in Table SI.

We now repeat the above analysis for a three-fold rotation about a carbon site. If we choose the rotation center to be an A-site, denoted $C_3(\triangle)$, the symmetry operator in this case is

$$\hat{C}_3(\triangle) = \begin{pmatrix} 1 & 0 & 0 & 0 \\ 0 & \omega & 0 & 0 \\ 0 & 0 & 1 & 0 \\ 0 & 0 & 0 & \omega^\dagger \end{pmatrix}. \tag{S9}$$

If we instead choose a B-site, denoted $C_3(\triangledown)$, the symmetry operator is

$$\hat{C}_3(\triangledown) = \begin{pmatrix} \omega^\dagger & 0 & 0 & 0 \\ 0 & 1 & 0 & 0 \\ 0 & 0 & \omega & 0 \\ 0 & 0 & 0 & 1 \end{pmatrix} = \hat{M}_x \hat{C}_3(\triangle) \hat{M}_x, \tag{S10}$$

$C_3(\hexagon)$	$\mathcal{T}$ even	$\mathcal{T}$ odd
Intravalley	σ_3	$\tau_3, \tau_3 \otimes \sigma_3$
Intervalley	$\tau_1 \otimes \sigma_1, \tau_2 \otimes \sigma_1$	$\tau_1 \otimes \sigma_2, \tau_2 \otimes \sigma_2$
$C_3(\triangle)$	$\mathcal{T}$ even	$\mathcal{T}$ odd
Intravalley	σ_3	$\tau_3, \tau_3 \otimes \sigma_3$
Intervalley	$\tau_1 \otimes (\sigma_0 + \sigma_3), \tau_2 \otimes (\sigma_0 + \sigma_3)$	none
$C_3(\triangledown)$	$\mathcal{T}$ even	$\mathcal{T}$ odd
Intravalley	σ_3	$\tau_3, \tau_3 \otimes \sigma_3$
Intervalley	$\tau_1 \otimes (\sigma_0 - \sigma_3), \tau_2 \otimes (\sigma_0 - \sigma_3)$	none

Table SI. **Symmetry classification of operators in valley-orbital space.** $\mathcal{T}$ is spinless time-reversal symmetry. $C_3(\hexagon)$, $C_3(\triangle)$, and $C_3(\triangledown)$ are threefold rotation symmetries about a hexagon center, an A site, and a B site, respectively.

where $\hat{M}_x = \tau_1 \otimes \sigma_1$. The action of these operators on the Pauli matrices is

$$
\begin{aligned}
&\hat{C}_3(\triangle)^\dagger \tau_0 \otimes \sigma_0 \hat{C}_3(\triangle) = \tau_0 \otimes \sigma_0, \quad \hat{C}_3(\triangle)^\dagger \tau_3 \otimes \sigma_0 \hat{C}_3(\triangle) = \tau_3 \otimes \sigma_0,\\
&\hat{C}_3(\triangle)^\dagger \tau_0 \otimes \sigma_3 \hat{C}_3(\triangle) = \tau_0 \otimes \sigma_3, \quad \hat{C}_3(\triangle)^\dagger \tau_3 \otimes \sigma_3 \hat{C}_3(\triangle) = \tau_3 \otimes \sigma_3,\\
&\hat{C}_3(\triangle)^\dagger \tau_0 \otimes \sigma_1 \hat{C}_3(\triangle) = -\frac{1}{2}\tau_0 \otimes \sigma_1 - \frac{\sqrt{3}}{2}\tau_3 \otimes \sigma_2, \quad \hat{C}_3(\triangle)^\dagger \tau_3 \otimes \sigma_2 \hat{C}_3(\triangle) = +\frac{\sqrt{3}}{2}\tau_0 \otimes \sigma_1 - \frac{1}{2}\tau_3 \otimes \sigma_2,\\
&\hat{C}_3(\triangle)^\dagger \tau_0 \otimes \sigma_2 \hat{C}_3(\triangle) = -\frac{1}{2}\tau_0 \otimes \sigma_2 + \frac{\sqrt{3}}{2}\tau_3 \otimes \sigma_1, \quad \hat{C}_3(\triangle)^\dagger \tau_3 \otimes \sigma_1 \hat{C}_3(\triangle) = -\frac{\sqrt{3}}{2}\tau_0 \otimes \sigma_2 - \frac{1}{2}\tau_3 \otimes \sigma_1,\\
&\hat{C}_3(\triangle)^\dagger \tau_1 \otimes \sigma_1 \hat{C}_3(\triangle) = -\frac{1}{2}\tau_1 \otimes \sigma_1 + \frac{\sqrt{3}}{2}\tau_2 \otimes \sigma_1, \quad \hat{C}_3(\triangle)^\dagger \tau_2 \otimes \sigma_1 \hat{C}_3(\triangle) = -\frac{\sqrt{3}}{2}\tau_1 \otimes \sigma_1 - \frac{1}{2}\tau_2 \otimes \sigma_1,\\
&\hat{C}_3(\triangle)^\dagger \tau_1 \otimes \sigma_2 \hat{C}_3(\triangle) = -\frac{1}{2}\tau_1 \otimes \sigma_2 + \frac{\sqrt{3}}{2}\tau_2 \otimes \sigma_2, \quad \hat{C}_3(\triangle)^\dagger \tau_2 \otimes \sigma_2 \hat{C}_3(\triangle) = -\frac{\sqrt{3}}{2}\tau_1 \otimes \sigma_2 - \frac{1}{2}\tau_2 \otimes \sigma_2,\\
&\hat{C}_3(\triangle)^\dagger \tau_1 \otimes \sigma_0 \hat{C}_3(\triangle) = \frac{1}{4}\tau_1 \otimes \sigma_0 + \frac{3}{4}\tau_1 \otimes \sigma_3 - \frac{\sqrt{3}}{4}\tau_2 \otimes \sigma_0 + \frac{\sqrt{3}}{4}\tau_2 \otimes \sigma_3,\\
&\hat{C}_3(\triangle)^\dagger \tau_1 \otimes \sigma_3 \hat{C}_3(\triangle) = \frac{3}{4}\tau_1 \otimes \sigma_0 + \frac{1}{4}\tau_1 \otimes \sigma_3 + \frac{\sqrt{3}}{4}\tau_2 \otimes \sigma_0 - \frac{\sqrt{3}}{4}\tau_2 \otimes \sigma_3,\\
&\hat{C}_3(\triangle)^\dagger \tau_2 \otimes \sigma_0 \hat{C}_3(\triangle) = \frac{\sqrt{3}}{4}\tau_1 \otimes \sigma_0 - \frac{\sqrt{3}}{4}\tau_1 \otimes \sigma_3 + \frac{1}{4}\tau_2 \otimes \sigma_0 + \frac{3}{4}\tau_2 \otimes \sigma_3,\\
&\hat{C}_3(\triangle)^\dagger \tau_2 \otimes \sigma_3 \hat{C}_3(\triangle) = -\frac{\sqrt{3}}{4}\tau_1 \otimes \sigma_0 + \frac{\sqrt{3}}{4}\tau_1 \otimes \sigma_3 + \frac{3}{4}\tau_2 \otimes \sigma_0 + \frac{1}{4}\tau_2 \otimes \sigma_3.
\end{aligned}
\tag{S11}
$$

By computing possible linear combinations of operators that are rotated into each other to search for invariant combinations, we find the following

$$
\begin{aligned}
&\text{Intravalley: } \tau_3, \sigma_3, \tau_3 \otimes \sigma_3,\\
&\text{Intervalley: } \tau_1 \otimes \sigma_0 + \tau_1 \otimes \sigma_3, \tau_2 \otimes \sigma_0 + \tau_2 \otimes \sigma_3.
\end{aligned}
\tag{S12}
$$

In contrast to $C_3(\hexagon)$-invariant couplings, we do not have $\tau_1 \otimes \sigma_1$, $\tau_1 \otimes \sigma_2$, $\tau_2 \otimes \sigma_1$, and $\tau_2 \otimes \sigma_2$ in the present case, Instead, $\tau_1 \otimes (\sigma_0 + \sigma_3)$ and $\tau_2 \otimes (\sigma_0 + \sigma_3)$ are invariant under $C_3(\triangle)$ symmetry but not under $C_3(\hexagon)$ symmetry. We note that $(\sigma_0 + \sigma_3)/2 = \begin{pmatrix} 1 & 0 \\ 0 & 0 \end{pmatrix}$ is the projector to the A sublattice; so $\tau_1 \otimes (\sigma_0 + \sigma_3)$ and $\tau_2 \otimes (\sigma_0 + \sigma_3)$ are realizations of τ_1 and τ_2 if we consider only one sublattice, i.e. by considering a triangular lattice instead of a honeycomb lattice. To obtain the invariant terms under $\hat{C}_3(\triangledown)$, we simply apply the mirror operator $\hat{M}_x$ to the $\hat{C}_3(\triangle)$-invariant terms to find

$$
\begin{aligned}
&\text{Intravalley: } \tau_3, \sigma_3, \tau_3 \otimes \sigma_3,\\
&\text{Intervalley: } \tau_1 \otimes \sigma_0 - \tau_1 \otimes \sigma_3, \tau_2 \otimes \sigma_0 - \tau_2 \otimes \sigma_3.
\end{aligned}
\tag{S13}
$$

In this case, we find τ_1 and τ_2 projected to the B sublattice, as represented by the projector $(\sigma_0 - \sigma_3)/2 = \begin{pmatrix} 0 & 0 \\ 0 & 1 \end{pmatrix}$.

It is worth emphasizing that in the preceding analysis, we have only classified symmetry-allowed terms that are finite at exactly the K and K' points; there may be momentum-dependent terms that respect the symmetries enumerated above but which vanish

as momentum approaches the zone corners. These momentum-dependent terms are not captured in our present analysis. Since we are interested in strong intervalley coupling that yields intervalley-mixed states, we suspect that the dominant terms are the ones which remain finite exactly at K and K', hence our choice to neglect momentum-dependent terms. That said, the other terms might be important as well, but we postpone their analysis to future works.

2. *Kekule Basis States and $C_3(\bigcirc)$ Symmetry-Allowed Intervalley Terms*

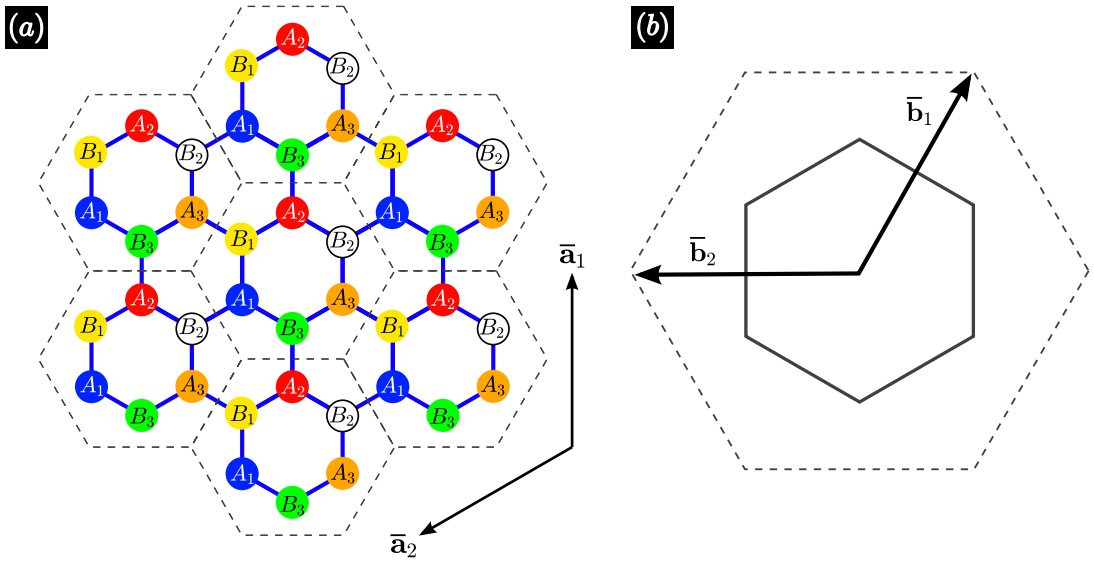

Figure S2. $\sqrt{3}\times\sqrt{3}$ **reconstructed unit cell.** (a) Real-space lattice with each unit cell, enclosed by dashed hexagons, consisting of six atoms. (b) Brillouin zone (solid hexagon) has been dilated by a factor of $1/3$ compared to the original Brillouin zone (dashed hexagon).

Now that we have the complete classification of all symmetry-allowed terms, let us find explicit real-space representations for each of them. To do this, we implement an enlargement of the unit cell to include six orbitals as shown in Fig. S2(a). The lattice vectors for the enlarged unit cells are $\overline{\mathbf{a}}_1 = \sqrt{3}a\,(0,1)$ and $\overline{\mathbf{a}}_2 = \sqrt{3}a\left(-\sqrt{3}/2,-1/2\right)$. The lattice constant is now $\sqrt{3}a$. The corresponding reciprocal lattice vectors are $\overline{\mathbf{b}}_1 = 4\pi/3a\left(-1/2,\sqrt{3}/2\right)$ and $\overline{\mathbf{b}}_2 = 4\pi/3a\,(-1,0)$. We notice that $\mathbf{K}_\tau = -\tau\overline{\mathbf{b}}_2$, implying that both Dirac cones are zone-folded back to the $\overline{\Gamma}$ point in the new Brillouin zone, as advertised. Since both valleys are folded to the same point, we do not need to consider the valleys separately, which, of course, is the rationale for considering this augmented basis in the first place. In the augmented basis, $\begin{pmatrix}A_1 & B_1 & A_2 & B_2 & A_3 & B_3\end{pmatrix}$, the unperturbed Hamiltonian is just

$$\hat{\mathcal{H}}_0(\mathbf{k}) = t_0\begin{pmatrix} 0 & e^{i\mathbf{k}\cdot\boldsymbol{\delta}_1} & 0 & e^{i\mathbf{k}\cdot\boldsymbol{\delta}_2} & 0 & e^{i\mathbf{k}\cdot\boldsymbol{\delta}_3} \\ e^{-i\mathbf{k}\cdot\boldsymbol{\delta}_1} & 0 & e^{-i\mathbf{k}\cdot\boldsymbol{\delta}_2} & 0 & e^{-i\mathbf{k}\cdot\boldsymbol{\delta}_3} & 0 \\ 0 & e^{i\mathbf{k}\cdot\boldsymbol{\delta}_2} & 0 & e^{i\mathbf{k}\cdot\boldsymbol{\delta}_3} & 0 & e^{i\mathbf{k}\cdot\boldsymbol{\delta}_1} \\ e^{-i\mathbf{k}\cdot\boldsymbol{\delta}_2} & 0 & e^{-i\mathbf{k}\cdot\boldsymbol{\delta}_3} & 0 & e^{-i\mathbf{k}\cdot\boldsymbol{\delta}_1} & 0 \\ 0 & e^{i\mathbf{k}\cdot\boldsymbol{\delta}_3} & 0 & e^{i\mathbf{k}\cdot\boldsymbol{\delta}_1} & 0 & e^{i\mathbf{k}\cdot\boldsymbol{\delta}_2} \\ e^{-i\mathbf{k}\cdot\boldsymbol{\delta}_3} & 0 & e^{-i\mathbf{k}\cdot\boldsymbol{\delta}_1} & 0 & e^{-i\mathbf{k}\cdot\boldsymbol{\delta}_2} & 0 \end{pmatrix}, \tag{S14}$$

where $\boldsymbol{\delta}_1 = (0,1)a/\sqrt{3}$, $\boldsymbol{\delta}_2 = (-\sqrt{3}/2,-1/2)a/\sqrt{3}$, and $\boldsymbol{\delta}_3 = (\sqrt{3}/2,-1/2)a/\sqrt{3}$ are the nearest-neighbor vectors. In this representation, the valley states are represented by (referring to Figs. S1 and S2 for visual aid)

$$|\psi_A(\mathbf{K})\rangle = \frac{1}{\sqrt{3}}\begin{pmatrix}1\\0\\\omega\\0\\\omega^\dagger\\0\end{pmatrix}, \quad |\psi_B(\mathbf{K})\rangle = \frac{1}{\sqrt{3}}\begin{pmatrix}0\\1\\0\\\omega^\dagger\\0\\\omega\end{pmatrix} \quad |\psi_A(\mathbf{K}')\rangle = \frac{1}{\sqrt{3}}\begin{pmatrix}1\\0\\\omega^\dagger\\0\\\omega\\0\end{pmatrix}, \quad |\psi_B(\mathbf{K}')\rangle = \frac{1}{\sqrt{3}}\begin{pmatrix}0\\1\\0\\\omega\\0\\\omega^\dagger\end{pmatrix}. \tag{S15}$$

We have verified explicitly that $\hat{\mathcal{H}}(\mathbf{0})\,|\psi_\sigma(\mathbf{K}_\tau)\rangle = 0$, demonstrating the valley states are indeed mapped to $\overline{\Gamma}$. Now, anticipating

the $C_3(\hexagon)$-symmetric intervalley terms are all intersublattice, we write the perturbation Hamiltonian as

$$\delta\hat{\mathcal{H}}_{\tau_i\otimes\sigma_j}(\mathbf{k}=\mathbf{0}) = \begin{pmatrix} 0 & f_1 & 0 & f_2 & 0 & f_3 \\ f_1^\dagger & 0 & f_4 & 0 & f_5 & 0 \\ 0 & f_4^\dagger & 0 & f_6 & 0 & f_7 \\ f_2^\dagger & 0 & f_6^\dagger & 0 & f_8 & 0 \\ 0 & f_5^\dagger & 0 & f_8^\dagger & 0 & f_9 \\ f_3^\dagger & 0 & f_7^\dagger & 0 & f_9^\dagger & 0 \end{pmatrix}, \tag{S16}$$

where f_i are complex numbers. In this basis, $C_3(\hexagon)$ symmetry is represented by

$$\hat{C}_3(\hexagon) = \begin{pmatrix} 0 & 0 & 1 & 0 & 0 & 0 \\ 0 & 0 & 0 & 1 & 0 & 0 \\ 0 & 0 & 0 & 0 & 1 & 0 \\ 0 & 0 & 0 & 0 & 0 & 1 \\ 1 & 0 & 0 & 0 & 0 & 0 \\ 0 & 1 & 0 & 0 & 0 & 0 \end{pmatrix}. \tag{S17}$$

Invariance under $C_3(\hexagon)$ symmetry requires the following

$$a = f_1 = f_6 = f_9, \quad b = f_2 = f_5^\dagger = f_7, \quad \text{and} \quad c = f_3 = f_4^\dagger = f_8^\dagger. \tag{S18}$$

So perturbation Hamiltonian now simplifies significantly to

$$\delta\hat{\mathcal{H}}_{\tau_i\otimes\sigma_j}(\mathbf{k}=\mathbf{0}) = \begin{pmatrix} 0 & a & 0 & b & 0 & c \\ a^\dagger & 0 & c^\dagger & 0 & b^\dagger & 0 \\ 0 & c & 0 & a & 0 & b \\ b^\dagger & 0 & a^\dagger & 0 & c^\dagger & 0 \\ 0 & b & 0 & c & 0 & a \\ c^\dagger & 0 & b^\dagger & 0 & a^\dagger & 0 \end{pmatrix}. \tag{S19}$$

Projecting this into the basis defined by Eq. (S15), we find that the Hamiltonian takes the form

$$\delta\hat{\mathcal{H}}_{\tau_i\otimes\sigma_j}(\mathbf{k}=\mathbf{0}) = \begin{pmatrix} 0 & 0 & 0 & a+\omega b+\omega^\dagger c \\ 0 & 0 & a^\dagger+\omega b^\dagger+\omega^\dagger c^\dagger & 0 \\ 0 & a+\omega^\dagger b+\omega c & 0 & 0 \\ a^\dagger+\omega^\dagger b^\dagger+\omega c^\dagger & 0 & 0 & 0 \end{pmatrix}. \tag{S20}$$

Now, by choosing appropriate complex numbers a, b, c, we can realize any of the symmetry-allowed terms. If we define $a = a_r + ia_i$, $b = b_r + ib_i$, and $c = c_r + ic_i$, we can write the Hamiltonian generically as

$$\delta\hat{\mathcal{H}}_{\tau_i\otimes\sigma_j}(\mathbf{k}=\mathbf{0}) = \left[a_r - \frac{b_r}{2} - \frac{c_r}{2}\right]\tau_1\otimes\sigma_1 + \left[\frac{b_i}{2} + \frac{c_i}{2} - a_i\right]\tau_1\otimes\sigma_2 + \left[\frac{\sqrt{3}c_r - \sqrt{3}b_r}{2}\right]\tau_2\otimes\sigma_1 + \left[\frac{\sqrt{3}b_i - \sqrt{3}c_i}{2}\right]\tau_2\otimes\sigma_2. \tag{S21}$$

Notice that the $\mathcal{T}$-even terms are associated with real hoppings while the $\mathcal{T}$-odd terms are associated with imaginary hoppings, as we would expect. Using this, we have the following special cases where each term in Eq. (S21) is isolated:

$$\begin{aligned} &\tau_1\otimes\sigma_1 : b = c = 0, a = a_r, \\ &\tau_1\otimes\sigma_2 : b = c = 0, a = a_i, \\ &\tau_2\otimes\sigma_1 : a_i = b_i = c_i = 0, 2a_r = b_r + c_r, b_r \neq c_r, \\ &\tau_2\otimes\sigma_2 : a_r = b_r = c_r = 0, 2a_i = b_i + c_i, b_i \neq c_i. \end{aligned} \tag{S22}$$

Terms involving $\tau_1\otimes\sigma_1$ and $\tau_1\otimes\sigma_2$ consist of modulation of the bonds around the hexagon of a single unit cell, as shown in Fig. S3(b). For example, we can have alternating double and single bonds around the hexagon similar to the resonance bonding structures of benzene. On the other hand, terms involving $\tau_2\otimes\sigma_1$ and $\tau_2\otimes\sigma_2$ consist of modulation of both intracell and intercell bonds, as shown in Fig. S3(c). In particular, for any triad of nearest-neighbor bonds, one must be the average of the other two.

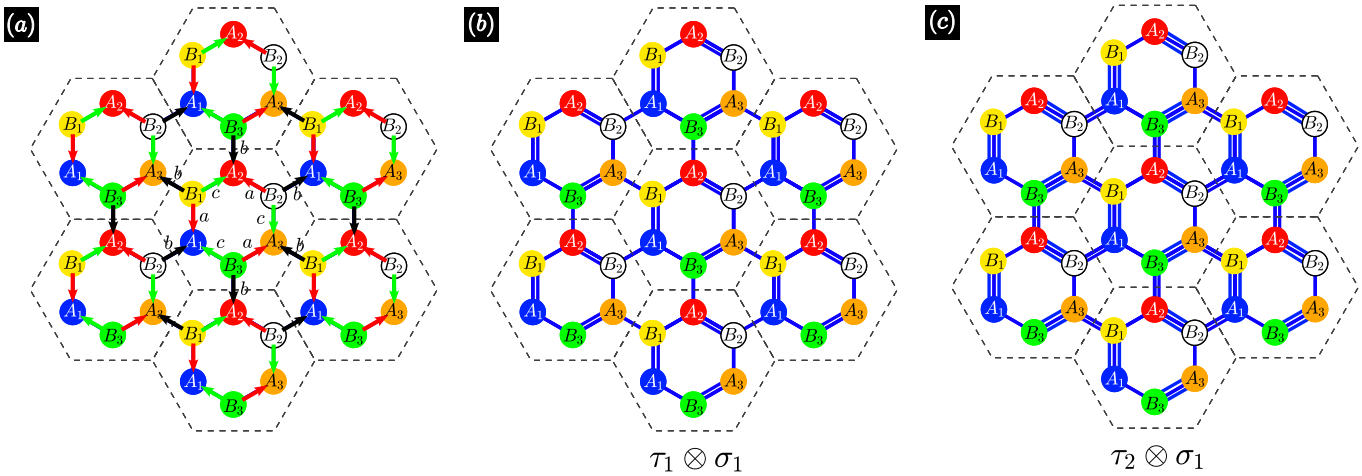

Figure S3. **Real-space representation of $C_3(\bigcirc)$ symmetric intervalley scattering on a honeycomb lattice.** (a) Directed hoppings are indicated by arrows, with notation specified in Eq. (S18). (b) Example of a tight-binding model that realizes the $\tau_1 \otimes \sigma_1$ interaction. Intracell bonds show benzene-like bond-strength modulation. (c) Example of a tight-binding model that realizes the $\tau_2 \otimes \sigma_1$ interaction, which involves modulation of both intracell and intercell bonds.

For illustration, let us consider one concrete example with the following Hamiltonian

$$\hat{\mathcal{H}}(\mathbf{k}) = \begin{pmatrix} 0 & (t_0+t_1)e^{i\mathbf{k}\cdot\boldsymbol{\delta}_1} & 0 & t_0 e^{i\mathbf{k}\cdot\boldsymbol{\delta}_2} & 0 & t_0 e^{i\mathbf{k}\cdot\boldsymbol{\delta}_3} \\ (t_0+t_1)e^{-i\mathbf{k}\cdot\boldsymbol{\delta}_1} & 0 & t_0 e^{-i\mathbf{k}\cdot\boldsymbol{\delta}_2} & 0 & t_0 e^{-i\mathbf{k}\cdot\boldsymbol{\delta}_3} & 0 \\ 0 & t_0 e^{i\mathbf{k}\cdot\boldsymbol{\delta}_2} & 0 & (t_0+t_1)e^{i\mathbf{k}\cdot\boldsymbol{\delta}_3} & 0 & t_0 e^{i\mathbf{k}\cdot\boldsymbol{\delta}_1} \\ t_0 e^{-i\mathbf{k}\cdot\boldsymbol{\delta}_2} & 0 & (t_0+t_1)e^{-i\mathbf{k}\cdot\boldsymbol{\delta}_3} & 0 & t_0 e^{-i\mathbf{k}\cdot\boldsymbol{\delta}_1} & 0 \\ 0 & t_0 e^{i\mathbf{k}\cdot\boldsymbol{\delta}_3} & 0 & t_0 e^{i\mathbf{k}\cdot\boldsymbol{\delta}_1} & 0 & (t_0+t_1)e^{i\mathbf{k}\cdot\boldsymbol{\delta}_2} \\ t_0 e^{-i\mathbf{k}\cdot\boldsymbol{\delta}_3} & 0 & t_0 e^{-i\mathbf{k}\cdot\boldsymbol{\delta}_1} & 0 & (t_0+t_1)e^{-i\mathbf{k}\cdot\boldsymbol{\delta}_2} & 0 \end{pmatrix}. \tag{S23}$$

The eigenstates of this Hamiltonian at $\mathbf{k} = \mathbf{0}$ are

$$\begin{aligned} E_1 &= -3t_0 - t_1, & |\psi_1\rangle &= \left(-1 \;\; 1 \;\; -1 \;\; 1 \;\; -1 \;\; 1\right)/\sqrt{6}, \\ E_2 &= -t_1, & |\psi_2\rangle &= \left(1 \;\; -1 \;\; 0 \;\; 0 \;\; -1 \;\; 1\right)/\sqrt{4}, \\ E_3 &= -t_1, & |\psi_3\rangle &= \left(1 \;\; -1 \;\; -1 \;\; 1 \;\; 0 \;\; 0\right)/\sqrt{4}, \\ E_4 &= +t_1, & |\psi_4\rangle &= \left(-1 \;\; -1 \;\; 0 \;\; 0 \;\; 1 \;\; 1\right)/\sqrt{4}, \\ E_5 &= +t_1, & |\psi_5\rangle &= \left(-1 \;\; -1 \;\; 1 \;\; 1 \;\; 0 \;\; 0\right)/\sqrt{4}, \\ E_6 &= +3t_0 + t_1, & |\psi_6\rangle &= \left(1 \;\; 1 \;\; 1 \;\; 1 \;\; 1 \;\; 1\right)/\sqrt{6}. \end{aligned}$$

$|\psi_1\rangle$ and $|\psi_6\rangle$ are high-energy states that we shall neglect when only states near the Dirac cones matter to the physics (i.e. the entirety of this work). States near $E = 0$ are doubly-degenerate and are hybridized from the valley-polarized states. Actually, this statement requires further inspection because it is possible that even though these states have no appearance of valley polarization, perhaps there are linear combinations of them which are valley-polarized. To prove that this is *not* the case and that these degenerate states are indeed intervalley-hybridized (i.e. not valley-polarized) states, we calculate the valley character of the linear combination $|\psi\rangle = \alpha\,|\psi_2\rangle + \beta e^{i\vartheta}\,|\psi_3\rangle$, where $\alpha \geq 0, \beta \geq 0, \vartheta$ $(\alpha^2 + \beta^2 = 1)$ are real numbers to be extremized for maximal valley polarization:

$$|\langle\psi|\psi_A(\mathbf{K})\rangle|^2 + |\langle\psi|\psi_B(\mathbf{K})\rangle|^2 = |\langle\psi|\psi_A(\mathbf{K}')\rangle|^2 + |\langle\psi|\psi_B(\mathbf{K}')\rangle|^2 = \frac{1+\alpha\beta\cos\vartheta}{2} \leq \frac{3}{4}, \tag{S24}$$

The maximal value of cosine is $\cos\vartheta = 1$. For these values of ϑ, the numerator is $1 + \alpha\sqrt{1-\alpha^2}$, which is maximal for $\alpha = \beta = 1/\sqrt{2}$. The overlaps with valley states are therefore bounded by $3/4$, showing that these states are indeed intervalley-coherent states.

3. $C_3(\triangle)$ Symmetry-Allowed Intervalley Terms

In this section, we write down all the symmetry-allowed terms consistent with $C_3(\triangle)$ symmetry acting on the A sublattice only. The most general such Hamiltonian is

$$\delta\hat{\mathcal{H}}_{\tau_i\otimes(\sigma_0+\sigma_3)}(\mathbf{k}=\mathbf{0})=\begin{pmatrix} f_1 & 0 & a_r+ia_i & 0 & b_r+ib_i & 0\\ 0 & 0 & 0 & 0 & 0 & 0\\ a_r-ia_i & 0 & f_2 & 0 & c_r+ic_i & 0\\ 0 & 0 & 0 & 0 & 0 & 0\\ b_r-ib_i & 0 & c_r-ic_i & 0 & f_3 & 0\\ 0 & 0 & 0 & 0 & 0 & 0 \end{pmatrix}, \tag{S25}$$

where the diagonal elements are required to be real by Hermiticity while the off-diagonal elements can be complex in general. In the Kekule basis, the symmetry operator for $C_3(\triangle)$ is

$$\hat{C}_3(\triangle)=\begin{pmatrix} 1&0&0&0&0&0\\ 0&0&0&0&0&1\\ 0&0&1&0&0&0\\ 0&1&0&0&0&0\\ 0&0&0&0&1&0\\ 0&0&0&1&0&0 \end{pmatrix}. \tag{S26}$$

We notice this operator matrix contains an invariant submatrix (a 3×3 identity submatrix). Therefore, it immediately follows that $\hat{C}_3(\triangle)^\dagger\delta\hat{\mathcal{H}}_{\tau_i\otimes(\sigma_0+\sigma_3)}(\mathbf{k}=\mathbf{0})\hat{C}_3(\triangle)=\delta\hat{\mathcal{H}}_{\tau_i\otimes(\sigma_0+\sigma_3)}(\mathbf{k}=\mathbf{0})$. Projecting this Hamiltonian to the valley-orbital basis, we find

$$\begin{aligned}\delta\hat{\mathcal{H}}_{\tau_i\otimes(\sigma_0+\sigma_3)}(\mathbf{k}=\mathbf{0})=\Bigg[&\frac{1}{6}\left(f_1+f_2+f_3-a_r-b_r-c_r\right)\tau_0+\frac{1}{12}\left(2f_1-f_2-f_3-2a_r-2b_r+4c_r\right)\tau_1\\ &\frac{1}{4\sqrt{3}}\left(f_3-f_2+2a_r-2b_r\right)\tau_2+\frac{1}{2\sqrt{3}}\left(-a_i+b_i-c_i\right)\tau_3\Bigg]\otimes\left[\sigma_0+\sigma_3\right].\end{aligned} \tag{S27}$$

The diagonal elements (f_1,f_2,f_3) can originate from on-site potentials or from *next*-nearest intra-sublattice hoppings. This means that we can obtain intervalley interaction even from purely local charge modulation on the reconstructed Kekule lattice. For example, by setting $f_1=a=b=c=0$, we have

$$\delta\hat{\mathcal{H}}_{\tau_i\otimes(\sigma_0+\sigma_3)}(\mathbf{k}=\mathbf{0})=\left[\frac{1}{6}\left(f_2+f_3\right)\tau_0-\frac{1}{12}\left(f_2+f_3\right)\tau_1+\frac{1}{4\sqrt{3}}\left(f_3-f_2\right)\tau_2\right]\otimes\left[\sigma_0+\sigma_3\right] \tag{S28}$$

On the other hand, with nearest-neighbor intra-sublattice hoppings, we can have a τ_3 coupling from the imaginary parts of a,b,c. While τ_1,τ_2 describe intervalley scattering, τ_3 describes valley imbalance. This means that simultaneously varying the real and imaginary parts of a,b,c, we can model both intervalley hybridization and valley polarization in the same model. For example, by setting $f_1=f_2=f_3=0$, we have

$$\delta\hat{\mathcal{H}}_{\tau_i\otimes(\sigma_0+\sigma_3)}(\mathbf{k}=\mathbf{0})=\frac{1}{6}\left[\left(-a_r-b_r-c_r\right)\tau_0+\left(2c_r-a_r-b_r\right)\tau_1+\sqrt{3}\left(a_r-b_r\right)\tau_2+\sqrt{3}\left(-a_i+b_i-c_i\right)\tau_3\right]\otimes\left[\sigma_0+\sigma_3\right]. \tag{S29}$$

We set $a_r=-b_r-c_r$ to eliminate the τ_0 term and also assume $a_i=b_i=0$ since we only need c_i to control the τ_3 term. By identifying $c=t_2e^{i\varphi}$ and $b_r=t_1$, we have

$$\delta\hat{\mathcal{H}}_{\tau_i\otimes(\sigma_0+\sigma_3)}(\mathbf{k}=\mathbf{0})=\left[t_2\cos\varphi\tau_1-\frac{2t_1+t_2\cos\varphi}{\sqrt{3}}\tau_2-\frac{t_2\sin\varphi}{\sqrt{3}}\tau_3\right]\otimes\frac{\sigma_0+\sigma_3}{2}. \tag{S30}$$

By tuning t_1, t_2, and φ, we can go from τ_1 to τ_2 to τ_3. The first two terms are even under $\mathcal{T}$ symmetry while the final term is odd under $\mathcal{T}$ symmetry. For $\varphi=0,\pi$, we recover $\mathcal{T}$ symmetry, which is sensible because these are the limits where all of the hoppings are real.

We end this section by mentioning that while terms involving τ_1 and τ_2 necessarily require at least a $\sqrt{3}\times\sqrt{3}$ reconstruction to coherently mix the valleys, terms involving τ_3 are intravalley and do not require such a reconstruction, even though the example above does involve a Kekule lattice. A famous example is the Haldane model. In the hexagonal Brillouin zone, it is given by

$$\delta\hat{\mathcal{H}}_{\tau_3}(\mathbf{k})=\frac{2m_z}{3\sqrt{3}}\sum_{i=1}^{3}\sin\left[\mathbf{k}\cdot\mathbf{a}_i\right]\sigma_3\rightarrow\delta\hat{\mathcal{H}}_{\tau_3}(\mathbf{k}=\mathbf{0})=-m_z\tau_3\otimes\sigma_3. \tag{S31}$$

We can modify this Hamiltonian to have the desired sublattice structure by replacing σ_3 with the appropriate σ matrices. We will use the Haldane model to simulate valley imbalance since it is simpler.

4. General Transformation Between Valley-Orbital Basis and Kekule Basis

Here, we provide a prescription to transform between the two basis sets by classifying every possible perturbation without any symmetry constraint in the valley-orbital basis. We start with a few examples. Let us write down tight-binding Hamiltonians that realize $\tau_1 \otimes \sigma_0$, $\tau_1 \otimes \sigma_3$, $\tau_2 \otimes \sigma_0$, and $\tau_2 \otimes \sigma_3$ and show explicitly that they break $C_3(\hexagon)$ symmetry, consistent with our preceding analysis. Both of these terms must hop only within the A or B sublattice of the original unit cell (not the Kekule unit cell). The following Hamiltonian realizes the $\tau_1 \otimes \sigma_0$ and $\tau_1 \otimes \sigma_3$ interactions

$$\delta\hat{\mathcal{H}}_{\tau_1}(\mathbf{k}=\mathbf{0}) = \begin{pmatrix} 0 & 0 & t_1 & 0 & t_1 & 0 \\ 0 & 0 & 0 & t_2 & 0 & t_2 \\ t_1 & 0 & 0 & 0 & -2t_1 & 0 \\ 0 & t_2 & 0 & 0 & 0 & -2t_2 \\ t_1 & 0 & -2t_1 & 0 & 0 & 0 \\ 0 & t_2 & 0 & -2t_2 & 0 & 0 \end{pmatrix} = -(t_1+t_2)\tau_1 \otimes \sigma_0 - (t_1-t_2)\tau_1 \otimes \sigma_3. \tag{S32}$$

On the other hand, the following Hamiltonian realizes the $\tau_2 \otimes \sigma_0$ and $\tau_2 \otimes \sigma_3$ interactions

$$\delta\hat{\mathcal{H}}_{\tau_2}(\mathbf{k}=\mathbf{0}) = \begin{pmatrix} 0 & 0 & t_1 & 0 & -t_1 & 0 \\ 0 & 0 & 0 & t_2 & 0 & -t_2 \\ t_1 & 0 & 0 & 0 & 0 & 0 \\ 0 & t_2 & 0 & 0 & 0 & 0 \\ -t_1 & 0 & 0 & 0 & 0 & 0 \\ 0 & -t_2 & 0 & 0 & 0 & 0 \end{pmatrix} = \frac{1}{\sqrt{3}}(t_1-t_2)\tau_2 \otimes \sigma_0 + \frac{1}{\sqrt{3}}(t_1+t_2)\tau_2 \otimes \sigma_3. \tag{S33}$$

We have checked explicitly that these two Hamiltonians do not preserve $C_3(\hexagon)$ symmetry by confirming that $\hat{C}_3(\hexagon)^\dagger \delta\hat{\mathcal{H}}_{\tau_i} \hat{C}_3(\hexagon) \neq \delta\hat{\mathcal{H}}_{\tau_i}$. However, these can be made to respect $C_3(\triangle)$ symmetry by setting $t_2 = 0$. Finally, we consider the most general perturbation of the form

$$\hat{\mathcal{H}}(\mathbf{k}=\mathbf{0}) = \sum_{\mu=0}^{8}\sum_{\nu=0}^{3} t_{\mu\nu}\lambda_\mu \otimes \sigma_\nu, \tag{S34}$$

where λ_μ are the Gell-Mann matrices that form the basis for the Lie algebra of $SU(3)$ and $t_{\mu\nu}$ are 36 real parameters the describe both hoppings and on-site energies. The nine Gell-Mann matrices are

$$\begin{aligned} &\lambda_0 = \sqrt{\frac{2}{3}}\begin{pmatrix} 1 & 0 & 0 \\ 0 & 1 & 0 \\ 0 & 0 & 1 \end{pmatrix} \quad \lambda_1 = \begin{pmatrix} 0 & 1 & 0 \\ 1 & 0 & 0 \\ 0 & 0 & 0 \end{pmatrix} \quad \lambda_2 = \begin{pmatrix} 0 & -i & 0 \\ i & 0 & 0 \\ 0 & 0 & 0 \end{pmatrix} \quad \lambda_3 = \begin{pmatrix} 1 & 0 & 0 \\ 0 & -1 & 0 \\ 0 & 0 & 0 \end{pmatrix} \quad \lambda_4 = \begin{pmatrix} 0 & 0 & 1 \\ 0 & 0 & 0 \\ 1 & 0 & 0 \end{pmatrix} \\ &\lambda_5 = \begin{pmatrix} 0 & 0 & -i \\ 0 & 0 & 0 \\ i & 0 & 0 \end{pmatrix} \quad \lambda_6 = \begin{pmatrix} 0 & 0 & 0 \\ 0 & 0 & 1 \\ 0 & 1 & 0 \end{pmatrix} \quad \lambda_7 = \begin{pmatrix} 0 & 0 & 0 \\ 0 & 0 & -i \\ 0 & i & 0 \end{pmatrix} \quad \lambda_8 = \frac{1}{\sqrt{3}}\begin{pmatrix} 1 & 0 & 0 \\ 0 & 1 & 0 \\ 0 & 0 & -2 \end{pmatrix}. \end{aligned} \tag{S35}$$

Like the Pauli matrices, these Gell-Mann matrices satisfy $\mathrm{Tr}\{\lambda_\mu\lambda_\nu\} = 2\delta_{\mu\nu}$. The previous examples can be written in terms of these Gell-Mann matrices, using the notation in Eqs. (S19), (S32), and (S33),

$$\begin{aligned} \delta\hat{\mathcal{H}}_{\tau_i\otimes\sigma_j}(\mathbf{k}=\mathbf{0}) &= \sqrt{\frac{3}{2}}a_r\lambda_0 \otimes \sigma_1 - \sqrt{\frac{3}{2}}a_i\lambda_0 \otimes \sigma_2 \\ &\quad + \frac{1}{2}(b_r+c_r)\left(\lambda_1+\lambda_4+\lambda_6\right)\otimes\sigma_1 + \frac{1}{2}(b_r-c_r)\left(-\lambda_2+\lambda_5-\lambda_7\right)\otimes\sigma_2 \\ &\quad + \frac{1}{2}(b_i-c_i)\left(-\lambda_2+\lambda_5-\lambda_7\right)\otimes\sigma_1 + \frac{1}{2}(b_i+c_i)\left(-\lambda_1-\lambda_4-\lambda_6\right)\otimes\sigma_2, \\ \delta\hat{\mathcal{H}}_{\tau_1}(\mathbf{k}=\mathbf{0}) &= \frac{1}{2}(t_1+t_2)\left(\lambda_1+\lambda_4-2\lambda_6\right)\otimes\sigma_0 + \frac{1}{2}(t_1-t_2)\left(\lambda_1+\lambda_4-2\lambda_6\right)\otimes\sigma_3, \\ \delta\hat{\mathcal{H}}_{\tau_2}(\mathbf{k}=\mathbf{0}) &= \frac{1}{2}(t_1+t_2)\left(\lambda_1-\lambda_4\right)\otimes\sigma_0 + \frac{1}{2}(t_1-t_2)\left(\lambda_1-\lambda_4\right)\otimes\sigma_3. \end{aligned} \tag{S36}$$

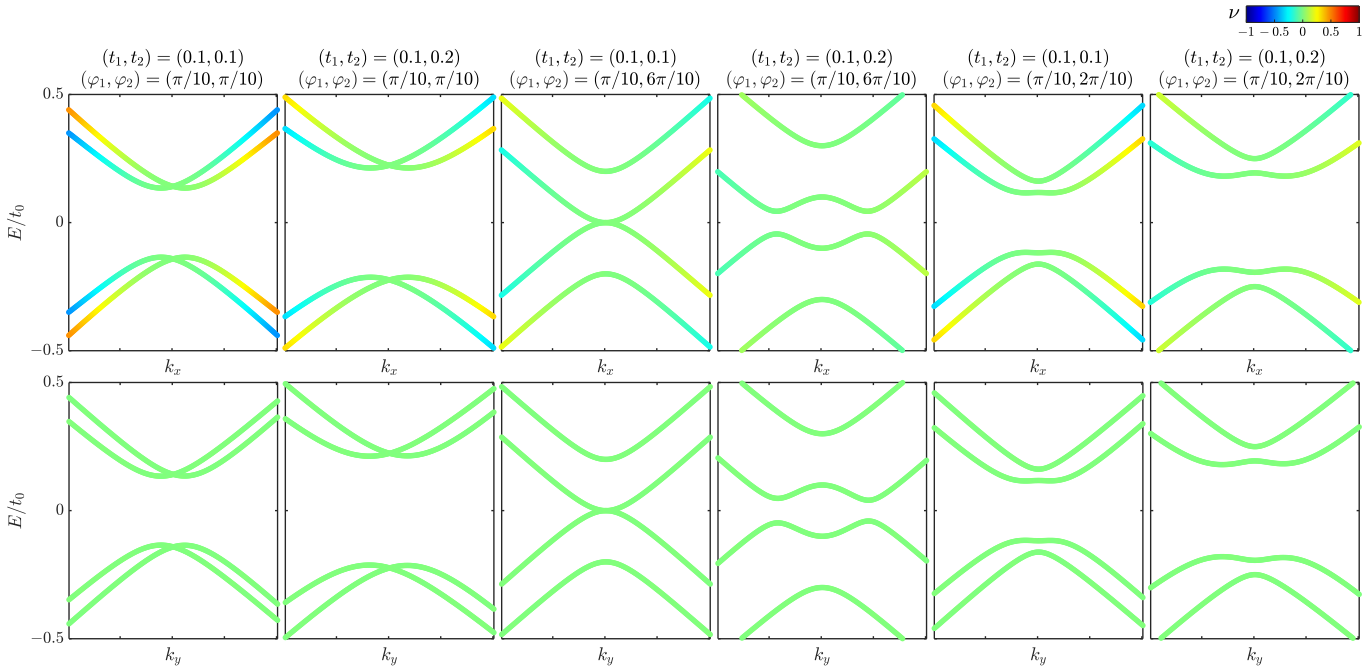

Figure S4. **Band structures for the model defined in Eq.** (S38)**.** The band structures on the top (bottom) panel are traced along the k_x (k_y) direction. We notice that Bloch states are much more strongly mixed in valley character along the k_y direction compared to the k_x direction.

In general, we can project any 6×6 Hamiltonian in the Kekule basis into the space of the valley-orbital states to obtain $\hat{\mathcal{H}}(\mathbf{k} = \mathbf{0}) = \sum_{i=0}^{3} \sum_{j=0}^{3} \mathcal{H}_{ij} \tau_i \otimes \sigma_j$, where the coefficients are given by

$$
\begin{aligned}
\mathcal{H}_{00} &= (\sqrt{6}t_{00} - t_{10} - t_{40} - t_{60})/3, \\
\mathcal{H}_{01} &= (-2t_{11} + 3t_{31} - 2t_{41} + 4t_{61} + \sqrt{3}t_{81})/6, \\
\mathcal{H}_{02} &= (-2t_{12} + 3t_{32} - 2t_{42} + 4t_{62} + \sqrt{3}t_{82})/6, \\
\mathcal{H}_{03} &= (\sqrt{6}t_{03} - t_{13} - t_{43} - t_{63})/3, \\
\mathcal{H}_{10} &= (-2t_{10} + 3t_{30} - 2t_{40} + 4t_{60} + \sqrt{3}t_{80})/6, \\
\mathcal{H}_{11} &= (\sqrt{6}t_{01} - t_{11} - t_{41} - t_{61})/3, \\
\mathcal{H}_{12} &= (\sqrt{6}t_{02} - t_{12} - t_{42} - t_{62})/3, \\
\mathcal{H}_{13} &= (-2t_{13} + 3t_{33} - 2t_{43} + 4t_{63} + \sqrt{3}t_{83})/6, \\
\mathcal{H}_{20} &= (2\sqrt{3}t_{13} + \sqrt{3}t_{33} - 2\sqrt{3}t_{43} - 3t_{83})/6, \\
\mathcal{H}_{21} &= (t_{22} - t_{52} + t_{72})/\sqrt{3}, \\
\mathcal{H}_{22} &= (-t_{21} + t_{51} - t_{71})/\sqrt{3}, \\
\mathcal{H}_{23} &= (2\sqrt{3}t_{10} + \sqrt{3}t_{30} - 2\sqrt{3}t_{40} - 3t_{80})/6, \\
\mathcal{H}_{30} &= (t_{23} - t_{53} + t_{73})/\sqrt{3}, \\
\mathcal{H}_{31} &= (-2t_{12} - t_{32} + 2t_{42} + \sqrt{3}t_{82})/2\sqrt{3}, \\
\mathcal{H}_{32} &= (2t_{11} + t_{31} - 2t_{41} - \sqrt{3}t_{81})/2\sqrt{3}, \\
\mathcal{H}_{33} &= (t_{20} - t_{50} + t_{70})/\sqrt{3}.
\end{aligned}
\tag{S37}
$$

Eq. (S37) allows us to write the Hamiltonian in the valley-orbital basis for any given Hamiltonian in the Kekule real-space basis of the form in Eq. (S34). This transformation is completely generic and generally does not respect any symmetry.

5. Band Structures for Example Models

In this section, we study the band structures of various example models in the vicinity of $\overline{\Gamma}$ of the Kekule Brillouin zone. Let us first study the example in Eq. (S19) with $a = t_1 e^{i\varphi_1}$ and $b = -c = t_2 e^{i\varphi_2}/\sqrt{3}$. With this minor relabeling, we have

$$\hat{\mathcal{H}}_{\tau_i\otimes\sigma_j}(\mathbf{k}) = \hat{\mathcal{H}}_0(\mathbf{k}) + \begin{pmatrix} 0 & t_1 e^{i\varphi_1} e^{i\mathbf{k}\cdot\boldsymbol{\delta}_1} & 0 & \frac{t_2 e^{i\varphi_2}}{\sqrt{3}} e^{i\mathbf{k}\cdot\boldsymbol{\delta}_2} & 0 & -\frac{t_2 e^{i\varphi_2}}{\sqrt{3}} e^{i\mathbf{k}\cdot\boldsymbol{\delta}_3} \\ t_1 e^{-i\varphi_1} e^{-i\mathbf{k}\cdot\boldsymbol{\delta}_1} & 0 & -\frac{t_2 e^{-i\varphi_2}}{\sqrt{3}} e^{-i\mathbf{k}\cdot\boldsymbol{\delta}_2} & 0 & \frac{t_2 e^{-i\varphi_2}}{\sqrt{3}} e^{-i\mathbf{k}\cdot\boldsymbol{\delta}_3} & 0 \\ 0 & -\frac{t_2 e^{i\varphi_2}}{\sqrt{3}} e^{i\mathbf{k}\cdot\boldsymbol{\delta}_2} & 0 & t_1 e^{i\varphi_1} e^{i\mathbf{k}\cdot\boldsymbol{\delta}_3} & 0 & \frac{t_2 e^{i\varphi_2}}{\sqrt{3}} e^{i\mathbf{k}\cdot\boldsymbol{\delta}_1} \\ \frac{t_2 e^{-i\varphi_2}}{\sqrt{3}} e^{-i\mathbf{k}\cdot\boldsymbol{\delta}_2} & 0 & t_1 e^{-i\varphi_1} e^{-i\mathbf{k}\cdot\boldsymbol{\delta}_3} & 0 & -\frac{t_2 e^{-i\varphi_2}}{\sqrt{3}} e^{-i\mathbf{k}\cdot\boldsymbol{\delta}_1} & 0 \\ 0 & \frac{t_2 e^{i\varphi_2}}{\sqrt{3}} e^{i\mathbf{k}\cdot\boldsymbol{\delta}_3} & 0 & -\frac{t_2 e^{i\varphi_2}}{\sqrt{3}} e^{i\mathbf{k}\cdot\boldsymbol{\delta}_1} & 0 & t_1 e^{i\varphi_1} e^{i\mathbf{k}\cdot\boldsymbol{\delta}_2} \\ -\frac{t_2 e^{-i\varphi_2}}{\sqrt{3}} e^{-i\mathbf{k}\cdot\boldsymbol{\delta}_3} & 0 & \frac{t_2 e^{-i\varphi_2}}{\sqrt{3}} e^{-i\mathbf{k}\cdot\boldsymbol{\delta}_1} & 0 & t_1 e^{-i\varphi_1} e^{-i\mathbf{k}\cdot\boldsymbol{\delta}_2} & 0 \end{pmatrix}. \tag{S38}$$

The energies at $\mathbf{k} = \mathbf{0}$ for the four low-energy states are given by

$$E = \pm\sqrt{t_1^2 + t_2^2 \pm 2t_1 t_2 \sin(\varphi_1 - \varphi_2)}. \tag{S39}$$

When $(\varphi_1 - \varphi_2) \mod \pi = 0$, the spectrum is degenerate with two states at $E = +\sqrt{t_1^2 + t_2^2}$ and two states at $E = -\sqrt{t_1^2 + t_2^2}$. When $(\varphi_1 - \varphi_2) \mod \pi = \pi/2$, we generically have four non-degenerate states with $E = \pm|t_1 \pm t_2|$ unless $t_1 = 0$ or $t_2 = 0$, in which case, we have two upper degenerate states and low lower degenerate states. If instead, $t_1 = \pm t_2$, then we have two degenerate states at $E = 0$. Band structures for some representative values are shown in Fig. S4. There, each state $|\psi\rangle$ is labeled by its valley polarization ν, defined as

$$\nu(\psi) = |\langle\psi|\psi_A(\mathbf{K})\rangle|^2 + |\langle\psi|\psi_B(\mathbf{K})\rangle|^2 - |\langle\psi|\psi_A(\mathbf{K}')\rangle|^2 - |\langle\psi|\psi_B(\mathbf{K}')\rangle|^2. \tag{S40}$$

This value ranges in $[-1, 1]$, with -1 indicating polarization in the K' valley and $+1$ indicating polarization in the K valley. As shown in Fig. S4, all the states are intervalley-hybridized states as diagnosed by $|\nu| < 1$. The bands are highly anisotropic along the two perpendicular directions shown. It is immediately apparent from Fig. S4 that Bloch states along the k_y direction are much more strongly mixed in valley character, i.e. $\nu \approx 0$, than states along the k_x direction. This is sensible because the k_y direction runs along the armchair direction while the k_x direction is parallel to the zigzag direction.

Next, we examine the example in Eq. (S32), which, when the momentum dependence is restored, takes the following form

$$\hat{\mathcal{H}}_{\tau_1}(\mathbf{k}) = \hat{\mathcal{H}}_0(\mathbf{k}) + \frac{1}{3}\begin{pmatrix} 0 & 0 & t_1 g^\dagger(\mathbf{k}) & 0 & t_1 g(\mathbf{k}) & 0 \\ 0 & 0 & 0 & t_2 g(\mathbf{k}) & 0 & t_2 g^\dagger(\mathbf{k}) \\ t_1 g(\mathbf{k}) & 0 & 0 & 0 & -2t_1 g^\dagger(\mathbf{k}) & 0 \\ 0 & t_2 g^\dagger(\mathbf{k}) & 0 & 0 & 0 & -2t_2 g(\mathbf{k}) \\ t_1 g^\dagger(\mathbf{k}) & 0 & -2t_1 g(\mathbf{k}) & 0 & 0 & 0 \\ 0 & t_2 g(\mathbf{k}) & 0 & -2t_2 g^\dagger(\mathbf{k}) & 0 & 0 \end{pmatrix}, \tag{S41}$$

where $g(\mathbf{k}) = e^{i\mathbf{k}\cdot\mathbf{a}_1} + e^{i\mathbf{k}\cdot\mathbf{a}_2} + e^{-i\mathbf{k}\cdot(\mathbf{a}_1+\mathbf{a}_2)}$. This model corresponds to $\tau_1 \otimes \sigma_0$ and $\tau_1 \otimes \sigma_3$. In the corresponding effective Hamiltonian in the valley-orbital basis, the energies are given by

$$E = \pm 2t_1, \pm 2t_2. \tag{S42}$$

When $|t_1| = |t_2|$, there are near-degenerate states (actually, in the Kekule basis, some of these degeneracies are broken), as shown in Fig. S5(a). For $\tau_2 \otimes \sigma_0$ and $\tau_2 \otimes \sigma_3$, we study the following Hamiltonian

$$\hat{\mathcal{H}}_{\tau_2}(\mathbf{k}) = \hat{\mathcal{H}}_0(\mathbf{k}) + \frac{1}{3}\begin{pmatrix} 0 & 0 & t_1 g^\dagger(\mathbf{k}) & 0 & -t_1 g(\mathbf{k}) & 0 \\ 0 & 0 & 0 & t_2 g(\mathbf{k}) & 0 & -t_2 g^\dagger(\mathbf{k}) \\ t_1 g(\mathbf{k}) & 0 & 0 & 0 & 0 & 0 \\ 0 & t_2 g^\dagger(\mathbf{k}) & 0 & 0 & 0 & 0 \\ -t_1 g^\dagger(\mathbf{k}) & 0 & 0 & 0 & 0 & 0 \\ 0 & -t_2 g(\mathbf{k}) & 0 & 0 & 0 & 0 \end{pmatrix}. \tag{S43}$$

The band structures are shown in Fig. S5(b).

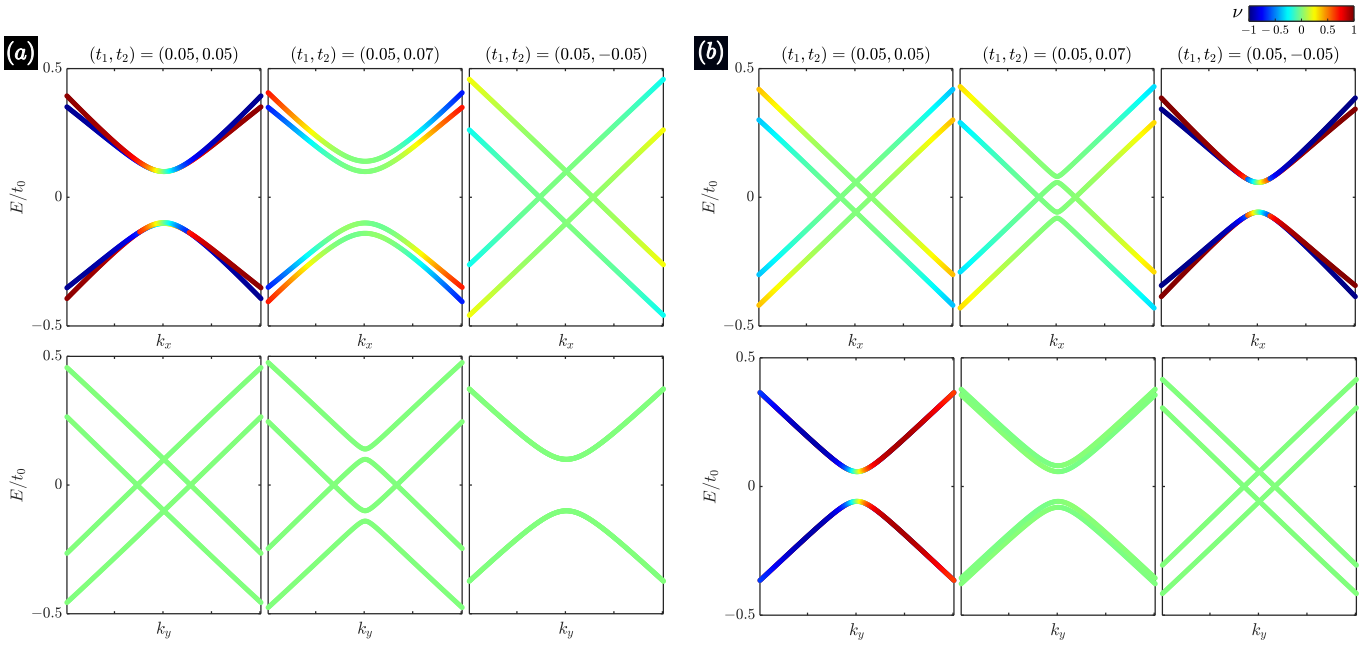

Figure S5. **Band structures for the models defined in Eqs.** (S41) **and** (S43)**.** (a) τ_1 model and (b) τ_2 model.

Finally, we consider two models that respect $C_3(\triangle)$. The first model is simply a charge modulation on the A sublattice around the Kekule unit cell:

$$\hat{\mathcal{H}}_{\tau_i\otimes(\sigma_0+\sigma_3)}(\mathbf{k}) = \hat{\mathcal{H}}_0(\mathbf{k}) + \begin{pmatrix} 0 & 0 & 0 & 0 & 0 & 0 \\ 0 & 0 & 0 & 0 & 0 & 0 \\ 0 & 0 & \varepsilon_{A_2} & 0 & 0 & 0 \\ 0 & 0 & 0 & 0 & 0 & 0 \\ 0 & 0 & 0 & 0 & \varepsilon_{A_3} & 0 \\ 0 & 0 & 0 & 0 & 0 & 0 \end{pmatrix}. \tag{S44}$$

In this model, $\varepsilon_{A_2} + \varepsilon_{A_3}$ is proportional to $\tau_1 \otimes (\sigma_0 + \sigma_3)$ while $\varepsilon_{A_2} - \varepsilon_{A_3}$ is proportional to $\tau_2 \otimes (\sigma_0 + \sigma_3)$. Some band structures are shown in Fig. S6(a). The second model requires modulation of bonds between atoms of the A sublattice

$$\hat{\mathcal{H}}_{\tau_i\otimes(\sigma_0+\sigma_3)}(\mathbf{k}) = \hat{\mathcal{H}}_0(\mathbf{k}) + \frac{1}{3}\begin{pmatrix} 0 & 0 & (-t_1 - t_2\cos\varphi)\, g^\dagger(\mathbf{k}) & 0 & t_1 g(\mathbf{k}) & 0 \\ 0 & 0 & 0 & 0 & 0 & 0 \\ (-t_1 - t_2\cos\varphi)\, g(\mathbf{k}) & 0 & 0 & 0 & t_2 e^{i\varphi} g^\dagger(\mathbf{k}) & 0 \\ 0 & 0 & 0 & 0 & 0 & 0 \\ t_1 g^\dagger(\mathbf{k}) & 0 & t_2 e^{-i\varphi} g(\mathbf{k}) & 0 & 0 & 0 \\ 0 & 0 & 0 & 0 & 0 & 0 \end{pmatrix}. \tag{S45}$$

This model allows us to tune continuously from $\tau_1 \otimes (\sigma_0 + \sigma_3)$ to $\tau_2 \otimes (\sigma_0 + \sigma_3)$ to $\tau_3 \otimes (\sigma_0 + \sigma_3)$ by varying the three available parameters. $\tau_1 \otimes (\sigma_0 + \sigma_3)$ is isolated when $\varphi = 0$ and $2t_1 + t_2 = 0$, $\tau_2 \otimes (\sigma_0 + \sigma_3)$ is isolated when $t_2 = 0$, and $\tau_3 \otimes (\sigma_0 + \sigma_3)$ is isolated when $\varphi = \pi/2$ and $t_1 = 0$. All three cases are shown in Fig. S6(b).

B. Multilayer Models

1. *General Symmetry Considerations*

To generalize our results in Sec. I A to N-layer rhombohedral graphene, we first rewrite the tight-binding Hamiltonian in the reconstructed Kekule zone. We use the same lattice structure for layer 1 as shown in Fig. S2(a). Layer 2 has exactly the same lattice structure as layer 1 but shifted by $\left(0, a/\sqrt{3}\right)$ laterally in the y-direction. In a similar way, every layer ℓ is shifted by

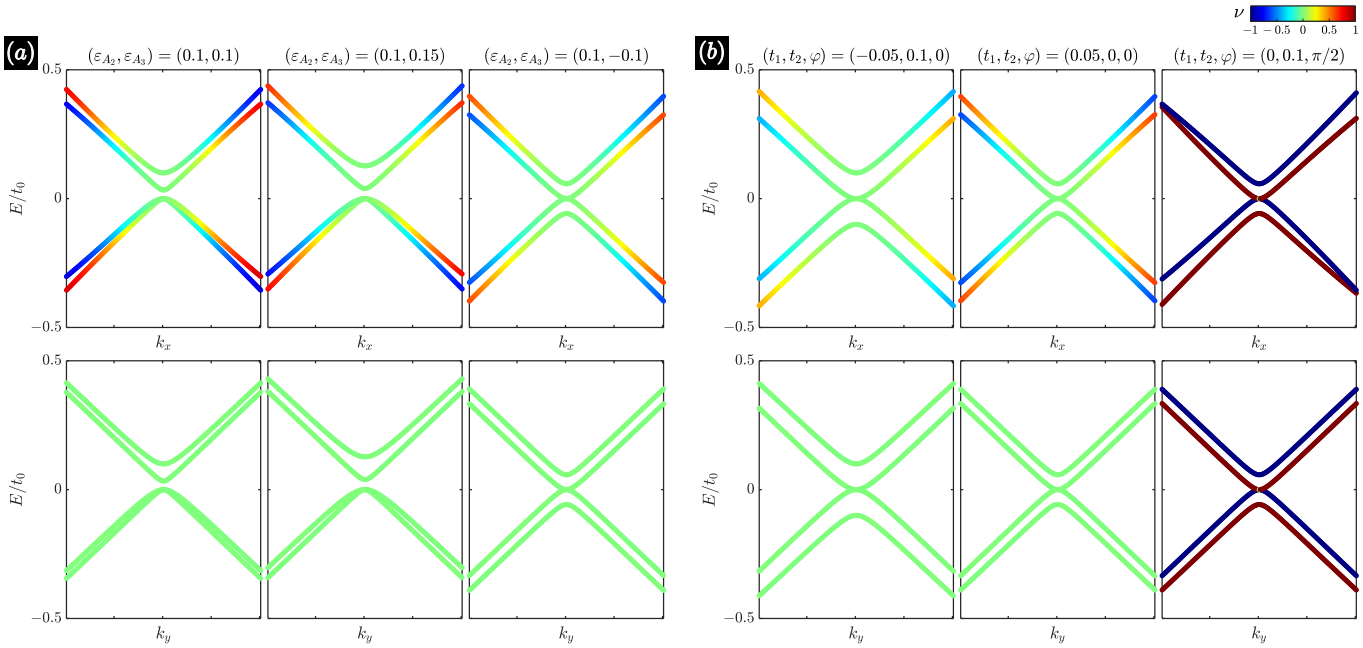

Figure S6. **Band structures for the models defined in Eqs.** (S44) **and** (S45)**.** (a) On-site model defined in Eq. (S44). (b) Hopping model defined in Eq. (S45).

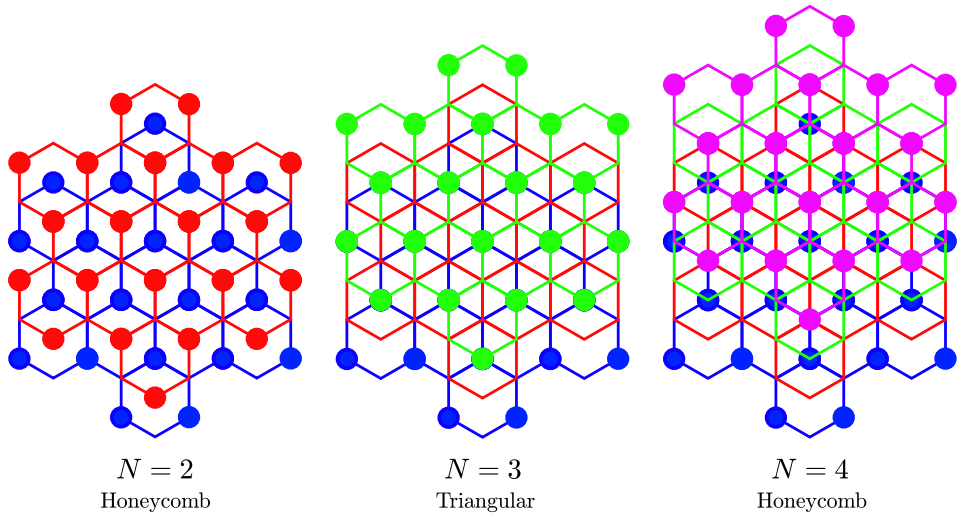

Figure S7. **Sublattice structure for rhombohedral multilayer stacks.** For N even, the structures are honeycomb, while for N odd, the structures are triangular.

$\left(0, a/\sqrt{3}\right)$ relative to layer $\ell - 1$, as shown in Fig. S7. The valley states for layer ℓ are

$$|\psi_{A^{(\ell)}}(\mathbf{K})\rangle = \frac{\mathbb{1}_\ell}{\sqrt{3}} \otimes \begin{pmatrix} 1 \\ 0 \\ \omega \\ 0 \\ \omega^\dagger \\ 0 \end{pmatrix}, \quad |\psi_{B^{(\ell)}}(\mathbf{K})\rangle = \frac{\mathbb{1}_\ell}{\sqrt{3}} \otimes \begin{pmatrix} 0 \\ 1 \\ 0 \\ \omega^\dagger \\ 0 \\ \omega \end{pmatrix} \quad |\psi_{A^{(\ell)}}(\mathbf{K}')\rangle = \frac{\mathbb{1}_\ell}{\sqrt{3}} \otimes \begin{pmatrix} 1 \\ 0 \\ \omega^\dagger \\ 0 \\ \omega \\ 0 \end{pmatrix}, \quad |\psi_{B^{(\ell)}}(\mathbf{K}')\rangle = \frac{\mathbb{1}_\ell}{\sqrt{3}} \otimes \begin{pmatrix} 0 \\ 1 \\ 0 \\ \omega \\ 0 \\ \omega^\dagger \end{pmatrix}, \tag{S46}$$

where $\mathbb{1}_\ell$ is a vector of size $N \times 1$ with one on row ℓ and zero elsewhere. The valley states on each layer are identical to each other because a shift in the y direction does not acquire any additional phase since it is orthogonal to the valley vectors $\mathbf{K}_\tau$. In the Kekule basis, the only uneclipsed sites are $A_1^{(1)}$, $A_2^{(1)}$, $A_3^{(1)}$, $B_1^{(N)}$, $B_2^{(N)}$, and $B_3^{(N)}$. Threefold rotation centered on $A_1^{(1)}$ (or

equivalently, on $A_2^{(1)}$ or on $A_3^{(1)}$) affects different layers in disparate fashions because of the relative shifts of rotation centers. On layer 1, it is implemented by the same lateral operator $\hat{C}_3(\triangle)$ as in the monolayer case. On layer 2, the rotation center is located at a hexagon center; consequently, this rotation on layer 2 is implemented by $\hat{C}_3(\hexagon)$. On layer 3, the rotation center is on the B sublattice; therefore, the action of rotation on this layer is $\hat{C}_3(\triangledown)$. On layers 4 and beyond, the rotation centers cycle through the same ordered sequence as described for layers 1-3. In total, the rotation operator for an N-layer stack about an axis going through $A_1^{(1)}$ is

$$\hat{C}_3(\triangle_N) = \begin{pmatrix} \hat{C}_3(\triangle) & 0 & 0 & 0 & \dots \\ 0 & \hat{C}_3(\hexagon) & 0 & 0 & \dots \\ 0 & 0 & \hat{C}_3(\triangledown) & 0 & \dots \\ 0 & 0 & 0 & \hat{C}_3(\triangle) & \dots \\ \vdots & \vdots & \vdots & \vdots & \ddots \end{pmatrix} \tag{S47}$$

As is well known, the low-energy physics is dominated by states localized primarily on $A^{(1)}$ and $B^{(N)}$. Projecting to just this subspace, we obtain the following representations for $C_3(\triangle_N)$ in the valley-orbital-layer basis $\{KA^{(1)}, KB^{(N)}, K'A^{(1)}, K'B^{(N)}\}$.

$$\hat{C}_3(\triangle_N) = \begin{cases} \begin{pmatrix} 1 & 0 & 0 & 0 \\ 0 & \omega & 0 & 0 \\ 0 & 0 & 1 & 0 \\ 0 & 0 & 0 & \omega^\dagger \end{pmatrix}, & \text{if} \quad \mod(N,3) = 1, \\ \begin{pmatrix} 1 & 0 & 0 & 0 \\ 0 & \omega^\dagger & 0 & 0 \\ 0 & 0 & 1 & 0 \\ 0 & 0 & 0 & \omega \end{pmatrix}, & \text{if} \quad \mod(N,3) = 2, \\ \begin{pmatrix} 1 & 0 & 0 & 0 \\ 0 & 1 & 0 & 0 \\ 0 & 0 & 1 & 0 \\ 0 & 0 & 0 & 1 \end{pmatrix}, & \text{if} \quad \mod(N,3) = 0. \end{cases} \tag{S48}$$

For $N = 4, 7, 10, ...$, the projected representation of $C_3(\Delta_N)$ looks exactly like $C_3(\triangle)$ in the monolayer case. Inspecting the $N = 4$ case in Fig. S7, we find that the effective degrees of freedom, shown by solid circles, populate the vertices of a honeycomb lattice in the exact same orientation as in the monolayer configuration. Therefore, it must be the case that the two representations of $C_3(\Delta_N)$ agree. For $N = 2, 5, 8, ...$, the projected representation of $C_3(\Delta_N)$ looks exactly like $C_3(\triangledown)$ in the monolayer case (if the two sublattices were switched). Again, referring to $N = 2$ in Fig. S7, we see that the effective degrees of freedom are located at the vertices of a honeycomb lattice but *rotated by* $180°$ relative to the monolayer lattice of Sec. I A. For $N = 3, 6, 9, ...$, $\hat{C}_3(\triangle_N)$ is the identity because the effective lattice is triangular, not honeycomb, as shown for $N = 3$ in Fig. S7.

Spinless time-reversal symmetry is a completely local operation. So, it does not couple to the sublattice or layer degrees of freedom; it simply takes every state at K to the corresponding state at K'. Therefore, its representation in the multilayer generalization remains the same as before

$$\hat{\mathcal{T}} = \tau_1 \mathcal{K}. \tag{S49}$$

With these considerations, we can classify all possible perturbations at the reconstructed $\overline{\Gamma}$ point of rhombohedral N-layer graphene that are invariant under $\hat{C}_3(\triangle_N)$ and $\hat{\mathcal{T}}$, as listed in Table SII. For $\mod(N,3) = 1$ or 2, the allowed terms are the same as those found before in the monolayer case. Interestingly, for $\mod(N,3) = 0$, all 15 nontrivial coupling terms $\tau_i \otimes \sigma_j$ are possible because of the trivial action of $C_3(\triangle_N)$ on this projected basis, i.e. it is the identity. In particular, in this setting, it is possible to have $\mathcal{T}$-breaking terms that mix valleys: $\tau_1 \otimes \sigma_2$ and $\tau_2 \otimes \sigma_2$. These terms must necessarily have sublattice coherence, which *might* be difficult to achieve because the top and bottom layers can be far apart. We postpone the consideration of these terms to later analysis. In this section, we focus on the layer-projected $\tau_1 \otimes (\sigma_0 + \sigma_3)$, $\tau_2 \otimes (\sigma_0 + \sigma_3)$, and $\tau_3 \otimes (\sigma_0 + \sigma_3)$, which are consistent with $C_3(\Delta_N)$ symmetry regardless of the number of layers.

$\mathrm{mod}\ (N,3)=0$	$\mathcal{T}$ even	$\mathcal{T}$ odd
Intravalley	$\sigma_3, \sigma_1, \tau_3\otimes\sigma_2$	$\sigma_2, \tau_3, \tau_3\otimes\sigma_3, \tau_3\otimes\sigma_1$
Intervalley	$\tau_1, \tau_2, \tau_1\otimes\sigma_1, \tau_1\otimes\sigma_3, \tau_2\otimes\sigma_1, \tau_2\otimes\sigma_3$	$\tau_1\otimes\sigma_2, \tau_2\otimes\sigma_2$
$\mathrm{mod}\ (N,3)=1$ or 2	$\mathcal{T}$ even	$\mathcal{T}$ odd
Intravalley	σ_3	$\tau_3, \tau_3\otimes\sigma_3$
Intervalley	$\tau_1\otimes(\sigma_0+\sigma_3), \tau_2\otimes(\sigma_0+\sigma_3)$	none

Table SII. **Symmetry classification of operators in valley-orbital space for rhombohedral N-layer graphene at the $\overline{\Gamma}$ point in the reconstructed Kekule lattice.** $\mathcal{T}$ is spinless time-reversal symmetry.

2. *Full N-Layer Models in the Kekule Basis*

The full Hamiltonian is built from sub-Hamiltonians in the following way

$$\hat{\mathcal{H}}(\mathbf{k}) = \begin{pmatrix} \hat{\mathcal{K}}(\mathbf{k}) & \hat{\mathcal{U}}_1(\mathbf{k}) & \hat{\mathcal{U}}_2 & 0 & \dots & 0 \\ \hat{\mathcal{U}}_1^\dagger(\mathbf{k}) & \hat{\mathcal{K}}(\mathbf{k}) & \hat{\mathcal{U}}_1(\mathbf{k}) & \hat{\mathcal{U}}_2 & \dots & 0 \\ \hat{\mathcal{U}}_2^\dagger & \hat{\mathcal{U}}_1^\dagger(\mathbf{k}) & \hat{\mathcal{K}}(\mathbf{k}) & \hat{\mathcal{U}}_1(\mathbf{k}) & \dots & 0 \\ 0 & \hat{\mathcal{U}}_2^\dagger & \hat{\mathcal{U}}_1^\dagger(\mathbf{k}) & \hat{\mathcal{K}}(\mathbf{k}) & \dots & 0 \\ \vdots & \vdots & \vdots & \vdots & \ddots & \vdots \\ 0 & 0 & 0 & 0 & \dots & \hat{\mathcal{K}}(\mathbf{k}) \end{pmatrix} + \Delta \begin{pmatrix} \frac{N-1}{2} & 0 & 0 & 0 & \dots & 0 \\ 0 & \frac{N-3}{2} & 0 & 0 & \dots & 0 \\ 0 & 0 & \frac{N-5}{2} & 0 & \dots & 0 \\ 0 & 0 & 0 & \frac{N-7}{2} & \dots & 0 \\ \vdots & \vdots & \vdots & \vdots & \ddots & \vdots \\ 0 & 0 & 0 & 0 & \dots & -\frac{N-1}{2} \end{pmatrix}, \tag{S50}$$

where $\hat{\mathcal{K}}(\mathbf{k})$ is the in-plane kinetic energy, which is identical to $\hat{\mathcal{H}}_0$ given in Eq. (S14) and repeated here for convenience,

$$\hat{\mathcal{K}}(\mathbf{k}) = -\gamma_0 \begin{pmatrix} 0 & e^{i\mathbf{k}\cdot\boldsymbol{\delta}_1} & 0 & e^{i\mathbf{k}\cdot\boldsymbol{\delta}_2} & 0 & e^{i\mathbf{k}\cdot\boldsymbol{\delta}_3} \\ e^{-i\mathbf{k}\cdot\boldsymbol{\delta}_1} & 0 & e^{-i\mathbf{k}\cdot\boldsymbol{\delta}_2} & 0 & e^{-i\mathbf{k}\cdot\boldsymbol{\delta}_3} & 0 \\ 0 & e^{i\mathbf{k}\cdot\boldsymbol{\delta}_2} & 0 & e^{i\mathbf{k}\cdot\boldsymbol{\delta}_3} & 0 & e^{i\mathbf{k}\cdot\boldsymbol{\delta}_1} \\ e^{-i\mathbf{k}\cdot\boldsymbol{\delta}_2} & 0 & e^{-i\mathbf{k}\cdot\boldsymbol{\delta}_3} & 0 & e^{-i\mathbf{k}\cdot\boldsymbol{\delta}_1} & 0 \\ 0 & e^{i\mathbf{k}\cdot\boldsymbol{\delta}_3} & 0 & e^{i\mathbf{k}\cdot\boldsymbol{\delta}_1} & 0 & e^{i\mathbf{k}\cdot\boldsymbol{\delta}_2} \\ e^{-i\mathbf{k}\cdot\boldsymbol{\delta}_3} & 0 & e^{-i\mathbf{k}\cdot\boldsymbol{\delta}_1} & 0 & e^{-i\mathbf{k}\cdot\boldsymbol{\delta}_2} & 0 \end{pmatrix}, \tag{S51}$$

$\hat{\mathcal{U}}_1$ is the interlayer hopping matrix between adjacent layers,

$$\hat{\mathcal{U}}_1(\mathbf{k}) = \begin{pmatrix} -\gamma_4 e^{i\mathbf{k}\cdot\boldsymbol{\delta}_1} & -\gamma_3 e^{-i\mathbf{k}\cdot\boldsymbol{\delta}_1} & -\gamma_4 e^{i\mathbf{k}\cdot\boldsymbol{\delta}_3} & -\gamma_3 e^{-i\mathbf{k}\cdot\boldsymbol{\delta}_3} & -\gamma_4 e^{i\mathbf{k}\cdot\boldsymbol{\delta}_2} & -\gamma_3 e^{-i\mathbf{k}\cdot\boldsymbol{\delta}_2} \\ \gamma_1 & -\gamma_4 e^{i\mathbf{k}\cdot\boldsymbol{\delta}_1} & 0 & -\gamma_4 e^{i\mathbf{k}\cdot\boldsymbol{\delta}_2} & 0 & -\gamma_4 e^{i\mathbf{k}\cdot\boldsymbol{\delta}_3} \\ -\gamma_4 e^{i\mathbf{k}\cdot\boldsymbol{\delta}_2} & -\gamma_3 e^{-i\mathbf{k}\cdot\boldsymbol{\delta}_3} & -\gamma_4 e^{i\mathbf{k}\cdot\boldsymbol{\delta}_1} & -\gamma_3 e^{-i\mathbf{k}\cdot\boldsymbol{\delta}_2} & -\gamma_4 e^{i\mathbf{k}\cdot\boldsymbol{\delta}_3} & -\gamma_3 e^{-i\mathbf{k}\cdot\boldsymbol{\delta}_1} \\ 0 & -\gamma_4 e^{i\mathbf{k}\cdot\boldsymbol{\delta}_3} & 0 & -\gamma_4 e^{i\mathbf{k}\cdot\boldsymbol{\delta}_1} & \gamma_1 & -\gamma_4 e^{i\mathbf{k}\cdot\boldsymbol{\delta}_2} \\ -\gamma_4 e^{i\mathbf{k}\cdot\boldsymbol{\delta}_3} & -\gamma_3 e^{-i\mathbf{k}\cdot\boldsymbol{\delta}_2} & -\gamma_4 e^{i\mathbf{k}\cdot\boldsymbol{\delta}_2} & -\gamma_3 e^{-i\mathbf{k}\cdot\boldsymbol{\delta}_1} & -\gamma_4 e^{i\mathbf{k}\cdot\boldsymbol{\delta}_1} & -\gamma_3 e^{-i\mathbf{k}\cdot\boldsymbol{\delta}_3} \\ 0 & -\gamma_4 e^{i\mathbf{k}\cdot\boldsymbol{\delta}_2} & \gamma_1 & -\gamma_4 e^{i\mathbf{k}\cdot\boldsymbol{\delta}_3} & 0 & -\gamma_4 e^{i\mathbf{k}\cdot\boldsymbol{\delta}_1} \end{pmatrix}, \tag{S52}$$

and $\hat{\mathcal{U}}_2$ is the interlayer hopping matrix between layers that are separated by another in the middle,

$$\hat{\mathcal{U}}_2 = \begin{pmatrix} 0 & \gamma_2/2 & 0 & 0 & 0 & 0 \\ 0 & 0 & 0 & 0 & 0 & 0 \\ 0 & 0 & 0 & 0 & 0 & \gamma_2/2 \\ 0 & 0 & 0 & 0 & 0 & 0 \\ 0 & 0 & 0 & \gamma_2/2 & 0 & 0 \\ 0 & 0 & 0 & 0 & 0 & 0 \end{pmatrix}. \tag{S53}$$

Here, Δ is the field-induced layer potential energy and γ_i are the hopping parameters. We ignore various on-site energies due to dimerization since they do not qualitatively matter when the displacement field is reasonably large. To demonstrate that this

γ_0	γ_1	γ_2	γ_3	γ_4
3100	380	-15	-290	-141

Table SIII. **Tight-binding parameters**. All values are quoted in meV.

Hamiltonian respects $C_3(\triangle_N)$, we have verified the following identity

$$\begin{pmatrix} \hat{C}_3(\triangle)^\dagger & 0 & 0 & 0 & \dots \\ 0 & \hat{C}_3(\hexagon)^\dagger & 0 & 0 & \dots \\ 0 & 0 & \hat{C}_3(\triangledown)^\dagger & 0 & \dots \\ 0 & 0 & 0 & \hat{C}_3(\triangle)^\dagger & \dots \\ \vdots & \vdots & \vdots & \vdots & \ddots \end{pmatrix} \begin{pmatrix} \hat{\mathcal{K}}(\mathbf{k}) & \hat{\mathcal{U}}_1(\mathbf{k}) & \hat{\mathcal{U}}_2 & 0 & \dots \\ \hat{\mathcal{U}}_1^\dagger(\mathbf{k}) & \hat{\mathcal{K}}(\mathbf{k}) & \hat{\mathcal{U}}_1(\mathbf{k}) & \hat{\mathcal{U}}_2 & \dots \\ \hat{\mathcal{U}}_2^\dagger & \hat{\mathcal{U}}_1^\dagger(\mathbf{k}) & \hat{\mathcal{K}}(\mathbf{k}) & \hat{\mathcal{U}}_1(\mathbf{k}) & \dots \\ 0 & \hat{\mathcal{U}}_2^\dagger & \hat{\mathcal{U}}_1^\dagger(\mathbf{k}) & \hat{\mathcal{K}}(\mathbf{k}) & \dots \\ \vdots & \vdots & \vdots & \vdots & \ddots \end{pmatrix} \begin{pmatrix} \hat{C}_3(\triangle) & 0 & 0 & 0 & \dots \\ 0 & \hat{C}_3(\hexagon) & 0 & 0 & \dots \\ 0 & 0 & \hat{C}_3(\triangledown) & 0 & \dots \\ 0 & 0 & 0 & \hat{C}_3(\triangle) & \dots \\ \vdots & \vdots & \vdots & \vdots & \ddots \end{pmatrix}$$

$$= \begin{pmatrix} \hat{C}_3(\triangle)^\dagger\hat{\mathcal{K}}(\mathbf{k})\hat{C}_3(\triangle) & \hat{C}_3(\triangle)^\dagger\hat{\mathcal{U}}_1(\mathbf{k})\hat{C}_3(\hexagon) & \hat{C}_3(\triangle)^\dagger\hat{\mathcal{U}}_2\hat{C}_3(\triangledown) & 0 & \dots \\ \hat{C}_3(\hexagon)^\dagger\hat{\mathcal{U}}_1^\dagger(\mathbf{k})\hat{C}_3(\triangle) & \hat{C}_3(\hexagon)^\dagger\hat{\mathcal{K}}(\mathbf{k})\hat{C}_3(\hexagon) & \hat{C}_3(\hexagon)^\dagger\hat{\mathcal{U}}_1(\mathbf{k})\hat{C}_3(\triangledown) & \hat{C}_3(\hexagon)^\dagger\hat{\mathcal{U}}_2\hat{C}_3(\triangle) & \dots \\ \hat{C}_3(\triangledown)^\dagger\hat{\mathcal{U}}_2^\dagger\hat{C}_3(\triangle) & \hat{C}_3(\triangledown)^\dagger\hat{\mathcal{U}}_1^\dagger(\mathbf{k})\hat{C}_3(\hexagon) & \hat{C}_3(\triangledown)^\dagger\hat{\mathcal{K}}(\mathbf{k})\hat{C}_3(\triangledown) & \hat{C}_3(\triangledown)^\dagger\hat{\mathcal{U}}_1(\mathbf{k})\hat{C}_3(\triangle) & \dots \\ 0 & \hat{C}_3(\triangle)^\dagger\hat{\mathcal{U}}_2^\dagger\hat{C}_3(\hexagon) & \hat{C}_3(\triangle)^\dagger\hat{\mathcal{U}}_1^\dagger(\mathbf{k})\hat{C}_3(\triangledown) & \hat{C}_3(\triangle)^\dagger\hat{\mathcal{K}}(\mathbf{k})\hat{C}_3(\triangle) & \dots \\ \vdots & \vdots & \vdots & \vdots & \ddots \end{pmatrix}$$

$$= \begin{pmatrix} \hat{\mathcal{K}}(R_3\mathbf{k}) & \hat{\mathcal{U}}_1(R_3\mathbf{k}) & \hat{\mathcal{U}}_2 & 0 & \dots \\ \hat{\mathcal{U}}_1^\dagger(R_3\mathbf{k}) & \hat{\mathcal{K}}(R_3\mathbf{k}) & \hat{\mathcal{U}}_1(R_3\mathbf{k}) & \hat{\mathcal{U}}_2 & \dots \\ \hat{\mathcal{U}}_2^\dagger & \hat{\mathcal{U}}_1^\dagger(R_3\mathbf{k}) & \hat{\mathcal{K}}(R_3\mathbf{k}) & \hat{\mathcal{U}}_1(R_3\mathbf{k}) & \dots \\ 0 & \hat{\mathcal{U}}_2^\dagger & \hat{\mathcal{U}}_1^\dagger(R_3\mathbf{k}) & \hat{\mathcal{K}}(R_3\mathbf{k}) & \dots \\ \vdots & \vdots & \vdots & \vdots & \ddots \end{pmatrix}, \tag{S54}$$

which simplifies to confirming the following equalities:

$$\begin{aligned} &\hat{C}_3(\triangle)^\dagger\hat{\mathcal{K}}(\mathbf{k})\hat{C}_3(\triangle) = \hat{\mathcal{K}}(R_3\mathbf{k}), \quad \hat{C}_3(\hexagon)^\dagger\hat{\mathcal{K}}(\mathbf{k})\hat{C}_3(\hexagon) = \hat{\mathcal{K}}(R_3\mathbf{k}), \quad \hat{C}_3(\triangledown)^\dagger\hat{\mathcal{K}}(\mathbf{k})\hat{C}_3(\triangledown) = \hat{\mathcal{K}}(R_3\mathbf{k}), \\ &\hat{C}_3(\triangle)^\dagger\hat{\mathcal{U}}_1(\mathbf{k})\hat{C}_3(\hexagon) = \hat{\mathcal{U}}_1(R_3\mathbf{k}), \quad \hat{C}_3(\hexagon)^\dagger\hat{\mathcal{U}}_1(\mathbf{k})\hat{C}_3(\triangledown) = \hat{\mathcal{U}}_1(R_3\mathbf{k}), \quad \hat{C}_3(\triangledown)^\dagger\hat{\mathcal{U}}_1(\mathbf{k})\hat{C}_3(\triangle) = \hat{\mathcal{U}}_1(R_3\mathbf{k}), \\ &\hat{C}_3(\triangle)^\dagger\hat{\mathcal{U}}_2\hat{C}_3(\triangledown) = \hat{\mathcal{U}}_2, \quad \hat{C}_3(\hexagon)^\dagger\hat{\mathcal{U}}_2\hat{C}_3(\triangle) = \hat{\mathcal{U}}_2, \quad \hat{C}_3(\triangledown)^\dagger\hat{\mathcal{U}}_2\hat{C}_3(\hexagon) = \hat{\mathcal{U}}_2, \end{aligned} \tag{S55}$$

where R_3 rotates wavevectors $\mathbf{k}$ by $2\pi/3 : R_3(k_x, k_y) = (-k_x + \sqrt{3}k_y, -\sqrt{3}k_x - k_y)/2$. In the Kekule basis, the three different symmetry operators are given elsewhere already but are repeated here for convenience:

$$\hat{C}_3(\hexagon) = \begin{pmatrix} 0 & 0 & 1 & 0 & 0 & 0 \\ 0 & 0 & 0 & 1 & 0 & 0 \\ 0 & 0 & 0 & 0 & 1 & 0 \\ 0 & 0 & 0 & 0 & 0 & 1 \\ 1 & 0 & 0 & 0 & 0 & 0 \\ 0 & 1 & 0 & 0 & 0 & 0 \end{pmatrix}, \quad \hat{C}_3(\triangle) = \begin{pmatrix} 1 & 0 & 0 & 0 & 0 & 0 \\ 0 & 0 & 0 & 0 & 0 & 1 \\ 0 & 0 & 1 & 0 & 0 & 0 \\ 0 & 1 & 0 & 0 & 0 & 0 \\ 0 & 0 & 0 & 0 & 1 & 0 \\ 0 & 0 & 0 & 1 & 0 & 0 \end{pmatrix}, \quad \hat{C}_3(\triangledown) = \begin{pmatrix} 0 & 0 & 0 & 0 & 1 & 0 \\ 0 & 1 & 0 & 0 & 0 & 0 \\ 1 & 0 & 0 & 0 & 0 & 0 \\ 0 & 0 & 0 & 1 & 0 & 0 \\ 0 & 0 & 1 & 0 & 0 & 0 \\ 0 & 0 & 0 & 0 & 0 & 1 \end{pmatrix}. \tag{S56}$$

Since the displacement field matrix acts uniformly and locally on each layer, it must commute with the $C_3(\Delta_N)$ symmetry operator. We have therefore checked that the full Hamiltonian is invariant under C_3 rotation about $A_1^{(1)}$.

3. Band Structures for Realistic Systems

In this section, we study the band structures of realistic models of N-layer rhombohedral graphene. We first examine the single-valley Fermi topology without any perturbation. We use the parameters listed in Table SIII for all of our simulations. Using the non-interacting band structures using Eq. (S50), we compute the density of states (DOS) as a function of electron density in a single valley-spin flavor (because we are ultimately interested only in the quarter metal phase) and displacement field using the formula

$$\mathrm{DOS}(E_F) = \frac{1}{\pi}\sum_n \frac{\eta}{\eta^2 + (E_F - E_n)^2}, \tag{S57}$$

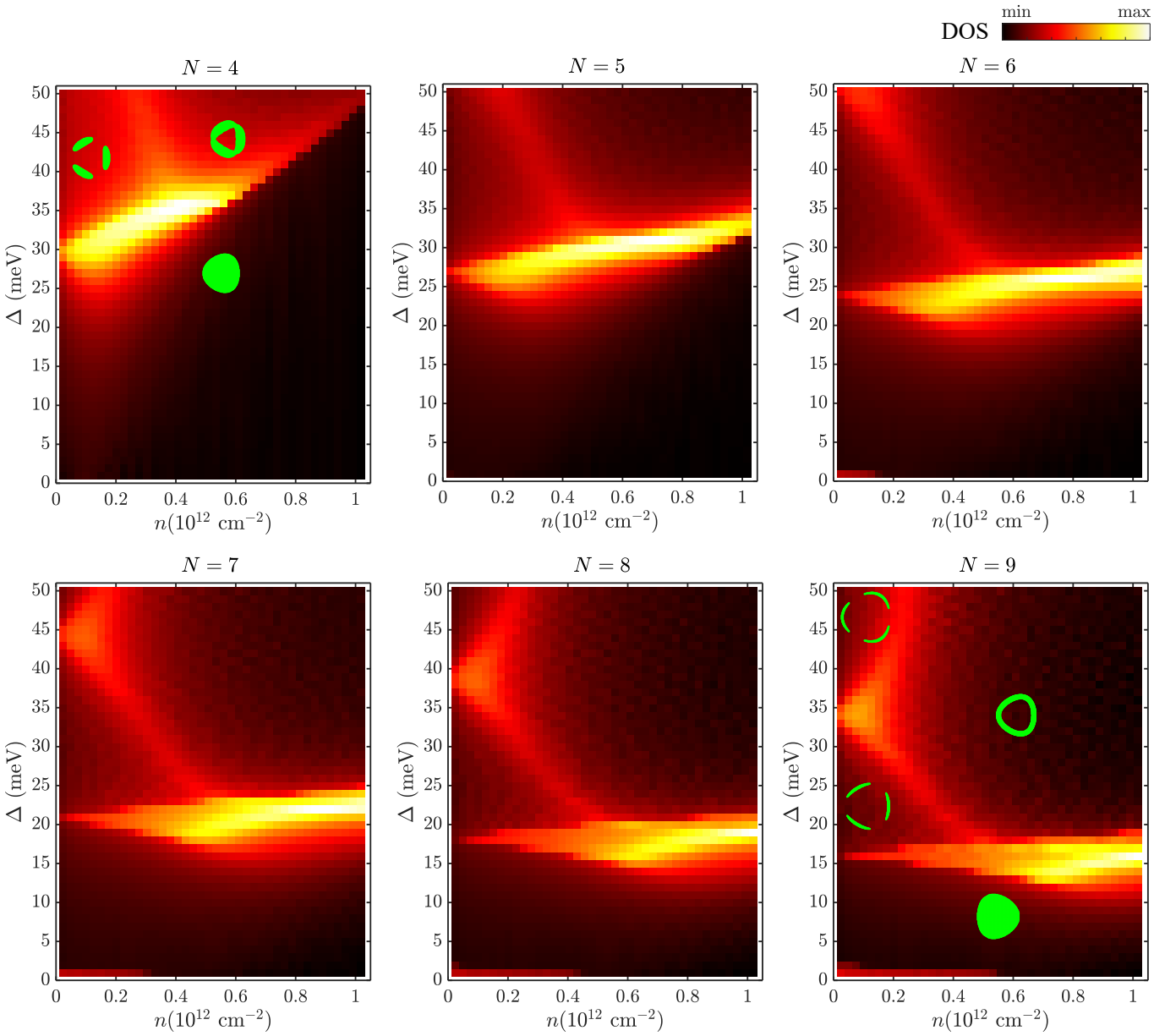

Figure S8. **Density-of-states maps as a function of electron density (in a single valley-spin) and displacement field.** High-intensity bright regions correspond to Lifshitz transitions where Fermi surface topologies change. Representative Fermi surfaces are shown for $N = 4$ and $N = 9$, with the other layer numbers displaying similar trends.

where $\eta = 0.1$ meV is a numerical broadening factor, E_F is the Fermi energy determined by the charge density, and E_n are the energy eigenvalues. The results for $N = 4, 5, 6, 7, 8, 9$ are shown in Fig. S8. The DOS maps contain a few prominent peaks associated with diverging DOS due to Lifshitz transitions for all values of N shown. At small values of Δ, the Fermi surface is primarily that of a simply-connected trigonally-warped geometry for the values of electron density shown across the different numbers of layers. As the displacement field increases, that simply-connected geometry evolves into one of two distinct Fermi surface topologies: a three-pocket structure at small densities or an annular surface at larger densities. The critical fields where these Liftshitz transitions occur are inversely related to increasing layer number. In between these Lifshitz transitions, there are many more topologically distinct Fermi surface topologies, such as a four-pocket structure, but they require fine-tuning parameters that we do not consider further. For our purpose, we will only consider the three Fermi surface topologies mentioned, although the primary focus is on the simply-connected topology.

Next, we add intervalley imbalance and hybridization. We implement intervalley imbalance on the $A^{(1)}$ sublattice to which we assume most of the charge density has been driven by the interlayer displacement field. For intervalley imbalance, we use a

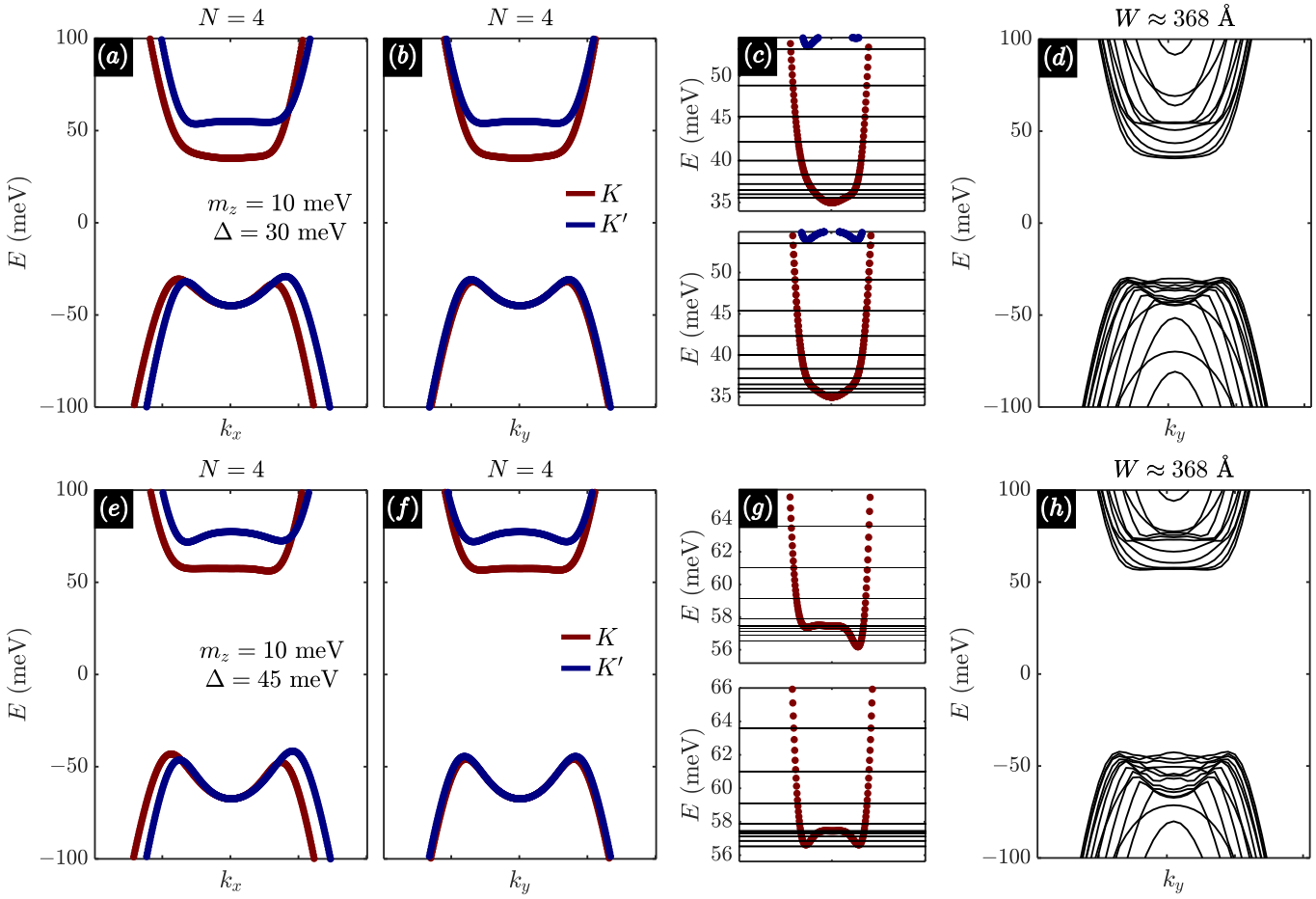

Figure S9. **Band structures for $N = 4$ with intervalley imbalance.** (a,b) Band structures along k_x and k_y for $m_z = 10$ meV and $\Delta = 30$ meV. (c) we zoom in on the bottoms of the conduction bands using black horizontal lines to show the chemical potentials at $n = 0.1, 0.2, ..., 0.8, 0.9, 1.0 \times 10^{12}$ cm^{-2}. (d) Band structure of an armchair nanoribbon with width $W = 368$ Å. (a-d) The top panel shows band structures at $\Delta = 30$ meV, while (e-h) the bottom panel shows band structures at $\Delta = 45$ meV.

version of the Haldane model, which in the Kekule basis, takes the following form on layer 1:

$$\delta\hat{\mathcal{H}}_{\tau_3}(\mathbf{k}) = \frac{m_z}{3\sqrt{3}i}\begin{pmatrix} 0 & 0 & -g^\dagger(\mathbf{k}) & 0 & g(\mathbf{k}) & 0 \\ 0 & 0 & 0 & 0 & 0 & 0 \\ g(\mathbf{k}) & 0 & 0 & 0 & -g^\dagger(\mathbf{k}) & 0 \\ 0 & 0 & 0 & 0 & 0 & 0 \\ -g^\dagger(\mathbf{k}) & 0 & g(\mathbf{k}) & 0 & 0 & 0 \\ 0 & 0 & 0 & 0 & 0 & 0 \end{pmatrix}, \tag{S58}$$

where $g(\mathbf{k}) = \sum_{i=1}^{3} e^{i\mathbf{k}\cdot\mathbf{a}_i}$ as defined before. At the $\bar{\Gamma}$ point, this Hamiltonian generates an intervalley imbalance with magnitude $-m_z\tau_3 \otimes (\sigma_0 - \sigma_3)/2$. In the valley-sublattice basis, the Hamiltonian takes the following minimal form

$$\delta\hat{\mathcal{H}}_{\tau_3}(\mathbf{0}) = \begin{pmatrix} \Delta\frac{N-1}{2} - m_z & 0 & 0 & 0 \\ 0 & -\Delta\frac{N-1}{2} & 0 & 0 \\ 0 & 0 & \Delta\frac{N-1}{2} + m_z & 0 \\ 0 & 0 & 0 & -\Delta\frac{N-1}{2} \end{pmatrix}. \tag{S59}$$

To a first approximation, the valence bands are not affected by this perturbation, while the conduction bands are valley-split by an energy amount of $2m_z$ at $\mathbf{k} = \mathbf{0}$. The situation away from $\bar{\Gamma}$ is much more complicated because the two valleys experience different effective mass terms, which as we have shown earlier, can deform the bands in various different ways to give distinct Fermi surface topologies. To ensure that we are always in the quarter metal phase, m_z needs to be large enough so that the chemical potential lies entirely in a single valley. Using Fig. S8 as a guide, we now inspect some specific combinations of Δ and

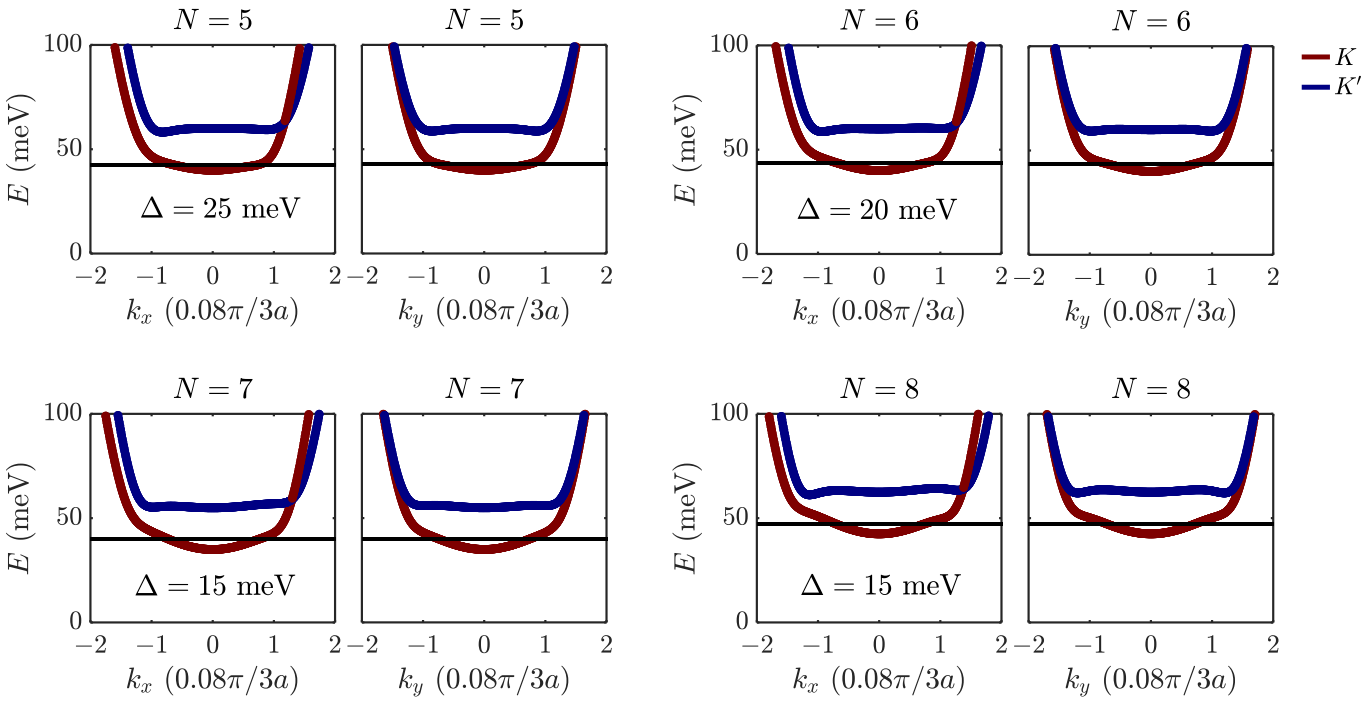

Figure S10. **Band structures for $N = 5-8$ with intervalley imbalance.** For each N, we show the band structure along k_x and k_y. The black horizontal lines indicate the chemical potentials at $n = 5 \times 10^{11}$ cm^{-2}. In all cases, $m_z = 10$ meV. Here, there is no intervalley interaction.

m_z to ensure that within the range of density of interest, the Fermi surface lies entirely in a single valley. In Fig. S9, we show the band structures for $N = 4$ using $m_z = 10$ meV showing that this is enough to keep both valleys separated in the range density $n \in [0, 1.0] \times 10^{12}$ cm^{-2}. In Fig. S10, we generalize this to $N = 5 - 8$, showing that $m_z = 10$ meV is enough to keep the conduction electrons in only one valley for $n = 5 \times 10^{11}$ cm^{-2}.

Finally, we implement τ_1 and τ_2 with the following

$$\delta\hat{\mathcal{H}}_{\tau_1}(\mathbf{k}) = m\cos\theta \begin{pmatrix} 0 & 0 & -\frac{1}{2}g^\dagger(\mathbf{k}) & 0 & -\frac{1}{2}g(\mathbf{k}) & 0 \\ 0 & 0 & 0 & 0 & 0 & 0 \\ -\frac{1}{2}g(\mathbf{k}) & 0 & 0 & 0 & g^\dagger(\mathbf{k}) & 0 \\ 0 & 0 & 0 & 0 & 0 & 0 \\ -\frac{1}{2}g^\dagger(\mathbf{k}) & 0 & g(\mathbf{k}) & 0 & 0 & 0 \\ 0 & 0 & 0 & 0 & 0 & 0 \end{pmatrix},$$
$$\delta\hat{\mathcal{H}}_{\tau_2}(\mathbf{k}) = m\sin\theta \begin{pmatrix} 0 & 0 & \frac{\sqrt{3}}{2}g^\dagger(\mathbf{k}) & 0 & -\frac{\sqrt{3}}{2}g(\mathbf{k}) & 0 \\ 0 & 0 & 0 & 0 & 0 & 0 \\ \frac{\sqrt{3}}{2}g(\mathbf{k}) & 0 & 0 & 0 & 0 & 0 \\ 0 & 0 & 0 & 0 & 0 & 0 \\ -\frac{\sqrt{3}}{2}g^\dagger(\mathbf{k}) & 0 & 0 & 0 & 0 & 0 \\ 0 & 0 & 0 & 0 & 0 & 0 \end{pmatrix}, \tag{S60}$$

where m is the magnitude of the perturbation and θ rotates the τ matrices.

II. TRANSPORT ALONG AND ACROSS DOMAIN WALLS

A. Reflections at an Armchair Termination

1. *Continuum Description*

We consider the continuum description of an armchair termination for monolayer graphene where the bulk extends to the negative x direction. This calculation will naturally extend to the domain-wall scenario that we will show later. In the bulk, the

continuum Hamiltonian is

$$\hat{\mathcal{H}}_{\text{eff}}(\mathbf{k}) = \begin{pmatrix} \hat{\mathcal{H}}_K(\mathbf{k}) & 0 \\ 0 & \hat{\mathcal{H}}_{K'}(\mathbf{k}) \end{pmatrix} = \begin{pmatrix} \varepsilon_K & \hbar v_0 (k_x - i k_y) & 0 & 0 \\ \hbar v_0 (k_x + i k_y) & -\varepsilon_K & 0 & 0 \\ 0 & 0 & \varepsilon_{K'} & \hbar v_0 (-k_x - i k_y) \\ 0 & 0 & \hbar v_0 (-k_x + i k_y) & -\varepsilon_{K'} \end{pmatrix}. \tag{S61}$$

In real space, we implement the replacement $k_i = -i\partial_i$. We place the armchair edge at $\mathbf{r} = (0, y)$ and impose the boundary condition $\psi_K(0, y) = \psi_{K'}(0, y)$. By mapping $k_x \mapsto -k_x$ in the K' sector, we can map the two-valley wavefunction in the half-plane to a one-valley wavefunction in the entire plane where the boundary condition connecting the two valleys in the former representation is converted to a continuity requirement of the one-valley wavefunction at the origin in the latter representation. Because of translational symmetry along the y direction, k_y remains a good quantum number. For concreteness, let us assume $0 < \varepsilon_K \leq \varepsilon_{K'}$. This non-essential assumption follows from the more general assumption that the large displacement-field-induced gap is topologically trivial. We use it here only so that we do not have to look for topological edge states. With these simplifications, eigenvalue problem in real space becomes a pair of coupled differential equations

$$\begin{pmatrix} \varepsilon(x) & \hbar v_0 (-i\partial_x - i k_y) \\ \hbar v_0 (-i\partial_x + i k_y) & -\varepsilon(x) \end{pmatrix} \begin{pmatrix} \psi_A(x) \\ \psi_B(x) \end{pmatrix} = E \begin{pmatrix} \psi_A(x) \\ \psi_B(x) \end{pmatrix}, \tag{S62}$$

where $\varepsilon(x \leq 0) = \varepsilon_K$ and $\varepsilon(x > 0) = \varepsilon_{K'}$. We have converted the problem of an armchair boundary into a *scattering* problem where an incoming wave from valley K is either reflected or transmitted. Reflection in the recast problem corresponds to *valley-preserving* reflection (a K state is reflected to a K state) in the original formalism while transmission in the recast problem corresponds to *valley-exchanging* reflection (a K state is reflected to a K' state) in the original formalism.

To begin, let us consider the familiar problem where $\varepsilon_K = \varepsilon_{K'} = \varepsilon$. We take the following ansatz for the wavefunction

$$\begin{pmatrix} \psi_A(x \leq 0) \\ \psi_B(x \leq 0) \end{pmatrix} = e^{i k_- x} \begin{pmatrix} \psi_A^- \\ \psi_B^- \end{pmatrix} \quad \text{and} \quad \begin{pmatrix} \psi_A(x > 0) \\ \psi_B(x > 0) \end{pmatrix} = e^{i k_+ x} \begin{pmatrix} \psi_A^+ \\ \psi_B^+ \end{pmatrix}, \tag{S63}$$

where $k_\pm$ are real assuming that $E \geq \varepsilon$. The boundary condition is satisfied if

$$\begin{pmatrix} \psi_A^- \\ \psi_B^- \end{pmatrix} = \begin{pmatrix} \psi_A^+ \\ \psi_B^+ \end{pmatrix}. \tag{S64}$$

Substituting this ansatz into the differential equations, we obtain

$$\begin{aligned} (\varepsilon - E)\, \psi_A^- + \hbar v_0 (k_- - i k_y)\, \psi_B^- &= 0, \\ \hbar v_0 (k_- + i k_y)\, \psi_A^- + (-\varepsilon - E)\, \psi_B^- &= 0, \\ (\varepsilon - E)\, \psi_A^+ + \hbar v_0 (k_+ - i k_y)\, \psi_B^+ &= 0, \\ \hbar v_0 (k_+ + i k_y)\, \psi_A^+ + (-\varepsilon - E)\, \psi_B^+ &= 0. \end{aligned} \tag{S65}$$

We notice that the first two equations are identical to the last two equations; therefore, solutions to the first two are also solutions to the second two. If either the A or the B sublattice wavefunction vanishes, then $E = \pm\varepsilon$ and $k_\pm = k_y = 0$, e.g. states at the band extrema. For $E \neq 0$, the following conditions must be true:

$$-\frac{\psi_A^-}{\psi_B^-} = \frac{\hbar v_0 (k_- - i k_y)}{\varepsilon - E} = \frac{-\varepsilon - E}{\hbar v_0 (k_- + i k_y)}, \quad \text{and} \quad -\frac{\psi_A^+}{\psi_B^+} = \frac{\hbar v_0 (k_+ - i k_y)}{\varepsilon - E} = \frac{-\varepsilon - E}{\hbar v_0 (k_+ + i k_y)}. \tag{S66}$$

Rearranging, we recover the familiar energy dispersion $E^2 = \varepsilon^2 + (\hbar v_0 k_y)^2 + (\hbar v_0 k_\pm)^2$. The constraint from the boundary condition is $k_+ = k_-$. This shows that an incoming K wave is completely scattered into a reflected K' wave and vice versa. In other words, when $\varepsilon_K = \varepsilon_{K'}$, scattering at an armchair edge completely exchanges the valley flavor.

The preceding analysis seems to pose a contradiction when $\varepsilon_K < \varepsilon_{K'}$. In the energy window $\varepsilon_K < E < \varepsilon_{K'}$, there are no propagating states in the K' valley into which to an incoming K wave can scatter. So to where does an incoming K wave scatter? Of course, an incoming K wave can *only* scatter into an outgoing, reflected K wave since these are the only propagating states available in the bulk. In this energy window, there are no *propagating* K' states but there are *evanescent* K' states which act as scattering centers to reflect the incoming K waves into outgoing K waves. For higher energies $E > \varepsilon_{K'} > \varepsilon_K$, there are both K and K' waves into which an incoming K wave can scatter; and in general, this reflection process depolarizes the valley character of the outgoing wave. Only in the special case where $\varepsilon_K = \varepsilon_{K'}$ is the reflected wave also valley polarized (but in the opposite valley compared to the incoming wave). We now validate these claims with scattering calculations, which are similar in spirit to the calculation done in Ref. [2].

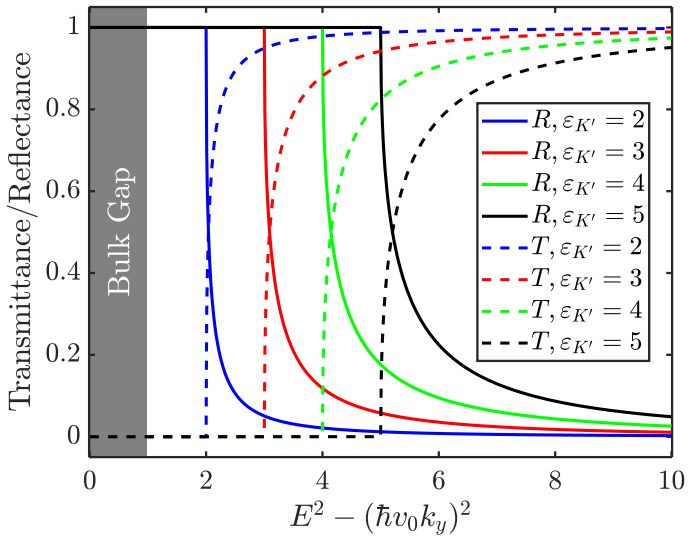

Figure S11. **Transmittance and reflectance as a function of energy, as defined in Eq.** (S72)**.** Here, $\varepsilon_K = 1$ sets the energy scale. Solid (dashed) lines show the reflectance (transmittance). For energies below $\varepsilon_{K'}$, we have unity reflectance. For large energies, we have near unity transmittance. For energies below ε_K, neither transmittance nor reflectance is defined since inside the bulk gap, there are propagating states.

For $\sqrt{\varepsilon_K^2+(\hbar v_0 k_y)^2} \le E < \sqrt{\varepsilon_{K'}^2+(\hbar v_0 k_y)^2}$, assuming positive E throughout, the bulk states are given by

$$\begin{aligned}\begin{pmatrix}\psi_A(x\le 0)\\ \psi_B(x\le 0)\end{pmatrix} &= e^{ik_x x}\begin{pmatrix}\varepsilon_K+E\\ \hbar v_0\,(k_x+ik_y)\end{pmatrix} + \mathfrak{r}e^{-ik_x x}\begin{pmatrix}\varepsilon_K+E\\ \hbar v_0\,(-k_x+ik_y)\end{pmatrix},\\ \begin{pmatrix}\psi_A(x> 0)\\ \psi_B(x> 0)\end{pmatrix} &= \mathfrak{t}e^{-\kappa_x x}\begin{pmatrix}\varepsilon_{K'}+E\\ i\hbar v_0\,(\kappa_x+k_y)\end{pmatrix},\end{aligned} \tag{S67}$$

where $E=\sqrt{\varepsilon_K^2+\hbar^2v_0^2k_x^2+\hbar^2v_0^2k_y^2}=\sqrt{\varepsilon_{K'}^2-\hbar^2v_0^2\kappa_x^2+\hbar^2v_0^2k_y^2}$. Matching the boundary condition, we find

$$\begin{aligned}\mathfrak{r} &= -1+\frac{2(\varepsilon_{K'}+E)k_x}{E(i\kappa_x+k_x)+\varepsilon_{K'}(k_x-ik_y)+i\varepsilon_K(\kappa_x+k_y)},\\ \mathfrak{t} &= -\frac{2i(\varepsilon_K+E)k_x}{E(\kappa_x-ik_x)-\varepsilon_{K'}(ik_x+k_y)+\varepsilon_K(\kappa_x+k_y)}.\end{aligned} \tag{S68}$$

We have verified that $|\mathfrak{r}|=1$, demonstrating that the entire incoming wave is reflected to the *same* valley. It is worth pointing out that the evanescent wave carries current in the direction parallel to the armchair edge. The current operator along the y-direction is $\hat{J}_y=-ev_0\sigma_2$. Even for $k_y=0$, this current is nonzero:

$$\langle\hat{J}_y\rangle \propto -ev_0\mathfrak{t}^\dagger\mathfrak{t}(\varepsilon_{K'}+E)\neq 0. \tag{S69}$$

Now, for $E\ge\sqrt{\varepsilon_{K'}^2+(\hbar v_0k_y)^2}>\sqrt{\varepsilon_K^2+(\hbar v_0k_y)^2}$, we study first the scattering of an incoming K wave

$$\begin{aligned}\begin{pmatrix}\psi_A(x\le 0)\\ \psi_B(x\le 0)\end{pmatrix} &= e^{ik_x x}\begin{pmatrix}\varepsilon_K+E\\ \hbar v_0\,(k_x+ik_y)\end{pmatrix} + \mathfrak{r}e^{-ik_x x}\begin{pmatrix}\varepsilon_K+E\\ \hbar v_0\,(-k_x+ik_y)\end{pmatrix},\\ \begin{pmatrix}\psi_A(x> 0)\\ \psi_B(x> 0)\end{pmatrix} &= \mathfrak{t}e^{ip_x x}\begin{pmatrix}\varepsilon_{K'}+E\\ \hbar v_0\,(p_x+ik_y)\end{pmatrix},\end{aligned} \tag{S70}$$

where $E=\sqrt{\varepsilon_K^2+\hbar^2v_0^2k_x^2+\hbar^2v_0^2k_y^2}=\sqrt{\varepsilon_{K'}^2+\hbar^2v_0^2p_x^2+\hbar^2v_0^2k_y^2}$. Matching the boundary condition, we find

$$\begin{aligned}\mathfrak{r} &= -1+\frac{2(\varepsilon_{K'}+E)k_x}{\varepsilon_K p_x+Ep_x+\varepsilon_{K'}k_x+Ek_x+i(\varepsilon_K-\varepsilon_{K'})k_y},\\ \mathfrak{t} &= \frac{2(\varepsilon_K+E)k_x}{\varepsilon_K p_x+Ep_x+\varepsilon_{K'}k_x+Ek_x+i(\varepsilon_K-\varepsilon_{K'})k_y}.\end{aligned} \tag{S71}$$

As a check of consistency, if $\varepsilon_K = \varepsilon_{K'}$, then $k_x = p_x$, $\mathfrak{r} = 0$, and $\mathfrak{t} = 1$, showing once again that the entire incoming wave is reflected to the *opposite* valley. In general, the reflectance and transmittance are given by

$$\begin{aligned}\mathfrak{R}(E,k_y) &= \frac{E^2-\varepsilon_K\varepsilon_{K'}-(\hbar v_0 k_y)^2-\sqrt{E^2-\varepsilon_K^2-(\hbar v_0 k_y)^2}\sqrt{E^2-\varepsilon_{K'}^2-(\hbar v_0 k_y)^2}}{E^2-\varepsilon_K\varepsilon_{K'}-(\hbar v_0 k_y)^2+\sqrt{E^2-\varepsilon_K^2-(\hbar v_0 k_y)^2}\sqrt{E^2-\varepsilon_{K'}^2-(\hbar v_0 k_y)^2}},\\ \mathfrak{T}(E,k_y) &= \frac{2\sqrt{E^2-\varepsilon_K^2-(\hbar v_0 k_y)^2}\sqrt{E^2-\varepsilon_{K'}^2-(\hbar v_0 k_y)^2}}{E^2-\varepsilon_K\varepsilon_{K'}-(\hbar v_0 k_y)^2+\sqrt{E^2-\varepsilon_K^2-(\hbar v_0 k_y)^2}\sqrt{E^2-\varepsilon_{K'}^2-(\hbar v_0 k_y)^2}}.\end{aligned} \tag{S72}$$

Again, these formulas are valid when $E^2-(\hbar v_0 k_y)^2 \geq \varepsilon_{K'}^2 > \varepsilon_K^2$, where we clearly have $\mathfrak{R}(E,k_y)+\mathfrak{T}(E,k_y)=1$. From these formulas, it is clear that if $E^2-(\hbar v_0 k_y)^2 = \varepsilon_{K'}^2$, we have perfect reflection to the *same* valley. Furthermore, we have

$$\lim_{E^2-(\hbar v_0 k_y)^2\to\infty}\mathfrak{T}(E,k_y)=1 \quad \text{and} \quad \lim_{E^2-(\hbar v_0 k_y)^2\to\infty}\mathfrak{R}(E,k_y)=0. \tag{S73}$$

In other words, when $E^2-(\hbar v_0 k_y)^2$ is much larger than both ε_K and $\varepsilon_{K'}$, we revert back to the situation where an incoming K wave is completely scattered into an outgoing K' wave. A plot of $\mathfrak{R}$ and $\mathfrak{T}$ for general energies is shown in Fig. S11. All of the limits noted above can be observed in this plot as well. For completeness, we now consider the situation where the incoming wave comes from the K' valley. In this case, we

$$\begin{aligned}\begin{pmatrix}\psi_A(x\leq 0)\\ \psi_B(x\leq 0)\end{pmatrix} &= \mathfrak{t}e^{-ik_x x}\begin{pmatrix}\varepsilon_K+E\\ \hbar v_0(-k_x+ik_y)\end{pmatrix},\\ \begin{pmatrix}\psi_A(x>0)\\ \psi_B(x>0)\end{pmatrix} &= e^{-ip_x x}\begin{pmatrix}\varepsilon_{K'}+E\\ \hbar v_0(-p_x+ik_y)\end{pmatrix}+\mathfrak{r}e^{ip_x x}\begin{pmatrix}\varepsilon_{K'}+E\\ \hbar v_0(p_x+ik_y)\end{pmatrix},\end{aligned} \tag{S74}$$

where, again, $E=\sqrt{\varepsilon_K^2+\hbar^2v_0^2k_x^2+\hbar^2v_0^2k_y^2}=\sqrt{\varepsilon_{K'}^2+\hbar^2v_0^2p_x^2+\hbar^2v_0^2k_y^2}$. Eq. (S74) is formally equivalent to Eq. (S70) with $\varepsilon_K \leftrightarrow \varepsilon_{K'}$ and $k_x \leftrightarrow -p_x$. Therefore, all of the preceding analysis applies; in particular, the transmittance and reflectance functions remain the same.

The above results are easily generalized to a slightly different situation where the sublattice gap is only rigidly shifted, instead of being modulated, depending on valleys. In this case, the Hamiltonian takes the following form

$$\hat{\mathcal{H}}_{\text{eff}}(\mathbf{k})=\begin{pmatrix}\hat{\mathcal{H}}_K(\mathbf{k}) & 0\\ 0 & \hat{\mathcal{H}}_{K'}(\mathbf{k})\end{pmatrix}=\begin{pmatrix}\varepsilon & \hbar v_0(k_x-ik_y) & 0 & 0\\ \hbar v_0(k_x+ik_y) & -\varepsilon & 0 & 0\\ 0 & 0 & \varepsilon+\delta\varepsilon & \hbar v_0(-k_x-ik_y)\\ 0 & 0 & \hbar v_0(-k_x+ik_y) & -\varepsilon+\delta\varepsilon\end{pmatrix}, \tag{S75}$$

where we assume $0<\delta\varepsilon<\varepsilon$. When $\sqrt{\varepsilon^2+(\hbar v_0 k_y)^2}\leq E<\delta\varepsilon+\sqrt{\varepsilon^2+(\hbar v_0 k_y)^2}$, we must have perfect reflection to the same valley. When $E>\delta\varepsilon+\sqrt{\varepsilon^2+(\hbar v_0 k_y)^2}$, the scattering states with an incoming K wave are

$$\begin{aligned}\begin{pmatrix}\psi_A(x\leq 0)\\ \psi_B(x\leq 0)\end{pmatrix} &= e^{ik_x x}\begin{pmatrix}\varepsilon+E\\ \hbar v_0(k_x+ik_y)\end{pmatrix}+\mathfrak{r}e^{-ik_x x}\begin{pmatrix}\varepsilon+E\\ \hbar v_0(-k_x+ik_y)\end{pmatrix},\\ \begin{pmatrix}\psi_A(x>0)\\ \psi_B(x>0)\end{pmatrix} &= \mathfrak{t}e^{ip_x x}\begin{pmatrix}\varepsilon+E-\delta\varepsilon\\ \hbar v_0(p_x+ik_y)\end{pmatrix},\end{aligned} \tag{S76}$$

where $E=\sqrt{\varepsilon^2+\hbar^2v_0^2k_x^2+\hbar^2v_0^2k_y^2}=\delta\varepsilon+\sqrt{\varepsilon^2+\hbar^2v_0^2p_x^2+\hbar^2v_0^2k_y^2}$. Matching boundary condition, we obtain

$$\begin{aligned}\mathfrak{R}(E,k_y) &= \frac{(E-\delta\varepsilon)E-\varepsilon^2-(\hbar v_0 k_y)^2-\sqrt{(E-\delta\varepsilon)^2-\varepsilon^2-(\hbar v_0 k_y)^2}\sqrt{E^2-\varepsilon^2-(\hbar v_0 k_y)^2}}{(E-\delta\varepsilon)E-\varepsilon^2-(\hbar v_0 k_y)^2+\sqrt{(E-\delta\varepsilon)^2-\varepsilon^2-(\hbar v_0 k_y)^2}\sqrt{E^2-\varepsilon^2-(\hbar v_0 k_y)^2}},\\ \mathfrak{T}(E,k_y) &= \frac{2\sqrt{(E-\delta\varepsilon)^2-\varepsilon^2-(\hbar v_0 k_y)^2}\sqrt{E^2-\varepsilon^2-(\hbar v_0 k_y)^2}}{(E-\delta\varepsilon)E-\varepsilon^2-(\hbar v_0 k_y)^2+\sqrt{(E-\delta\varepsilon)^2-\varepsilon^2-(\hbar v_0 k_y)^2}\sqrt{E^2-\varepsilon^2-(\hbar v_0 k_y)^2}},\end{aligned} \tag{S77}$$

which is nearly identical to the previous result. Therefore, the general conclusions regarding wave transmission and reflection in the presence of a valley imbalance are robust. In particular, without valley imbalance, an incoming K wave is reflected perfectly

into an outgoing K' wave. In the presence of a valley imbalance, say where there are propagating K states but only localized K' states, then an incoming K wave is reflected entirely into an outgoing K wave, as it must. For higher energies, where there are both propagating K and K' states but at different wavevectors due to valley imbalance, then an incoming K wave is generically reflected into both an outing K and K' wave.

We end this section by considering the N-layer generalization with Hamiltonian given by

$$\hat{\mathcal{H}}_{\text{eff}}(\mathbf{k}) = \begin{pmatrix} \hat{\mathcal{H}}_K(\mathbf{k}) & 0 \\ 0 & \hat{\mathcal{H}}_{K'}(\mathbf{k}) \end{pmatrix} = \begin{pmatrix} \varepsilon_K & (k_x - ik_y)^N & 0 & 0 \\ (k_x + ik_y)^N & -\varepsilon_K & 0 & 0 \\ 0 & 0 & \varepsilon_{K'} & (-k_x - ik_y)^N \\ 0 & 0 & (-k_x + ik_y)^N & -\varepsilon_{K'} \end{pmatrix}. \tag{S78}$$

Here, we work in units where k^N has the same dimension as energy. It is instructive to look at the particular case $N = 2$ first. In this case, the (positive) energies are given by $E = \sqrt{\varepsilon_{K,K'}^2 + \left(k_x^2 + k_y^2\right)^2}$. Solving for k_x, we obtain

$$k_x = \pm\sqrt{\pm\sqrt{E^2 - \varepsilon_{K,K'}^2} - k_y^2}. \tag{S79}$$

If $\sqrt{\varepsilon_{K,K'}^2 + k_y^4} < E$, we have two real roots and two purely imaginary roots (only one of which is normalizable). If $E < \varepsilon_{K,K'} < \sqrt{\varepsilon_{K,K'}^2 + k_y^4}$, we have four complex roots (only two of which are normalizable). If $\varepsilon_{K,K'} < E < \sqrt{\varepsilon_{K,K'}^2 + k_y^4}$, we have four purely imaginary roots (only two of which are normalizable). The presence of many *additional* evanescent modes contrasts the higher-order theory with the linear-momentum theory previously considered. The number of additional modes is proportional to N since these complex wavevectors originate from taking the N^{th} roots of the energy dispersion. In general, we write the wavevectors

$$k_{\pm n} = \pm\sqrt{|E^2 - \varepsilon_{K,K'}^2|^{1/N} \exp\left(\frac{i\pi\left[1 - \text{sign}(E^2 - \varepsilon_{K,K'}^2)\right]}{2N} + \frac{2\pi i n}{N}\right) - k_y^2}. \tag{S80}$$

For complex roots, we only keep the ones with negative (positive) imaginary part for states on the left (right) side of the boundary that extends to negative (positive) x direction to enforce normalizability. For real roots, we keep both the positive and negative solutions. If $\sqrt{\varepsilon_{K,K'}^2 + k_y^{2N}} < E$, which we always assume for the left side, then we have two real roots and $N-1$ admissible complex roots. If $E < \sqrt{\varepsilon_{K,K'}^2 + k_y^{2N}}$, then there are N complex roots. The boundary condition is derived by enforcing vanishing current at the boundary $\langle\psi|\,\hat{J}_x\,|\psi\rangle = 0$. One such choice is obtained by requiring the wavefunction and all of its derivatives up to the $(N-1)^{\text{th}}$ one to be continuous at the interface. The most general scattering wavefunction with an incoming K wave in this case where there are no propagating states on the right side can be written as

$$\begin{aligned} \begin{pmatrix} \psi_A(x \le 0) \\ \psi_B(x \le 0) \end{pmatrix} &= e^{ik_{+0}x}\begin{pmatrix} \varepsilon_K + E \\ (k_{+0} + ik_y)^N \end{pmatrix} + \mathfrak{r}e^{-ik_{+0}x}\begin{pmatrix} \varepsilon_K + E \\ (-k_{+0} + ik_y)^N \end{pmatrix} + \sum_{n=1}^{N-1} \mathfrak{a}_n e^{i\kappa_{-n}x}\begin{pmatrix} \varepsilon_K + E \\ (\kappa_{-n} + ik_y)^N \end{pmatrix}, \\ \begin{pmatrix} \psi_A(x > 0) \\ \psi_B(x > 0) \end{pmatrix} &= \sum_{n=0}^{N-1} \mathfrak{b}_n e^{i\rho_{+n}x}\begin{pmatrix} \varepsilon_{K'} + E \\ (\rho_{+n} + ik_y)^N \end{pmatrix}, \end{aligned} \tag{S81}$$

where κ_{-n} are complex numbers with negative imaginary parts (so that the exponents contain $e^{|\text{Im}\kappa_{-n}|x}$ which decay as $x \to -\infty$) while ρ_{+n} are complex numbers with positive imaginary parts (so that the exponents contain $e^{-\text{Im}\rho_{+n}x}$ which decay as $x \to +\infty$). Matching boundary condition, we find

$$\begin{aligned} \left[+\mathfrak{r}\left(-ik_{+0}\right)^m + \sum_{n=1}^{N-1} \mathfrak{a}_n \left(i\kappa_{-n}\right)^m\right]\left[\varepsilon_K + E\right] - \left[\sum_{n=0}^{N-1} \mathfrak{b}_n \left(i\rho_{+n}\right)^m\right]\left[\varepsilon_{K'} + E\right] &= -\left(ik_{+0}\right)^m\left[\varepsilon_K + E\right], \\ \mathfrak{r}\left(-ik_{+0}\right)^m\left(-k_{+0} + ik_y\right)^N + \sum_{n=1}^{N-1} \mathfrak{a}_n \left(i\kappa_{-n}\right)^m\left(\kappa_{-n} + ik_y\right)^N - \sum_{n=0}^{N-1} \mathfrak{b}_n \left(i\rho_{+n}\right)^m\left(\rho_{+n} + ik_y\right)^N &= -\left(ik_{+0}\right)^m\left(k_{+0} + ik_y\right)^N, \end{aligned} \tag{S82}$$

for $m = 0, ..., N-1$. We note that there are $2N$ unknowns and $2N$ equations. Therefore, this system of equations is solvable. The reflectance is $|\mathfrak{r}|^2$, which we have checked numerically is always unity. Now, moving onto the case where are propagating modes on both sides of the boundary, the most general scattering wavefunction with an incoming K wave is modified slightly to

$$\begin{aligned}
\begin{pmatrix}\psi_A(x\leq 0)\\ \psi_B(x\leq 0)\end{pmatrix} &= e^{ik_{+0}x}\begin{pmatrix}\varepsilon_K+E\\ (k_{+0}+ik_y)^N\end{pmatrix} + \mathfrak{r}e^{-ik_{+0}x}\begin{pmatrix}\varepsilon_K+E\\ (-k_{+0}+ik_y)^N\end{pmatrix} + \sum_{n=1}^{N-1}\mathfrak{a}_n e^{i\kappa_{-n}x}\begin{pmatrix}\varepsilon_K+E\\ (\kappa_{-n}+ik_y)^N\end{pmatrix},\\
\begin{pmatrix}\psi_A(x>0)\\ \psi_B(x>0)\end{pmatrix} &= \mathfrak{t}e^{ip_{+0}x}\begin{pmatrix}\varepsilon_{K'}+E\\ (p_{+0}+ik_y)^N\end{pmatrix} + \sum_{n=1}^{N-1}\mathfrak{b}_n e^{i\rho_{+n}x}\begin{pmatrix}\varepsilon_{K'}+E\\ (\rho_{+n}+ik_y)^N\end{pmatrix}.
\end{aligned} \tag{S83}$$

Matching the boundary condition is done exactly as before by demanding continuity of the wavefunction and its derivatives at $x = 0$. The transmittance and reflectance are defined in the usual way

$$\mathfrak{R}(E,k_y) = |\mathfrak{r}(E,k_y)|^2 \quad \text{and} \quad \mathfrak{T} = |\mathfrak{t}(E,k_y)|^2\frac{(\varepsilon_{K'}+E)\left(p_{+0}^2+k_y^2\right)^{N-1}p_{+0}}{(\varepsilon_K+E)\left(k_{+0}^2+k_y^2\right)^{N-1}k_{+0}}. \tag{S84}$$

We have checked numerically that $\mathfrak{R}(E,k_y)+\mathfrak{T}(E,k_y) = 1$ in the appropriate range of energy and parallel momentum. All of the *qualitative* conclusions for the monolayer model apply to the N-layer models without modification. Namely:

1. For $\sqrt{\varepsilon_K^2+k_y^{2N}} < E < \sqrt{\varepsilon_{K'}^2+k_y^{2N}}$, we have total intravalley reflection: an incoming K wave is reflected entirely into an outgoing K wave.
2. The evanescent modes can carry current in the direction parallel to the armchair edge even for $k_y = 0$.
3. For $\sqrt{\varepsilon_K^2+k_y^{2N}} < \sqrt{\varepsilon_{K'}^2+k_y^{2N}} < E$, we have partial intravalley reflection and partial intervalley reflection: an incoming K wave is reflected into both an outgoing K wave and an outgoing K' wave.
4. For $E \to \infty$, we have total intervalley reflection: an incoming K wave is reflected entirely into an outgoing K' wave.

2. *Semi-Infinite Plane*

We employ the standard iterative Green's function method to calculate the surface Green's function [3, 4]. We partition the Hamiltonian in "layers" (this is *not* the same as the number of layers in a rhombohedral stack) that are coupled to each other in the following way

$$\hat{\mathcal{H}} = \begin{pmatrix}\mathcal{H}_{0,0} & \mathcal{V}_0 & 0 & 0 & \dots\\ \mathcal{V}_0^\dagger & \mathcal{H}_{1,1} & \mathcal{V} & 0 & \dots\\ 0 & \mathcal{V}^\dagger & \mathcal{H}_{2,2} & \mathcal{V} & \dots\\ 0 & 0 & \mathcal{V}^\dagger & \mathcal{H}_{3,3} & \dots\\ \vdots & \vdots & \vdots & \vdots & \ddots\end{pmatrix}. \tag{S85}$$

$\mathcal{H}_{0,0}$ is the surface Hamiltonian. For a *bulk* homogeneous system, $\mathcal{H}_{i\neq 0, i\neq 0} = \mathcal{H}_{1,1}$, which we now assume. The Green's function is defined as the resolvent of the Hamiltonian $\hat{\mathcal{G}}(\omega) = \left(\omega - \hat{\mathcal{H}}\right)^{-1}$. Internal indices, including parallel momentum, are left implicit. Using the identity $\left(\omega - \hat{\mathcal{H}}\right)\hat{\mathcal{G}}(\omega) = \mathbb{1}$, we obtain the following

$$\sum_a \left(\omega\delta_{i,a} - \mathcal{H}_{i,a}\right)\mathcal{G}_{a,j}(\omega) = \delta_{i,j}. \tag{S86}$$

Because the Hamiltonian is tridiagonal, this equation simplifies significantly

$$\begin{aligned}
\left(\omega - \mathcal{H}_{0,0}\right)\mathcal{G}_{0,0}(\omega) &= 1 + \mathcal{V}_0\mathcal{G}_{1,0}(\omega),\\
\left(\omega - \mathcal{H}_{1,1}\right)\mathcal{G}_{1,0}(\omega) &= \mathcal{V}_0^\dagger\mathcal{G}_{0,0}(\omega) + \mathcal{V}\mathcal{G}_{2,0}(\omega)\\
&\vdots\\
\left(\omega - \mathcal{H}_{1,1}\right)\mathcal{G}_{i,0}(\omega) &= \mathcal{V}^\dagger\mathcal{G}_{i-1,0}(\omega) + \mathcal{V}\mathcal{G}_{i+1,0}(\omega).
\end{aligned} \tag{S87}$$

We solve for $\mathcal{G}_{0,0}(\omega)$ iteratively as follows. In the first step, we substitute in $\mathcal{G}_{1,0}(\omega)$ from the second equation into the first equation to obtain

$$\left(\omega - \mathcal{H}_{0,0} - \mathcal{V}_0 \left[\omega - \mathcal{H}_{1,1}\right]^{-1} \mathcal{V}_0^\dagger\right) \mathcal{G}_{0,0}(\omega) = 1 + \mathcal{V}_0 \left[\omega - \mathcal{H}_{1,1}\right]^{-1} \mathcal{V}\mathcal{G}_{2,0}(\omega). \tag{S88}$$

Because we need $\mathcal{G}_{2,0}(\omega)$ to solve for $\mathcal{G}_{0,0}(\omega)$ now, we use the following equation to relate Green's functions that differ by two (inner) layers

$$\begin{aligned}
\left(\omega - \mathcal{H}_{1,1} - \mathcal{V}^\dagger \left[\omega - \mathcal{H}_{1,1}\right]^{-1} \mathcal{V} - \mathcal{V} \left[\omega - \mathcal{H}_{1,1}\right]^{-1} \mathcal{V}^\dagger\right) \mathcal{G}_{2,0}(\omega) &= \mathcal{V}^\dagger \left[\omega - \mathcal{H}_{1,1}\right]^{-1} \mathcal{V}_0^\dagger \mathcal{G}_{0,0}(\omega) + \mathcal{V} \left[\omega - \mathcal{H}_{1,1}\right]^{-1} \mathcal{V}\mathcal{G}_{4,0}(\omega), \\
\left(\omega - \mathcal{H}_{1,1} - \mathcal{V}^\dagger \left[\omega - \mathcal{H}_{1,1}\right]^{-1} \mathcal{V} - \mathcal{V} \left[\omega - \mathcal{H}_{1,1}\right]^{-1} \mathcal{V}^\dagger\right) \mathcal{G}_{4,0}(\omega) &= \mathcal{V}^\dagger \left[\omega - \mathcal{H}_{1,1}\right]^{-1} \mathcal{V}^\dagger \mathcal{G}_{2,0}(\omega) + \mathcal{V} \left[\omega - \mathcal{H}_{1,1}\right]^{-1} \mathcal{V}\mathcal{G}_{6,0}(\omega), \\
&\vdots
\end{aligned} \tag{S89}$$

To simplify, we define (the superscripts denote iteration step)

$$\begin{aligned}
\mathcal{E}_0^{(1)} &= \mathcal{H}_{0,0} + \mathcal{V}_0 \left[\omega - \mathcal{H}_{1,1}\right]^{-1} \mathcal{V}_0^\dagger, \\
\mathcal{E}^{(1)} &= \mathcal{H}_{1,1} + \mathcal{V}^\dagger \left[\omega - \mathcal{H}_{1,1}\right]^{-1} \mathcal{V} + \mathcal{V} \left[\omega - \mathcal{H}_{1,1}\right]^{-1} \mathcal{V}^\dagger, \\
\alpha_0^{(1)} &= \mathcal{V}_0 \left[\omega - \mathcal{H}_{1,1}\right]^{-1} \mathcal{V}, \\
\beta_0^{(1)} &= \mathcal{V}^\dagger \left[\omega - \mathcal{H}_{1,1}\right]^{-1} \mathcal{V}_0^\dagger, \\
\alpha^{(1)} &= \mathcal{V} \left[\omega - \mathcal{H}_{1,1}\right]^{-1} \mathcal{V}, \\
\beta^{(1)} &= \mathcal{V}^\dagger \left[\omega - \mathcal{H}_{1,1}\right]^{-1} \mathcal{V}^\dagger,
\end{aligned} \tag{S90}$$

to obtain

$$\begin{aligned}
\left(\omega - \mathcal{E}_0^{(1)}\right) \mathcal{G}_{0,0}(\omega) &= 1 + \alpha_0^{(1)} \mathcal{G}_{2,0}(\omega), \\
\left(\omega - \mathcal{E}^{(1)}\right) \mathcal{G}_{2,0}(\omega) &= \beta_0^{(1)} \mathcal{G}_{0,0}(\omega) + \alpha^{(1)} \mathcal{G}_{4,0}(\omega), \\
\left(\omega - \mathcal{E}^{(1)}\right) \mathcal{G}_{4,0}(\omega) &= \beta^{(1)} \mathcal{G}_{2,0}(\omega) + \alpha^{(1)} \mathcal{G}_{6,0}(\omega), \\
&\vdots
\end{aligned} \tag{S91}$$

In the second iteration, we obtain

$$\begin{aligned}
&\left(\omega - \mathcal{E}_0^{(1)} - \alpha_0^{(1)} \left[\omega - \mathcal{E}^{(1)}\right]^{-1} \beta_0^{(1)}\right) \mathcal{G}_{0,0}(\omega) = 1 + \alpha_0^{(1)} \left[\omega - \mathcal{E}^{(1)}\right]^{-1} \alpha^{(1)} \mathcal{G}_{4,0}(\omega), \\
&\left(\omega - \mathcal{E}^{(1)} - \beta^{(1)} \left[\omega - \mathcal{E}^{(1)}\right]^{-1} \alpha^{(1)} - \alpha^{(1)} \left[\omega - \mathcal{E}^{(1)}\right]^{-1} \beta^{(1)}\right) \mathcal{G}_{4,0}(\omega) \\
&= \beta^{(1)} \left[\omega - \mathcal{E}^{(1)}\right]^{-1} \beta_0^{(1)} \mathcal{G}_{0,0}(\omega) + \alpha^{(1)} \left[\omega - \mathcal{E}^{(1)}\right]^{-1} \alpha^{(1)} \mathcal{G}_{8,0}(\omega), \\
&\left(\omega - \mathcal{E}^{(1)} - \beta^{(1)} \left[\omega - \mathcal{E}^{(1)}\right]^{-1} \alpha^{(1)} - \alpha^{(1)} \left[\omega - \mathcal{E}^{(1)}\right]^{-1} \beta^{(1)}\right) \mathcal{G}_{8,0}(\omega) \\
&= \beta^{(1)} \left[\omega - \mathcal{E}^{(1)}\right]^{-1} \beta^{(1)} \mathcal{G}_{4,0}(\omega) + \alpha^{(1)} \left[\omega - \mathcal{E}^{(1)}\right]^{-1} \alpha^{(1)} \mathcal{G}_{12,0}(\omega), \\
&\vdots
\end{aligned} \tag{S92}$$

from which it is evident that we can define the iterative procedure at the n^{th} step as

$$\begin{aligned}
\mathcal{E}_0^{(n)} &= \mathcal{E}_0^{(n-1)} + \alpha_0^{(n-1)} \left[\omega - \mathcal{E}^{(n-1)}\right]^{-1} \beta_0^{(n-1)}, \\
\mathcal{E}^{(n)} &= \mathcal{E}^{(n-1)} + \beta^{(n-1)} \left[\omega - \mathcal{E}^{(n-1)}\right]^{-1} \alpha^{(n-1)} + \alpha^{(n-1)} \left[\omega - \mathcal{E}^{(n-1)}\right]^{-1} \beta^{(n-1)}, \\
\alpha_0^{(n)} &= \alpha_0^{(n-1)} \left[\omega - \mathcal{E}^{(n-1)}\right]^{-1} \alpha^{(n-1)}, \\
\beta_0^{(n)} &= \beta^{(n-1)} \left[\omega - \mathcal{E}^{(n-1)}\right]^{-1} \beta_0^{(n-1)}, \\
\alpha^{(n)} &= \alpha^{(n-1)} \left[\omega - \mathcal{E}^{(n-1)}\right]^{-1} \alpha^{(n-1)}, \\
\beta^{(n)} &= \beta^{(n-1)} \left[\omega - \mathcal{E}^{(n-1)}\right]^{-1} \beta^{(n-1)}.
\end{aligned} \tag{S93}$$

At this step, the Green's function satisfies

$$\left(\omega - \mathcal{E}_0^{(n)}\right) \mathcal{G}_{0,0}(\omega) = 1 + \alpha_0^{(n)} \mathcal{G}_{2^n,0}(\omega). \tag{S94}$$

We terminate the iterative loop at some critical n^* when $\left\|\alpha_0^{(n^*)}\right\| < \text{tol}$, where tol is some small convergence parameter. At this critical step, the surface Green's function is appropriately given by

$$\mathcal{G}_{0,0}(\omega) \approx \left(\omega - \mathcal{E}_0^{(n^*)}\right)^{-1}. \tag{S95}$$

The spectral weight at energy ω is computed using this approximated surface Green's function by

$$A(\omega) = -\lim_{\eta \to 0^+} \frac{1}{\pi} \text{ImTr} \mathcal{G}_{0,0}(\omega = E + i\eta). \tag{S96}$$

B. Transmission and Reflection at an Armchair Domain Wall

1. *Continuum Description of a Step-Function Domain Wall*

Here, we extend the results of Sec. II A to study transmission and reflection due to an abrupt domain wall that switches the sense of valley polarization. A similar, but different, analysis for bilayer graphene is undertaken by Ref. [5]. The domain wall is located at $x = 0$ and runs along the armchair direction. To model this system, we first consider the Hamiltonian of a monolayer graphene sheet with a valley-dependent mass gap that varies along the x-direction

$$\hat{\mathcal{H}}_{\text{eff}}(\mathbf{k}) = \begin{pmatrix} \varepsilon_K(x) & \hbar v_0 \left(k_x - i k_y\right) & 0 & 0 \\ \hbar v_0 \left(k_x + i k_y\right) & -\varepsilon_K(x) & 0 & 0 \\ 0 & 0 & \varepsilon_{K'}(x) & \hbar v_0 \left(-k_x - i k_y\right) \\ 0 & 0 & \hbar v_0 \left(-k_x + i k_y\right) & -\varepsilon_{K'}(x) \end{pmatrix}. \tag{S97}$$

We take the gap function to be

$$\varepsilon_K(x) = \begin{cases} \varepsilon_- & x \leq 0 \\ \varepsilon_+ & x > 0 \end{cases} \quad \text{and} \quad \varepsilon_{K'}(x) = \begin{cases} \varepsilon_+ & x \leq 0 \\ \varepsilon_- & x > 0 \end{cases}, \tag{S98}$$

where we assume that $0 < \varepsilon_- < \varepsilon_+$. That is, for $x < 0$, the gap at K is smaller than the gap at K' and the opposite is true for $x > 0$. Now, let us consider the case where $\sqrt{\varepsilon_-^2 + (\hbar v_0 k_y)^2} \leq E < \sqrt{\varepsilon_+^2 + (\hbar v_0 k_y)^2}$ where the wavefunction can be written as

$$\begin{aligned}
\begin{pmatrix} \psi_{A,K}(x \leq 0) \\ \psi_{B,K}(x \leq 0) \\ \psi_{A,K'}(x \leq 0) \\ \psi_{B,K'}(x \leq 0) \end{pmatrix} &= e^{ik_x x} \begin{pmatrix} \varepsilon_- + E \\ \hbar v_0 (k_x + i k_y) \\ 0 \\ 0 \end{pmatrix} + \mathfrak{r}_K e^{-ik_x x} \begin{pmatrix} \varepsilon_- + E \\ \hbar v_0 (-k_x + i k_y) \\ 0 \\ 0 \end{pmatrix} + \mathfrak{r}_{K'} e^{+\kappa_x x} \begin{pmatrix} 0 \\ 0 \\ \varepsilon_+ + E \\ i\hbar v_0 (\kappa_x + k_y) \end{pmatrix}, \\
\begin{pmatrix} \psi_{A,K}(x > 0) \\ \psi_{B,K}(x > 0) \\ \psi_{A,K'}(x > 0) \\ \psi_{B,K'}(x > 0) \end{pmatrix} &= \mathfrak{t}_K e^{-\kappa_x x} \begin{pmatrix} \varepsilon_+ + E \\ i\hbar v_0 (\kappa_x + k_y) \\ 0 \\ 0 \end{pmatrix} + \mathfrak{t}_{K'} e^{+ik_x x} \begin{pmatrix} 0 \\ 0 \\ \varepsilon_- + E \\ \hbar v_0 (-k_x + i k_y) \end{pmatrix}.
\end{aligned} \tag{S99}$$

The energy dispersion is given by $E = \sqrt{\varepsilon_-^2 + (\hbar v_0 k_x)^2 + (\hbar v_0 k_y)^2} = \sqrt{\varepsilon_+^2 - (\hbar v_0 \kappa_x)^2 + (\hbar v_0 k_y)^2}$. We enforce the boundary condition by demanding continuity of the current along the x-direction. This can be achieved by making the wavefunction continuous at $x = 0$. Matching the boundary condition yields $\mathfrak{r}_{K'} = \mathfrak{t}_{K'} = 0$ and

$$\begin{aligned}\mathfrak{r}_K &= -1 + \frac{2(\varepsilon_+ + E)k_x}{E(i\kappa_x + k_x) + \varepsilon_+(k_x - ik_y) + i\varepsilon_-(\kappa_x + k_y)},\\ \mathfrak{t}_K &= -\frac{2i(\varepsilon_- + E)k_x}{E(\kappa_x - ik_x) - \varepsilon_+(ik_x + k_y) + \varepsilon_-(\kappa_x + k_y)}.\end{aligned} \tag{S100}$$

We find $|\mathfrak{r}_K| = 1$. This demonstrates perfect reflection. An incoming K wave is reflected completely into an outgoing K wave. There is no transmission to the other side. The calculation here bears resemblance to the calculation done for the armchair boundary above. However, it is important to note that the evanescent state here resides in the K valley in contrast to the evanescent wave that resides in the K' valley for the armchair boundary. Similar to before, the evanescent mode, even for $k_y = 0$, carries current in the direction parallel to the domain wall.

We now generalize the above result to the N-layer situation. Again, this is very similar to the armchair calculation, but we need to keep all four degrees of freedom on both sides of the boundary. The Hamiltonian is

$$\hat{\mathcal{H}}_{\text{eff}}(\mathbf{k}) = \begin{pmatrix} \varepsilon_K(x) & (k_x - ik_y)^N & 0 & 0 \\ (k_x + ik_y)^N & -\varepsilon_K(x) & 0 & 0 \\ 0 & 0 & \varepsilon_{K'}(x) & (-k_x - ik_y)^N \\ 0 & 0 & (-k_x + ik_y)^N & -\varepsilon_{K'}(x) \end{pmatrix}. \tag{S101}$$

The valley-dependent mass gap is taken to be of the same form as in Eq. (S98). For a fixed k_y and E, we have $2N$ *complex* wavevectors for each valley and each side of the domain wall given by

$$k_{\pm n} = \pm\sqrt{|E^2 - \varepsilon_{+/-}^2|^{1/N} \exp\left(\frac{i\pi\left[1 - \text{sign}\left(E^2 - \varepsilon_{+/-}^2\right)\right]}{2N} + \frac{2\pi i n}{N}\right) - k_y^2}, \tag{S102}$$

where $n \in \{0, 1, ..., N-1\}$. We always work in the energy regime where there are two *real* wavevectors on the left in the K valley, $E > \sqrt{\varepsilon_-^2 + k_y^{2N}}$. Of the $2(N-1)$ complex roots remaining, we only take half of them which are normalizable. On the left-hand side, we only take complex roots which have negative imaginary parts, while on the right-hand side, we only take complex roots which have positive imaginary parts. If $E < \sqrt{\varepsilon_+^2 + k_y^{2N}}$, then there are only complex roots, and again, we choose only half of them which are normalizable. It is worth pointing out that there are evanescent modes on both sides of the domain wall for the N-layer situation, which contrasts with the monolayer case where the evanescent modes reside on the opposite sides to the propagating modes. The wavefunction can be written as

$$\begin{aligned}\begin{pmatrix}\psi_{A,K}(x\le 0)\\ \psi_{B,K}(x\le 0)\\ \psi_{A,K'}(x\le 0)\\ \psi_{B,K'}(x\le 0)\end{pmatrix} &= e^{ik_{+0}x}\begin{pmatrix}\varepsilon_- + E\\ (k_{+0} + ik_y)^N\\ 0\\ 0\end{pmatrix} + \mathfrak{r}_K e^{-ik_{+0}x}\begin{pmatrix}\varepsilon_- + E\\ (-k_{+0} + ik_y)^N\\ 0\\ 0\end{pmatrix}\\ &\quad + \sum_{n=1}^{N-1}\mathfrak{a}_n e^{i\kappa_{-n}x}\begin{pmatrix}\varepsilon_- + E\\ (\kappa_{-n} + ik_y)^N\\ 0\\ 0\end{pmatrix} + \sum_{n=0}^{N-1}\mathfrak{b}_n e^{i\rho_{-n}x}\begin{pmatrix}0\\ 0\\ \varepsilon_+ + E\\ (-\rho_{-n} + ik_y)^N\end{pmatrix},\\ \begin{pmatrix}\psi_{A,K}(x> 0)\\ \psi_{B,K}(x> 0)\\ \psi_{A,K'}(x> 0)\\ \psi_{B,K'}(x> 0)\end{pmatrix} &= \sum_{n=0}^{N-1}\mathfrak{c}_n e^{i\rho_{+n}x}\begin{pmatrix}\varepsilon_+ + E\\ (\rho_{+n} + ik_y)^N\\ 0\\ 0\end{pmatrix} + \sum_{n=1}^{N-1}\mathfrak{d}_n e^{i\kappa_{+n}x}\begin{pmatrix}0\\ 0\\ \varepsilon_- + E\\ (-\kappa_{+n} + ik_y)^N\end{pmatrix}\\ &\quad + \mathfrak{t}_{K'} e^{+ik_{+0}x}\begin{pmatrix}0\\ 0\\ \varepsilon_- + E\\ (-k_{+0} + ik_y)^N\end{pmatrix}.\end{aligned} \tag{S103}$$

Here, we use a slightly different notation for the wavevectors to emphasize their signs and dependence on the energies. k is used for purely real values while $\kappa_\pm$ and $\rho_\pm$ are used to indicate complex values with $\pm$ imaginary parts. $\kappa_\pm$ uses ε_- in its calculation

while $\rho_\pm$ uses ε_+ in its calculation. Now, enforcing continuity at the domain wall, we obtain

$$\begin{aligned}
\left[\mathfrak{r}_K(-ik_{+0})^m + \sum_{n=1}^{N-1}\mathfrak{a}_n(i\kappa_{-n})^m\right][\varepsilon_- + E] - \sum_{n=0}^{N-1}\mathfrak{c}_n(i\rho_{+n})^m[\varepsilon_+ + E] &= -(ik_{+0})^m[\varepsilon_- + E],\\
\mathfrak{r}_K(-ik_{+0})^m[-k_{+0} + ik_y]^N + \sum_{n=1}^{N-1}\mathfrak{a}_n(i\kappa_{-n})^m[\kappa_{-n} + ik_y]^N - \sum_{n=0}^{N-1}\mathfrak{c}_n(i\rho_{+n})^m[\rho_{+n} + ik_y]^N &= -(ik_{+0})^m[k_{+0} + ik_y]^N,\\
\sum_{n=0}^{N-1}\mathfrak{b}_n(i\rho_{-n})^m[\varepsilon_+ + E] - \left[\sum_{n=1}^{N-1}\mathfrak{d}_n(i\kappa_{+n})^m + \mathfrak{t}_{K'}(ik_{+0})^m\right][\varepsilon_- + E] &= 0,\\
\sum_{n=0}^{N-1}\mathfrak{b}_n(i\rho_{-n})^m[-\rho_{-n} + ik_y]^N - \sum_{n=1}^{N-1}\mathfrak{d}_n(i\kappa_{+n})^m[-\kappa_{+n} + ik_y]^N - \mathfrak{t}_{K'}(ik_{+0})^m[-k_{+0} + ik_y]^N &= 0.
\end{aligned} \tag{S104}$$

From here, we note that the $\mathfrak{a}_n$ and $\mathfrak{c}_n$ coefficients are completely decoupled from the $\mathfrak{b}_n$ and $\mathfrak{d}_n$ coefficients. In particular, the $\mathfrak{b}_n$ and $\mathfrak{d}_n$ coefficients and $\mathfrak{t}_{K'}$ can always be set to zero and still satisfy the domain-wall continuity condition. We have checked numerically that $|\mathfrak{r}_K| = 1$ for any number of layer as long as the chemical potential lies in the quarter metal phase. This shows that for any number of layers, an abrupt valley domain wall is opaque. Electron waves coming in from one valley must reflect entirely back to that same valley. There can be no transmission!

2. *Green's Function Calculation of a Finite-Width Domain Wall*

To calculate transmission through a domain connected to semi-infinite right and left leads, we use the equilibrium Green's function method [6, 7]. The domain Hamiltonian is written as $\mathcal{H}_D$, while the left and right leads have block form, $\mathcal{H}_L$ and $\mathcal{H}_R$ connected by $\mathcal{V}_L$ and $\mathcal{V}_R$. The hoppings from the leads to the domain are denoted $\mathcal{V}_{LD}$ and $\mathcal{V}_{DR}$. The Hamiltonian has the following form

$$\hat{\mathcal{H}} = \begin{pmatrix}
\ddots & \vdots & \vdots & \vdots & \vdots & \vdots & \vdots & \vdots & \iddots\\
\dots & \mathcal{H}_L & \mathcal{V}_L & 0 & 0 & 0 & 0 & 0 & \dots\\
\dots & \mathcal{V}_L^\dagger & \mathcal{H}_L & \mathcal{V}_L & 0 & 0 & 0 & 0 & \dots\\
\dots & 0 & \mathcal{V}_L^\dagger & \mathcal{H}_L & \mathcal{V}_{LD} & 0 & 0 & 0 & \dots\\
\dots & 0 & 0 & \mathcal{V}_{LD}^\dagger & \mathcal{H}_D & \mathcal{V}_{DR} & 0 & 0 & \dots\\
\dots & 0 & 0 & 0 & \mathcal{V}_{DR}^\dagger & \mathcal{H}_R & \mathcal{V}_R & 0 & \dots\\
\dots & 0 & 0 & 0 & 0 & \mathcal{V}_R^\dagger & \mathcal{H}_R & \mathcal{V}_R & \dots\\
\dots & 0 & 0 & 0 & 0 & 0 & \mathcal{V}_R^\dagger & \mathcal{H}_R & \dots\\
\iddots & \vdots & \vdots & \vdots & \vdots & \vdots & \vdots & \vdots & \ddots
\end{pmatrix}. \tag{S105}$$

This Hamiltonian can be partitioned as follows

$$\begin{aligned}
\hat{\mathcal{H}} &= \begin{pmatrix} \tilde{\mathcal{H}}_L & \tilde{\mathcal{V}}_{LD} & 0\\ \tilde{\mathcal{V}}_{LD}^\dagger & \mathcal{H}_D & \tilde{\mathcal{V}}_{DR}\\ 0 & \tilde{\mathcal{V}}_{DR}^\dagger & \tilde{\mathcal{H}}_R \end{pmatrix},\\
\tilde{\mathcal{H}}_L &= \begin{pmatrix} \ddots & \vdots & \vdots & \vdots\\ \dots & \mathcal{H}_L & \mathcal{V}_L & 0\\ \dots & \mathcal{V}_L^\dagger & \mathcal{H}_L & \mathcal{V}_L\\ \dots & 0 & \mathcal{V}_L^\dagger & \mathcal{H}_L \end{pmatrix}, \quad \tilde{\mathcal{V}}_{LD} = \begin{pmatrix} \vdots\\ 0\\ 0\\ \mathcal{V}_{LD} \end{pmatrix}, \quad \tilde{\mathcal{V}}_{DR} = \begin{pmatrix} \mathcal{V}_{DR} & 0 & 0 & \dots \end{pmatrix}, \quad \tilde{\mathcal{H}}_R = \begin{pmatrix} \mathcal{H}_R & \mathcal{V}_R & 0 & \dots\\ \mathcal{V}_R^\dagger & \mathcal{H}_R & \mathcal{V}_R & \dots\\ 0 & \mathcal{V}_R^\dagger & \mathcal{H}_R & \dots\\ \vdots & \vdots & \vdots & \ddots \end{pmatrix}.
\end{aligned} \tag{S106}$$

Writing the full Green's function as

$$\begin{pmatrix} \omega - \tilde{\mathcal{H}}_L & -\tilde{\mathcal{V}}_{LD} & 0\\ -\tilde{\mathcal{V}}_{LD}^\dagger & \omega - \mathcal{H}_D & -\tilde{\mathcal{V}}_{DR}\\ 0 & -\tilde{\mathcal{V}}_{DR}^\dagger & \omega - \tilde{\mathcal{H}}_R \end{pmatrix} \begin{pmatrix} * & \tilde{\mathcal{G}}_{LD}(\omega) & *\\ * & \mathcal{G}_D(\omega) & *\\ * & \tilde{\mathcal{G}}_{DR}(\omega) & * \end{pmatrix} = \begin{pmatrix} 1 & 0 & 0\\ 0 & 1 & 0\\ 0 & 0 & 1 \end{pmatrix}, \tag{S107}$$

we find the following

$$\begin{aligned}\left(\omega-\tilde{\mathcal{H}}_L\right)\tilde{\mathcal{G}}_{LD}(\omega)&=\tilde{\mathcal{V}}_{LD}\mathcal{G}_D(\omega),\\ \left(\omega-\mathcal{H}_D\right)\mathcal{G}_D(\omega)&=1+\tilde{\mathcal{V}}_{LD}^\dagger\tilde{\mathcal{G}}_{LD}(\omega)+\tilde{\mathcal{V}}_{DR}\tilde{\mathcal{G}}_{DR}(\omega),\\ \left(\omega-\tilde{\mathcal{H}}_R\right)\tilde{\mathcal{G}}_{DR}(\omega)&=\tilde{\mathcal{V}}_{DR}^\dagger\mathcal{G}_D(\omega).\end{aligned}\tag{S108}$$

Solving for $\mathcal{G}_D$, we find

$$\mathcal{G}_D(\omega)=\left[\omega-\mathcal{H}_D-\tilde{\mathcal{V}}_{LD}^\dagger\left[\omega-\tilde{\mathcal{H}}_L\right]^{-1}\tilde{\mathcal{V}}_{LD}-\tilde{\mathcal{V}}_{DR}\left[\omega-\tilde{\mathcal{H}}_R\right]^{-1}\tilde{\mathcal{V}}_{DR}^\dagger\right]^{-1}.\tag{S109}$$

$\left[\omega-\tilde{\mathcal{H}}_L\right]^{-1}$ and $\left[\omega-\tilde{\mathcal{H}}_R\right]^{-1}$ are the full Green's functions of the left and right leads without any effect from the domain wall respectively. However, since the coupling matrices are everywhere zero except at the domain wall, we can replace these with surface Green's functions computed using the iterative method outlined in Sec. II A 2. Therefore, we obtain

$$\mathcal{G}_D(\omega)=\left[\omega-\mathcal{H}_D-\mathcal{V}_{LD}^\dagger\mathcal{G}_{0,L}(\omega)\mathcal{V}_{LD}-\mathcal{V}_{DR}\mathcal{G}_{0,R}(\omega)\mathcal{V}_{DR}^\dagger\right]^{-1}.\tag{S110}$$

To simplify, we define the lead self energies

$$\Sigma_L(\omega)=\mathcal{V}_{LD}^\dagger\mathcal{G}_{0,L}(\omega)\mathcal{V}_{LD}\quad\text{and}\quad\Sigma_R(\omega)=\mathcal{V}_{RD}^\dagger\mathcal{G}_{0,R}(\omega)\mathcal{V}_{RD}.\tag{S111}$$

We also define the level-width functions

$$\Gamma_L(\omega)=i\left(\Sigma_L(\omega)-\Sigma_L^\dagger(\omega)\right)\quad\text{and}\quad\Gamma_R(\omega)=i\left(\Sigma_R(\omega)-\Sigma_R^\dagger(\omega)\right).\tag{S112}$$

Using these various functions, the transmission from left to right is given by the Caroli-Fisher-Lee formula [8, 9]

$$T(E)=\mathrm{tr}\left[\Gamma_L(E)\mathcal{G}_D(E)\Gamma_R(E)\mathcal{G}_D^\dagger(E)\right],\tag{S113}$$

where $\omega=E+i0^+$ is used to define the delayed Green's functions.

III. MODELS OF SUPERCONDUCTIVITY

A. Monolayer Toy Model

Because superconductivity emerges only in the large displacement field limit, it is likely that the superconducting pair function is highly layer polarized. Therefore, let us begin with a one-orbital monolayer model written in a momentum basis centered at $\mathbf{K}$ and not at Γ in the primitive *triangular* Brillouin zone (not yet in the Kekule Brillouin zone). We have

$$\hat{\mathcal{H}}_{\mathrm{BdG}}=\frac{1}{2}\sum_{\mathbf{k}}\begin{pmatrix}\hat{c}_{\mathbf{K}+\mathbf{k}}^\dagger & \hat{c}_{\mathbf{K}-\mathbf{k}}\end{pmatrix}\begin{pmatrix}\varepsilon_{\mathbf{K}}(\mathbf{k})-\mu & \Delta_{\mathbf{K}}(\mathbf{k})\\ \Delta_{\mathbf{K}}^\dagger(\mathbf{k}) & -\varepsilon_{\mathbf{K}}^*(-\mathbf{k})+\mu\end{pmatrix}\begin{pmatrix}\hat{c}_{\mathbf{K}+\mathbf{k}}\\ \hat{c}_{\mathbf{K}-\mathbf{k}}^\dagger\end{pmatrix}.\tag{S114}$$

We write the superconducting gap centered at the zone corner as

$$\hat{\Delta}=\sum_{\mathbf{k}}\hat{c}_{\mathbf{K}+\mathbf{k}}^\dagger\Delta_{\mathbf{K}}(\mathbf{k})\hat{c}_{\mathbf{K}-\mathbf{k}}^\dagger=\sum_{\mathbf{k}}\hat{c}_{\mathbf{K}+\mathbf{k}}^\dagger\Delta_{\mathrm{SC}}\left[\sin(\mathbf{k}\cdot\mathbf{a}_1)+\omega\sin(\mathbf{k}\cdot\mathbf{a}_2)+\omega^\dagger\sin(\mathbf{k}\cdot\mathbf{a}_3)\right]\hat{c}_{\mathbf{K}-\mathbf{k}}^\dagger.\tag{S115}$$

Here, $\omega=e^{2\pi i/3}$ and $\mathbf{a}_1=(a,0),\mathbf{a}_2=(-a/2,\sqrt{3}a/2)$, $\mathbf{a}_3=(-a/2,-\sqrt{3}a/2)$. This gap function is manifestly antisymmetric under $\mathbf{k}\mapsto-\mathbf{k}$ and has a unity phase winding, which can be seen from expanding around $\mathbf{k}=\mathbf{0}$: $\sin(\mathbf{k}\cdot\mathbf{a}_1)+\omega\sin(\mathbf{k}\cdot\mathbf{a}_2)+\omega^\dagger\sin(\mathbf{k}\cdot\mathbf{a}_3)\approx\frac{3}{2}a(k_x+ik_y)$. We rewrite this function in real space

$$\begin{aligned}\hat{\Delta}&=\frac{1}{N}\frac{\Delta_{\mathrm{SC}}}{2i}\sum_{\mathbf{k}}\sum_{\mathbf{r},\mathbf{r}'}e^{i\mathbf{K}\cdot(\mathbf{r}+\mathbf{r}')}e^{i\mathbf{k}\cdot(\mathbf{r}-\mathbf{r}')}\hat{c}_{\mathbf{r}}^\dagger\left(e^{i\mathbf{k}\cdot\mathbf{a}_1}-e^{-i\mathbf{k}\cdot\mathbf{a}_1}+\omega e^{i\mathbf{k}\cdot\mathbf{a}_2}-\omega e^{-i\mathbf{k}\cdot\mathbf{a}_2}+\omega^\dagger e^{i\mathbf{k}\cdot\mathbf{a}_3}-\omega^\dagger e^{-i\mathbf{k}\cdot\mathbf{a}_3}\right)\hat{c}_{\mathbf{r}'}^\dagger\\ &=\frac{\Delta_{\mathrm{SC}}}{2i}\sum_{\mathbf{r}}e^{2i\mathbf{K}\cdot\mathbf{r}}\left[\omega^\dagger\left(\hat{c}_{\mathbf{r}}^\dagger\hat{c}_{\mathbf{r}+\mathbf{a}_1}^\dagger+\omega\hat{c}_{\mathbf{r}}^\dagger\hat{c}_{\mathbf{r}+\mathbf{a}_2}^\dagger+\omega^\dagger\hat{c}_{\mathbf{r}}^\dagger\hat{c}_{\mathbf{r}+\mathbf{a}_3}^\dagger\right)-\omega\left(\hat{c}_{\mathbf{r}}^\dagger\hat{c}_{\mathbf{r}-\mathbf{a}_1}^\dagger+\omega\hat{c}_{\mathbf{r}}^\dagger\hat{c}_{\mathbf{r}-\mathbf{a}_2}^\dagger+\omega^\dagger\hat{c}_{\mathbf{r}}^\dagger\hat{c}_{\mathbf{r}-\mathbf{a}_3}^\dagger\right)\right],\end{aligned}\tag{S116}$$

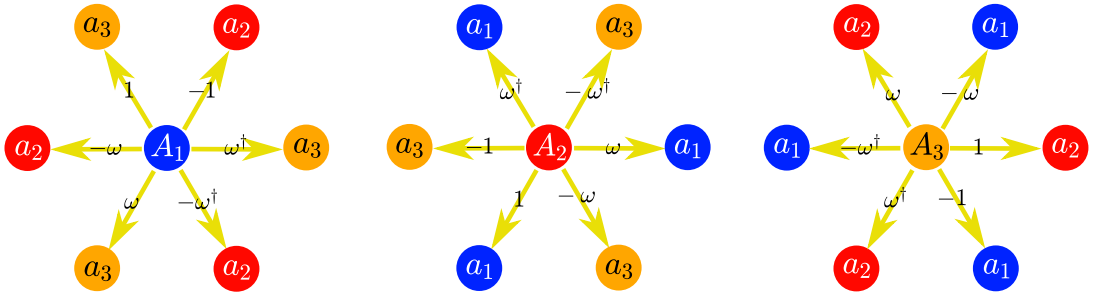

Figure S12. **Real-space representation of $k_x + ik_y$ superconducting pair function with center-of-mass momentum $2\mathbf{K}$.** Capitalized labels indicate electron sites, while lower-case labels indicate hole sites. All amplitudes should be multiplied by $\Delta_{\rm SC}/2i$. To switch the chirality of the pairing function, the hopping amplitudes are reflected across the x-axis. To switch the center-of-mass momentum, the hopping amplitudes are complex-conjugated and reflected across the x-axis.

where $\mathbf{r}$ is a lattice translation vector. Because $\mathbf{K}$ is *not* a reciprocal lattice vector in the triangular Brillouin zone, the overall phase $e^{2i\mathbf{K}\cdot\mathbf{r}}$ is not periodic in $\mathbf{r}$. This is a signature of *finite-momentum* pairing: there must be a modulation of the pairing wavefunction on a scale *incommensurate* with the lattice structure. Now, to make the phase $e^{2i\mathbf{K}\cdot\mathbf{r}}$ periodic, we can enlarge the unit cell to a $\sqrt{3}\times\sqrt{3}$ Kekule lattice where the sublattices are located at $\boldsymbol{\tau}_{A_1} = (0,0)$, $\boldsymbol{\tau}_{A_2} = -\mathbf{a}_3$, and $\boldsymbol{\tau}_{A_3} = \mathbf{a}_1$ and the new primitive translation vectors are $\bar{\mathbf{a}}_1 = \left(0,\sqrt{3}a\right)$, $\bar{\mathbf{a}}_2 = \sqrt{3}a\left(-\sqrt{3}/2,-1/2\right)$, and $\bar{\mathbf{a}}_3 = \sqrt{3}a\left(+\sqrt{3}/2,-1/2\right)$. In this reconstructed lattice, $\mathbf{K}$ is indeed a reciprocal lattice vector. The pairing function now takes the form

$$\begin{aligned}\hat{\Delta} = {}& \frac{\Delta_{\rm SC}}{2i}\sum_{\mathbf{r}}\left[\omega^\dagger\left(\hat{c}^\dagger_{A_1,\mathbf{r}}\hat{c}^\dagger_{A_3,\mathbf{r}} + \omega\hat{c}^\dagger_{A_1,\mathbf{r}}\hat{c}^\dagger_{A_3,\mathbf{r}+\bar{\mathbf{a}}_1+\bar{\mathbf{a}}_2} + \omega^\dagger\hat{c}^\dagger_{A_1,\mathbf{r}}\hat{c}^\dagger_{A_3,\mathbf{r}+\bar{\mathbf{a}}_2}\right) - \omega\left(\hat{c}^\dagger_{A_1,\mathbf{r}}\hat{c}^\dagger_{A_2,\mathbf{r}+\bar{\mathbf{a}}_2} + \omega\hat{c}^\dagger_{A_1,\mathbf{r}}\hat{c}^\dagger_{A_2,\mathbf{r}-\bar{\mathbf{a}}_1} + \omega^\dagger\hat{c}^\dagger_{A_1,\mathbf{r}}\hat{c}^\dagger_{A_2,\mathbf{r}}\right)\right] \\ & + \frac{\Delta_{\rm SC}}{2i}\sum_{\mathbf{r}}\omega^\dagger\left[\omega^\dagger\left(\hat{c}^\dagger_{A_2,\mathbf{r}}\hat{c}^\dagger_{A_1,\mathbf{r}+\bar{\mathbf{a}}_1+\bar{\mathbf{a}}_3} + \omega\hat{c}^\dagger_{A_2,\mathbf{r}}\hat{c}^\dagger_{A_1,\mathbf{r}+\bar{\mathbf{a}}_1} + \omega^\dagger\hat{c}^\dagger_{A_2,\mathbf{r}}\hat{c}^\dagger_{A_1,\mathbf{r}}\right) - \omega\left(\hat{c}^\dagger_{A_2,\mathbf{r}}\hat{c}^\dagger_{A_3,\mathbf{r}+\bar{\mathbf{a}}_1+\bar{\mathbf{a}}_2} + \omega\hat{c}^\dagger_{A_2,\mathbf{r}}\hat{c}^\dagger_{A_3,\mathbf{r}} + \omega^\dagger\hat{c}^\dagger_{A_2,\mathbf{r}}\hat{c}^\dagger_{A_3,\mathbf{r}+\bar{\mathbf{a}}_1}\right)\right] \\ & + \frac{\Delta_{\rm SC}}{2i}\sum_{\mathbf{r}}\omega\left[\omega^\dagger\left(\hat{c}^\dagger_{A_3,\mathbf{r}}\hat{c}^\dagger_{A_2,\mathbf{r}+\bar{\mathbf{a}}_3} + \omega\hat{c}^\dagger_{A_3,\mathbf{r}}\hat{c}^\dagger_{A_2,\mathbf{r}} + \omega^\dagger\hat{c}^\dagger_{A_3,\mathbf{r}}\hat{c}^\dagger_{A_2,\mathbf{r}-\bar{\mathbf{a}}_1}\right) - \omega\left(\hat{c}^\dagger_{A_3,\mathbf{r}}\hat{c}^\dagger_{A_1,\mathbf{r}} + \omega\hat{c}^\dagger_{A_3,\mathbf{r}}\hat{c}^\dagger_{A_1,\mathbf{r}+\bar{\mathbf{a}}_3} + \omega^\dagger\hat{c}^\dagger_{A_3,\mathbf{r}}\hat{c}^\dagger_{A_1,\mathbf{r}+\bar{\mathbf{a}}_1+\bar{\mathbf{a}}_3}\right)\right].\end{aligned} \tag{S117}$$

Here, the notation is that $\hat{c}^\dagger_{\sigma,\mathbf{r}} = \hat{c}^\dagger_{\mathbf{r}+\boldsymbol{\tau}_\sigma}$ and the $\mathbf{r}$ vectors are the translation vectors of the Kekule lattice. In this expanded basis, we can write the pairing function with center-of-mass momentum at $\overline{\Gamma}$. In momentum space, the Hamiltonian now takes the form

$$\hat{\Delta} = \sum_{\mathbf{k}}\begin{pmatrix}\hat{c}^\dagger_{A_1,\mathbf{k}} & \hat{c}^\dagger_{A_2,\mathbf{k}} & \hat{c}^\dagger_{A_3,\mathbf{k}}\end{pmatrix}\begin{pmatrix}0 & -\omega f(-\mathbf{k}) & \omega^\dagger f(\mathbf{k}) \\ \omega f(\mathbf{k}) & 0 & -f(-\mathbf{k}) \\ -\omega^\dagger f(-\mathbf{k}) & f(\mathbf{k}) & 0\end{pmatrix}\begin{pmatrix}\hat{c}^\dagger_{A_1,-\mathbf{k}} \\ \hat{c}^\dagger_{A_2,-\mathbf{k}} \\ \hat{c}^\dagger_{A_3,-\mathbf{k}}\end{pmatrix} = \sum_{\mathbf{k},\sigma,\sigma'}\hat{c}^\dagger_{\sigma,\mathbf{k}}\Delta_{\sigma\sigma'}(\mathbf{k})\hat{c}^\dagger_{\sigma',-\mathbf{k}}, \tag{S118}$$

where $f(\mathbf{k}) = (\Delta_{\rm SC}/2i)\left[\exp(i\mathbf{k}\cdot\mathbf{a}_1) + \omega\exp(i\mathbf{k}\cdot\mathbf{a}_2) + \omega^\dagger\exp(i\mathbf{k}\cdot\mathbf{a}_3)\right]$. As a check of consistency, we note that antisymmetry is satisfied explicitly because $\Delta_{\sigma,\sigma'}(\mathbf{k}) = -\Delta_{\sigma',\sigma}(-\mathbf{k})$ and that the projection to the K valley holds

$$\frac{1}{3}\begin{pmatrix}1 & \omega^\dagger & \omega\end{pmatrix}\begin{pmatrix}0 & -\omega f(-\mathbf{k}) & \omega^\dagger f(\mathbf{k}) \\ \omega f(\mathbf{k}) & 0 & -f(-\mathbf{k}) \\ -\omega^\dagger f(-\mathbf{k}) & f(\mathbf{k}) & 0\end{pmatrix}\begin{pmatrix}1 \\ \omega^\dagger \\ \omega\end{pmatrix} = \Delta_{\rm SC}\left[\sin(\mathbf{k}\cdot\mathbf{a}_1) + \omega\sin(\mathbf{k}\cdot\mathbf{a}_2) + \omega^\dagger\sin(\mathbf{k}\cdot\mathbf{a}_3)\right]. \tag{S119}$$

To switch the chirality of the pairing function, we replace ω *inside* the $f(\mathbf{k})$ functions with $\omega^\dagger$. To switch the center-of-mass momentum, we replace ω *outside* the $f(\mathbf{k})$ functions with $\omega^\dagger$. Therefore, if we want to describe a $k_x - ik_y$ pairing function at K', we simply complex conjugate all factors of ω in $\Delta_{\sigma,\sigma'}(\mathbf{k})$. However, prior theoretical studies have suggested that the chirality of superconductivity is locked to the valley polarization.

The foregoing preliminary considerations allow us to construct a tight-binding model where the electron and hole sectors are independently represented by fermionic operators, $\hat{d}_{\sigma,\mathbf{k}} = \hat{c}^\dagger_{\sigma,-\mathbf{k}}$. The gap function is represented in real space as hoppings between the electron and hole sectors, as shown in Fig. S12.

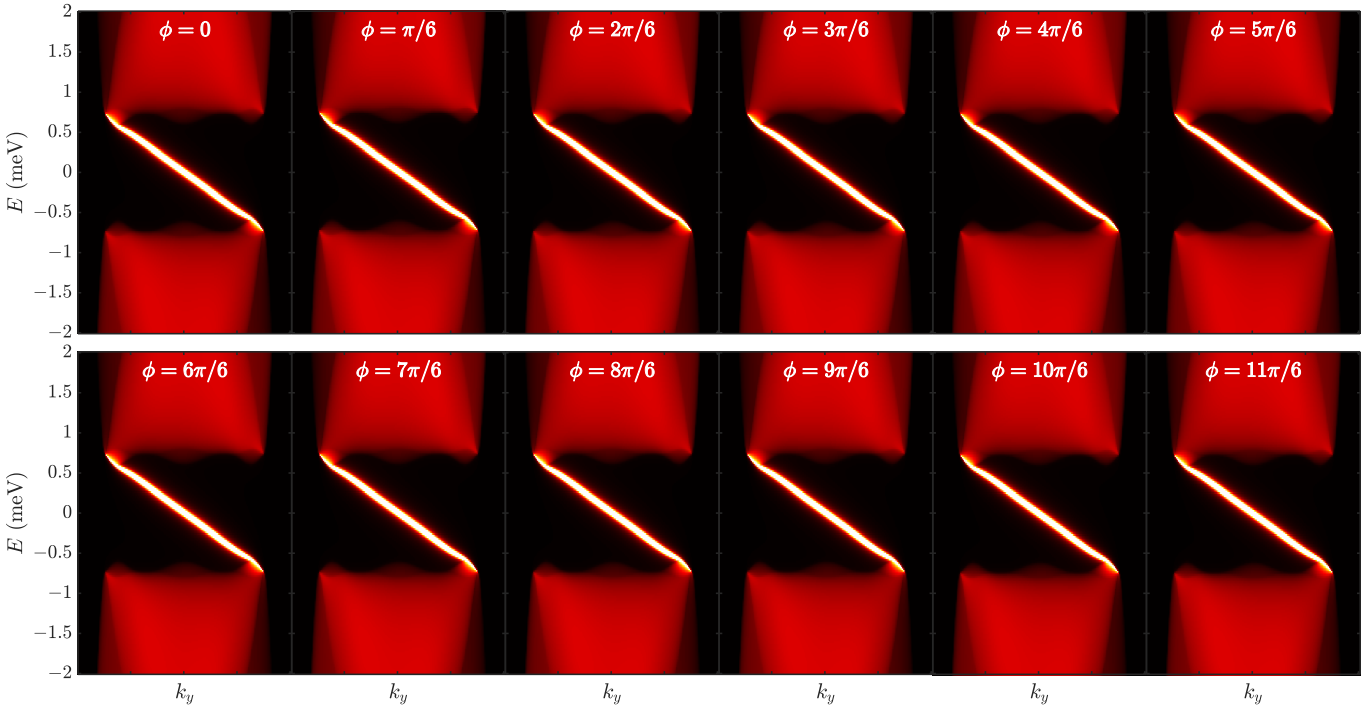

Figure S13. **BdG band structure of an SNS Josephson junction as a function of the pairing phase** ϕ. In this calculation, the domain wall has no intervalley hybridization. Here, $N = 4$, $m_z = 30$ meV, $n = 5 \times 10^{11}$ cm^{-2}, $w = 2$ nm, $\Delta = 30$ meV, and $\Delta_{\mathrm{SC}} = 10$ meV.

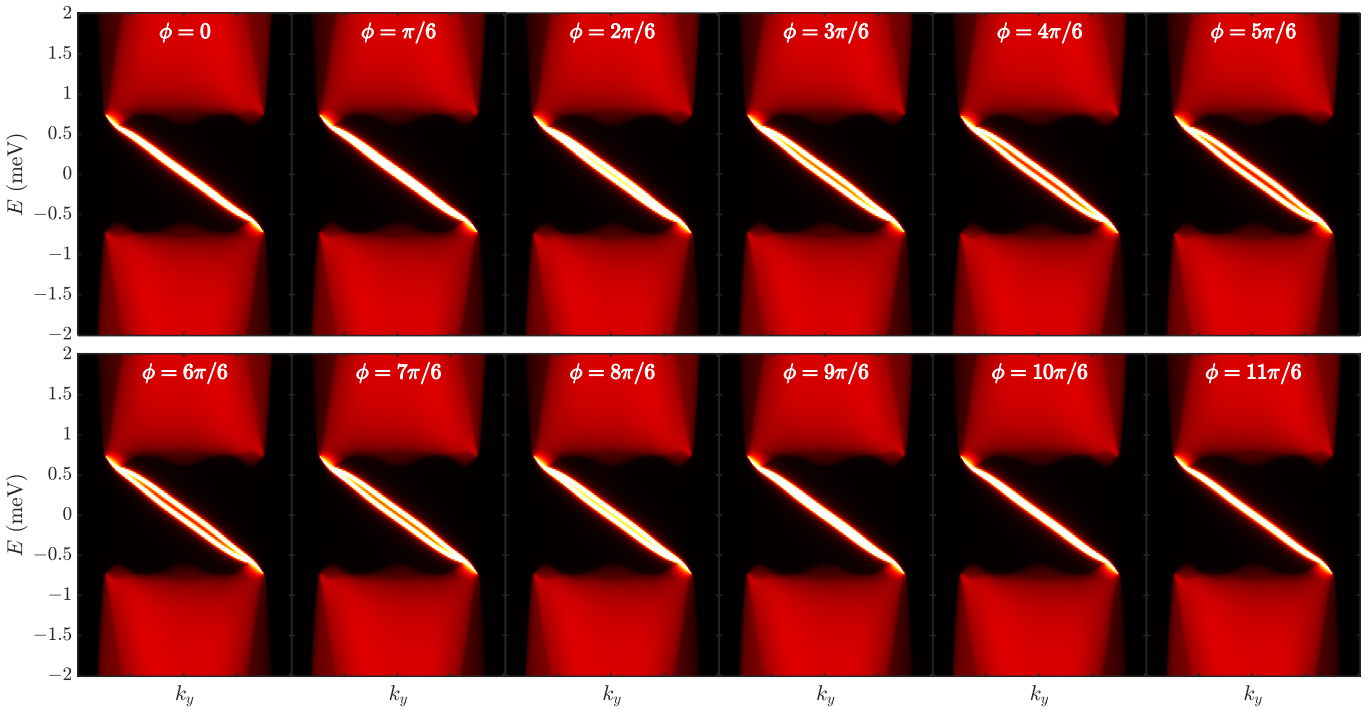

Figure S14. **BdG band structure of an SNS Josephson junction as a function of the pairing phase** ϕ. In this calculation, the domain wall has an intervalley interaction τ_1 with magnitude $m = 1$ meV. Here, $N = 4$, $m_z = 30$ meV, $n = 5 \times 10^{11}$ cm^{-2}, $w = 2$ nm, $\Delta = 30$ meV, and $\Delta_{\mathrm{SC}} = 10$ meV.

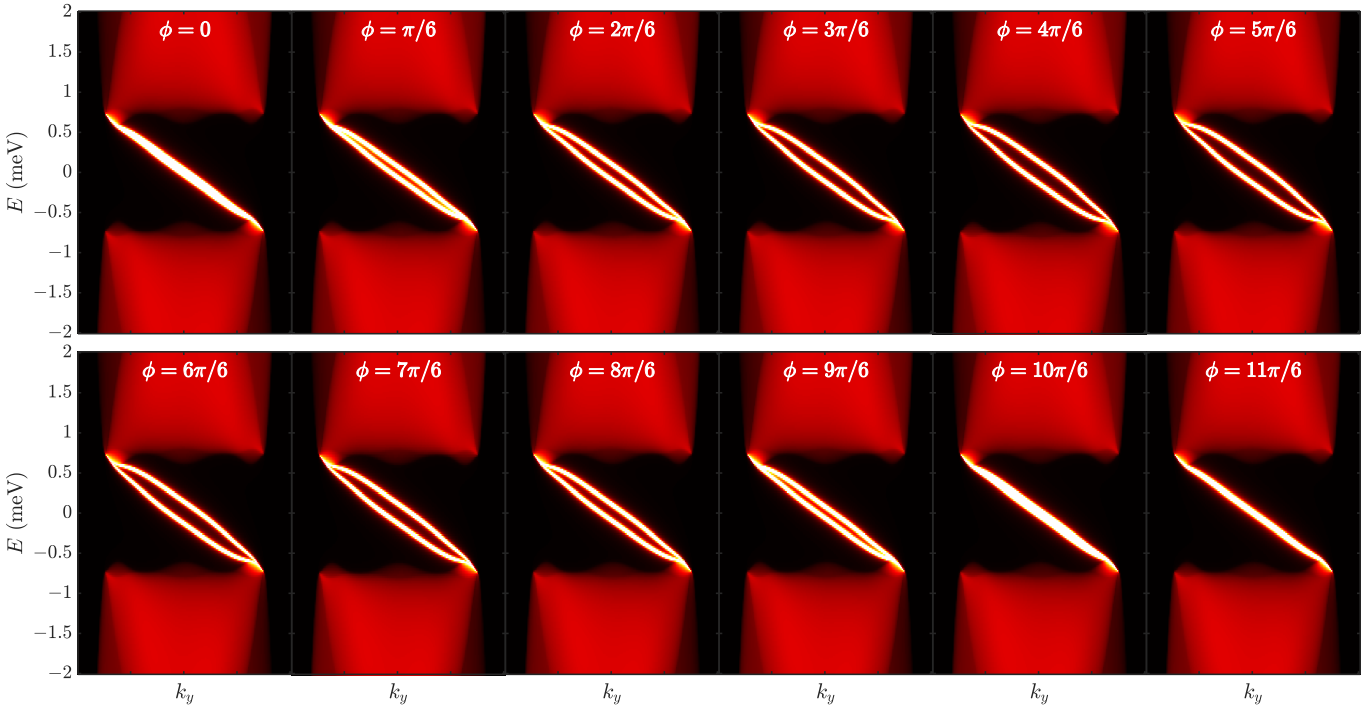

Figure S15. **BdG band structure of an SNS Josephson junction as a function of the pairing phase** ϕ. In this calculation, the domain wall has an intervalley interaction τ_1 with magnitude $m = 2$ meV. Here, $N = 4$, $m_z = 30$ meV, $n = 5 \times 10^{11}$ cm^{-2}, $w = 2$ nm, $\Delta = 30$ meV, and $\Delta_{\mathrm{SC}} = 10$ meV.

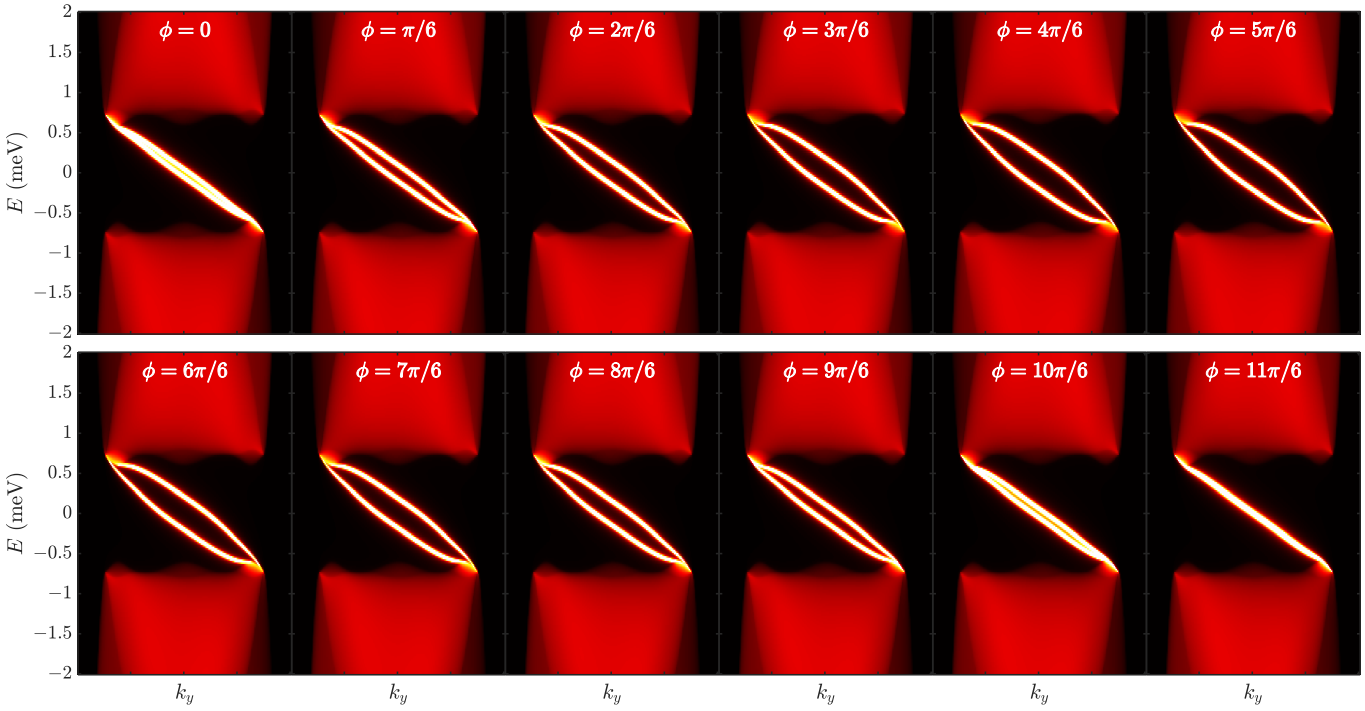

Figure S16. **BdG band structure of an SNS Josephson junction as a function of the pairing phase** ϕ. In this calculation, the domain wall has an intervalley interaction τ_1 with magnitude $m = 3$ meV. Here, $N = 4$, $m_z = 30$ meV, $n = 5 \times 10^{11}$ cm^{-2}, $w = 2$ nm, $\Delta = 30$ meV, and $\Delta_{\mathrm{SC}} = 10$ meV.

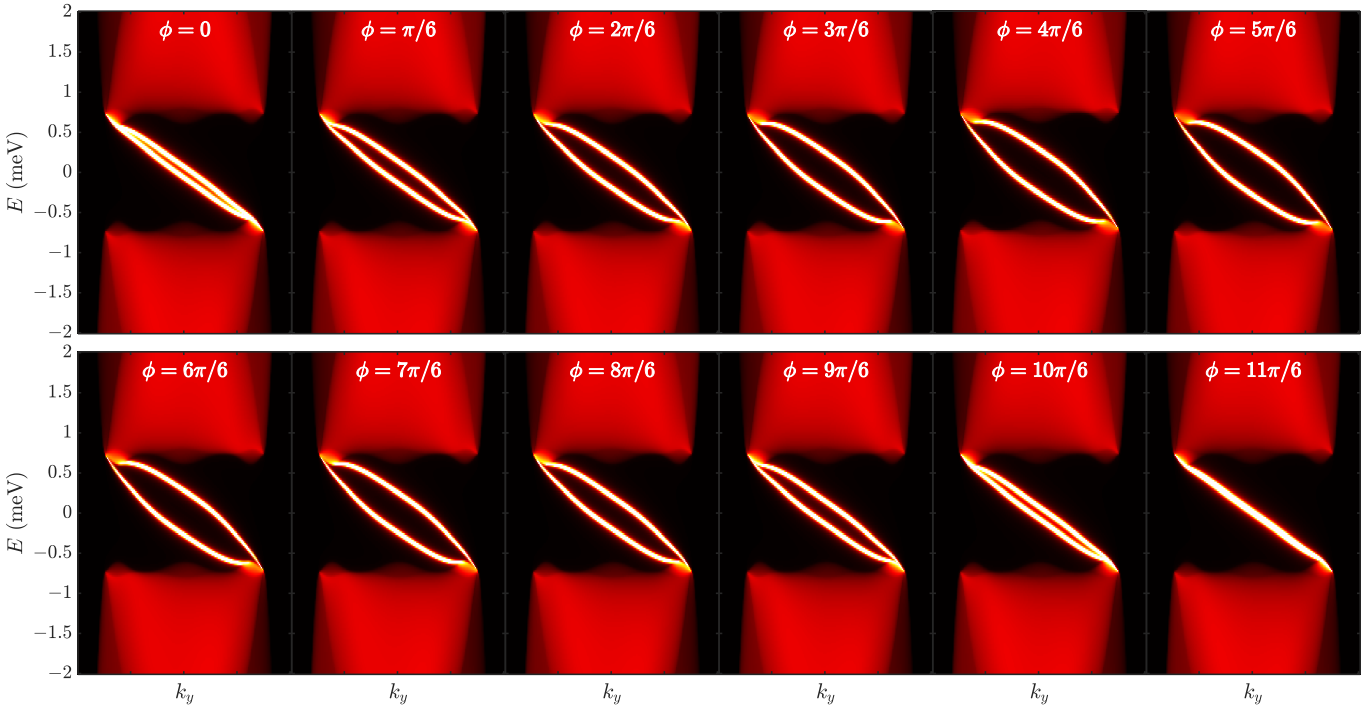

Figure S17. **BdG band structure of an SNS Josephson junction as a function of the pairing phase** ϕ. In this calculation, the domain wall has an intervalley interaction τ_1 with magnitude $m = 4$ meV. Here, $N = 4$, $m_z = 30$ meV, $n = 5 \times 10^{11}$ cm^{-2}, $w = 2$ nm, $\Delta = 30$ meV, and $\Delta_{\mathrm{SC}} = 10$ meV.

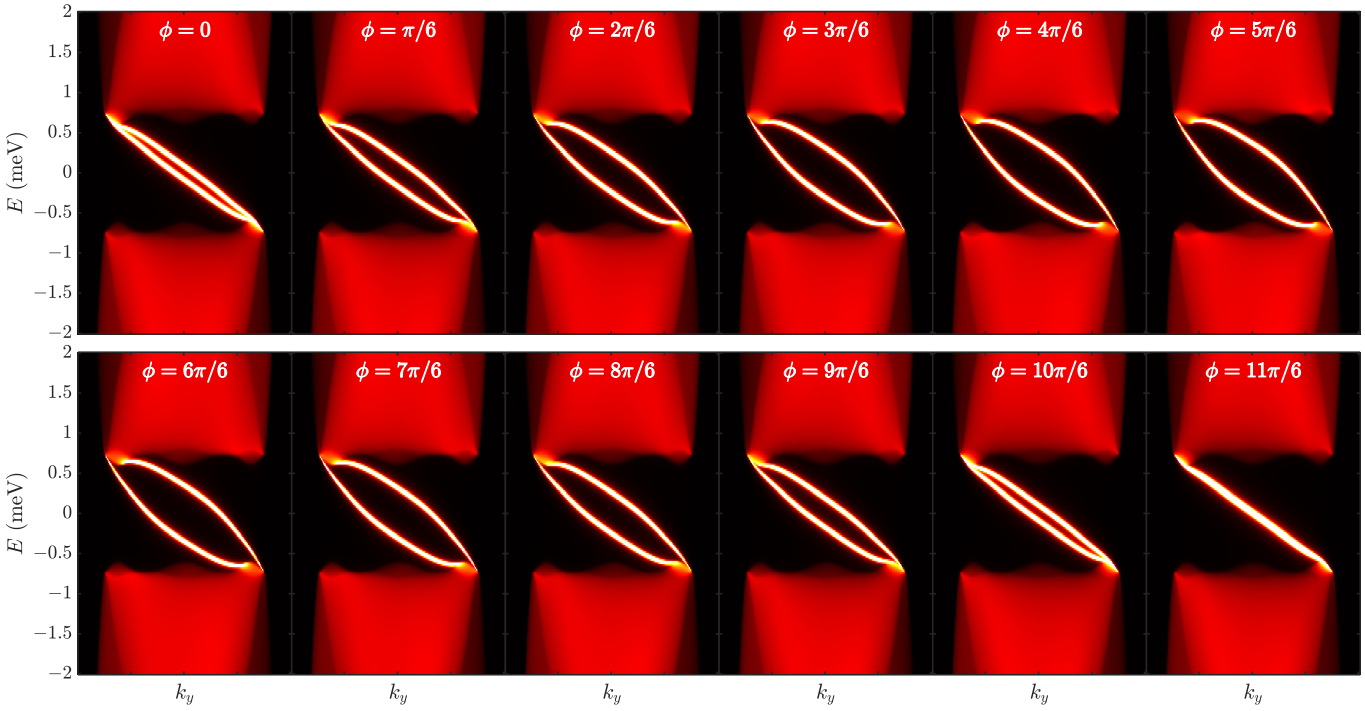

Figure S18. **BdG band structure of an SNS Josephson junction as a function of the pairing phase** ϕ. In this calculation, the domain wall has an intervalley interaction τ_1 with magnitude $m = 5$ meV. Here, $N = 4$, $m_z = 30$ meV, $n = 5 \times 10^{11}$ cm^{-2}, $w = 2$ nm, $\Delta = 30$ meV, and $\Delta_{\mathrm{SC}} = 10$ meV.

B. Supercurrent calculation

The supercurrent is defined as the phase derivative of the free energy $\mathcal{F}(\phi)$

$$I(\phi) = -\frac{2e}{\hbar}\frac{\partial \mathcal{F}}{\partial \phi}. \tag{S120}$$

The free energy at finite temperature for a single spin species (due to polarization) is given by

$$\mathcal{F}(\phi) = -\frac{k_B T}{2}\sum_{n=-\infty}^{\infty} \ln\det\left[-\mathcal{G}^{-1}(i\omega_n)\right] + ..., \tag{S121}$$

where $\mathcal{G}(i\omega_n) = (i\omega_n - \mathcal{H}_{\rm BdG})^{-1}$ is the BdG Green's function and $\omega_n = (2n+1)\pi k_B T$. The factor of $1/2$ is there to avoid double counting the fermion degrees of freedom in the BdG basis [10]. Using the rule $\partial_\phi \ln\det\left[-\mathcal{G}^{-1}\right] = \mathrm{tr}\,\mathcal{G}\partial_\phi\mathcal{G}^{-1}$, the supercurrent is given by

$$I(\phi) = \frac{e}{\hbar}k_B T\sum_{n=-\infty}^{\infty}\mathrm{Tr}\left[\mathcal{G}(i\omega_n)\frac{\partial}{\partial\phi}\mathcal{G}^{-1}(i\omega_n)\right] = -\frac{e}{\hbar}\oint_{\mathcal{C}}\frac{dz}{2\pi i}f(z)\,\mathrm{Tr}\left[\mathcal{G}(z)\frac{\partial}{\partial\phi}\mathcal{G}^{-1}(z)\right], \tag{S122}$$

where $f(z)$ is the fermion occupation function and $\mathcal{C}$ is a contour that encloses the poles of $f(z)$. For now, we leave the sum over momentum implicit for brevity. Now, assuming that $\mathcal{G}(\omega + i\eta)$ is analytic in the upper half plane and $\mathcal{G}(\omega - i\eta)$ is analytic in the lower half plane and both decay as $|z| \to \infty$, the contour integral can be turned into an integral along the real line

$$I(\phi) = -\frac{e}{\hbar}\int_{-\infty}^{\infty}\frac{d\omega}{2\pi i}n_F(\omega)\,\mathrm{Tr}\left[\mathcal{G}(\omega+i\eta)\frac{\partial}{\partial\phi}\mathcal{G}^{-1}(\omega+i\eta) - \mathcal{G}(\omega-i\eta)\frac{\partial}{\partial\phi}\mathcal{G}^{-1}(\omega-i\eta)\right]. \tag{S123}$$

Now, noting that $\mathcal{G}(\omega+i\eta) = \mathcal{G}^\dagger(\omega - i\eta)$, we can simplify the integrand

$$I(\phi) = -\frac{e}{\hbar}\int_{-\infty}^{\infty}\frac{d\omega}{\pi}n_F(\omega)\mathrm{Im}\,\mathrm{Tr}\left[\mathcal{G}(\omega+i\eta)\frac{\partial}{\partial\phi}\mathcal{G}^{-1}(\omega+i\eta)\right]. \tag{S124}$$

To simplify, we assume that only the self-energy on the right domain contains the phase ϕ,

$$I(\phi) = \frac{e}{\hbar}\int_{-\infty}^{\infty}\frac{d\omega}{\pi}n_F(\omega)\mathrm{Im}\,\mathrm{Tr}\left[\mathcal{G}(\omega+i\eta)\frac{\partial}{\partial\phi}\Sigma_R(\omega+i\eta)\right]. \tag{S125}$$

Using the identity $\partial_\phi\Sigma_R = i[\gamma_z, \Sigma_R]/2$, where γ_z is a Pauli matrix that acts on Nambu space, we find

$$I(\phi) = \frac{e}{\hbar}\mathrm{Re}\left[\int_{-\infty}^{\infty}\frac{d\omega}{2\pi}n_F(\omega)\,\mathrm{Tr}\left(\mathcal{G}(\omega+i\eta)[\gamma_z, \Sigma_R(\omega+i\eta)]\right)\right]. \tag{S126}$$

At zero temperature, the integral only goes up to $\omega = 0$. In this case, we use a change of variables to map the interval $(-\infty, 0)$ to the interval $(-1, 1)$ and then use contour integration to evaluate the integral numerically. We apply the adaptive Gauss-Kronrod quadrature for fast convergence. The error on the supercurrent calculated at each k_y is approximately 10^{-5} nA.

[1] ω here is not the same as frequency ω used later. It should be clear from context which ω is used as they do not overlap in usage.

[2] R. Takahashi and S. Murakami, Gapless interface states between topological insulators with opposite dirac velocities, Phys. Rev. Lett. **107**, 166805 (2011).

[3] F. Guinea, C. Tejedor, F. Flores, and E. Louis, Effective two-dimensional hamiltonian at surfaces, Phys. Rev. B **28**, 4397 (1983).

[4] M. P. L. Sancho, J. M. L. Sancho, and J. Rubio, Highly convergent schemes for the calculation of bulk and surface green functions, J. Phys. F **15**, 851 (1985).

[5] D.-N. Liu, J. Zheng, and P. A. Pantaleón, Mode-selective cloaking and phase-matching cavity resonances in bilayer graphene transport, Phys. Rev. B **113**, 165412 (2026).

[6] S. Datta, *Electronic Transport in Mesoscopic Systems*, Cambridge Studies in Semiconductor Physics and Microelectronic Engineering (Cambridge University Press, 1995).

[7] D. A. Ryndyk, *Theory of Quantum Transport at Nanoscale: An Introduction*, Springer Series in Solid-State Sciences, Vol. 184 (Springer International Publishing, Cham, Switzerland, 2016).

[8] C. Caroli, R. Combescot, P. Nozières, and D. Saint-James, A direct calculation of the tunnelling current, J. Phys. C **4**, 916 (1971).

[9] D. S. Fisher and P. A. Lee, Relation between conductivity and transmission matrix, Phys. Rev. B **23**, 6851 (1981).

[10] In the limit $\Delta_{\mathrm{SC}} \to 0$, this definition gives exactly the free energy of the Fermi sea of a normal metal.